Multiphase Fluid Flow through Porous Media

Conductivity and Geomechanics

by

Nariman Mahabadi

A Dissertation Presented in Partial Fulfillment
of the Requirements for the Degree
Doctor of Philosophy

Approved July 2016 by the
Graduate Supervisory Committee:

Jaewon Jang, Chair
Claudia Zapata
Edward Kavazanjian

ARIZONA STATE UNIVERSITY

August 2016

ABSTRACT

The understanding of multiphase fluid flow in porous media is of great importance in many fields such as enhanced oil recovery, hydrology, CO_2 sequestration, contaminants cleanup, and natural gas production from hydrate bearing sediments.

In this study, first, the water retention curve (WRC) and relative permeability in hydrate bearing sediments are explored to obtain fitting parameters for semi-empirical equations. Second, immiscible fluid invasion into porous media is investigated to identify fluid displacement pattern and displacement efficiency that are affected by pore size distribution and connectivity. Finally, fluid flow through granular media is studied to obtain fluid-particle interaction. This study utilizes the combined techniques of discrete element method simulation, micro-focus X-ray computed tomography (CT), pore-network model simulation algorithms for gas invasion, gas expansion, and relative permeability calculation, transparent micromodels, and water retention curve measurement equipment modified for hydrate-bearing sediments. In addition, a photoelastic disk set-up is fabricated and the image processing technique to correlate the force chain to the applied contact forces is developed.

The results show that the gas entry pressure and the capillary pressure increase with increasing hydrate saturation. Fitting parameters are suggested for different hydrate saturation conditions and morphologies. And, a new model for immiscible fluid invasion and displacement is suggested in which the boundaries of displacement patterns depend on the pore size distribution and connectivity. Finally, the fluid-particle interaction study shows that the fluid flow increases the contact forces between photoelastic disks in parallel direction with the fluid flow.

DEDICATION

This dissertation is dedicated to my love, Golnoosh, who has always supported me and encouraged me to pursue my dreams. Thank you very much for your unconditional love and sincere support. This work is also dedicated to my parents. All I have and will accomplish are only possible due to their love and sacrifice.

ACKNOWLEDGMENTS

I would like to express my sincere gratitude to my advisor, Dr. Jaewon Jang for giving me such an excellent time in my life. It was really fortunate to work with him at ASU. I was always amazed by his endless curiosity, patience, excellent guidance, and generous support, which really motivated and helped me to pursue my Ph.D.

I would like to thank my thesis committee members, Dr. Edward Kavazanjian and Dr. Claudia Zapata for their insightful comments and recommendations.

Special thanks to Dr. Yongkoo Seol (DOE/NETL), Dr. Sheng Dai (Georgia Tech), Dr. William. F. Waite (USGS) and Xianglei Zheng for their generous support and great experience.

Finally, I would like to acknowledge the support for this work that was funded by the U.S. Department of Energy gas hydrate project. I'm grateful to the funding source that made my Ph.D. work possible.

TABLE OF CONTENTS

Page

CHAPTER Page

CHAPTER Page

LIST OF TABLES

LIST OF FIGURES

Figure Page

Figure Page

CHAPTER 1

INTRODUCTION

1.1 Motivation

The understanding of multiphase fluid flow in porous media is of great importance in many fields such as enhanced oil recovery, hydrology, CO_2 sequestration, contaminants cleanup and natural gas production from hydrate bearing sediments. However, there are many unanswered questions about the key parameters that characterize gas and water flows in porous media. The characteristics of multiphase fluid flow in porous media such as water retention curve, relative permeability, preferential fluid flow patterns and fluid-particle interaction should be taken into consideration for a fundamental understanding of the behavior of pore scale systems.

The main focus of this study is to characterize the pore scale properties of methane hydrates in hydrate bearing sediments. Methane hydrates are solid crystalline compounds in which methane molecules are trapped in the cage of water molecules. High water pressures and low temperature provide the stable condition for methane hydrate. Methane hydrates are found in large quantities beneath the permafrost regions and shallow marine sediments. The amount of methane contained in gas hydrates is estimated to be $\sim 3\times10^{15}$ m^3 [Boswell and Collett, 2011; NETL/DOE, 2011].

The study of methane hydrate has critical implications on various geological and engineering processes such as hydrate dissociation, gas production, global warming and climate change. The characterization of the methane hydrate behavior such as flow properties in hydrate bearing sediments is therefore urgently needed.

1.2 Thesis Organization

This study investigates multiphase fluid flow properties in porous medium, particularly the characterization of gas hydrates in hydrate bearing sediments.

Chapter 2 reports numerical simulation of relative water and gas permeability in hydrate bearing sediments using pore network modeling obtained by discrete element simulation. Gas expansion is simulated through the pore network model and the effects of various hydrate saturations are studied.

Chapter 3 focuses on numerical modelling of water retention curve and relative permeability functions based on micro CT images of recovered sample of hydrate bearing sediments. The fitting parameters are suggested for different hydrate saturations and hydrate topologies.

Chapter 4 documents an experimental study on hydrate bearing sediments. Tetrahydrofuran (THF) is selected as hydrate former. The pore habit of THF hydrates is investigated by visual observation in a transparent micromodel and the measurements of water retention curves in THF hydrate-bearing sediments is conducted for different hydrate saturations.

Chapter 5 reports a study to explore the effect of pore size distribution on the preferential multiphase fluid flow patterns in the porous media. A new form of phase diagram is suggested based on the results of this study.

Chapter 6 focuses on an experimental study using photo-elastic disks to visualize the evolution of force chains for fluid-particle interaction. A unique method is developed to correlate the external force to the pattern of fringes in the photoelastic disks.

Salient conclusions are summarized in Chapter 7.

CHAPTER 2

RELATIVE WATER AND GAS PERMEABILITY FOR GAS PRODUCTION FROM HYDRATE-BEARING SEDIMENTS: DEM AND PORE NETWORK MODEL SIMULATION

2.1 Introduction

Numerical simulation studies predict the long-term behavior of hydrate-bearing sediments during gas production [Kurihara et al., 2008; Moridis et al., 2009; Moridis and Regan, 2007a, 2007b; Anderson et al., 2011, Myshakin et al., 2011, 2012]. Numerical simulators for gas hydrate studies adopt many equations for coupled-process analyses. A relative permeability equation among many others embedded in numerical simulators is one of important equations because it affects gas and water production rate and gas recovery efficiency, therefore it decides the economic development of hydrate-bearing sediments [Johnson et al., 2011; Minagawa et al., 2004; Mingawaga et al., 2007; Kleinberg et al., 2003; Gupta, 2007; Jang and Santamarina, 2011, 2014; Santamarina and Jang, 2009, 2010]. Expression for relative water k_{rw} and gas permeability k_{rg} as a function of water saturation S_w requires fitting parameters [Corey, 1954; Brooks and Corey, 1964; Stone, 1970; Anderson et al., 2011; Moridis et al., 2008].

In this study, a pore network model is developed to simulate hydrate dissociation and gas expansion in a distributed hydrate system where initial hydrate saturation varies from S_h=10% to 60%. Based on the numerical simulation results of relative water and gas permeability, fitting parameters for modified Stone equation are suggested.

2.2 Relative Permeability Equations for Gas Hydrate Production

The relative permeability [unitless] of water k_{rw} (or gas k_{rg}) is the water (or gas) permeability [m/s] at a given water saturation S_w normalized by a reference permeability which is the water (or gas) permeability at 100% water (or gas) saturation. The permeability at the residual phase saturation may be used as a reference permeability [Jaiswal, 2004]. In this study, water permeability at 100% water saturation and gas permeability at residual water saturation S_{rw} (at which there is no more water displacement) are used as reference permeabilities.

Modified Stone equation shown below is frequently used for gas hydrate simulation study.

$$k_{rw}=\left(\frac{S_w-S_{rw}}{1-S_{rw}}\right)^{n_w} \tag{2.1}$$

$$k_{rg}=\left(\frac{S_g-S_{rg}}{1-S_{rw}}\right)^{n_g} \tag{2.2}$$

Where S_{rw} is the residual water saturation, S_{rg} is the residual gas saturation [Stone, 1970; Moridis et al., 2008]. The fitting parameters n_w and n_g, the residual water saturation S_{rw} and residual gas saturation S_{rg} need to be determined. As the fitting parameters n_w and n_g increase, both relative water and gas permeabilities decrease at a given water saturation.

Fitting parameters for the modified Stone equation and residual water and gas saturations used in hydrate-bearing reservoir simulations are compiled: n_w=3.0~4.5, n_g=3.0~4.0, S_{rw}=0.1~0.25, and S_{rg}=0~0.02 [Reagan and Moridis, 2008; Moridis and Kowalsky, 2005; Moridis et al., 2007, 2009; Moridis and Regan, 2007a, 2007b; Moridis and Sloan, 2007; Rutqvist and Moridis, 2007, 2009; Anderson et al., 2011; Kurihara et al.,

2011]. However, to the authors' best knowledge, any supporting experimental or numerical evidence to validate these selected fitting parameters for hydrate simulation studies is not available in the literature.

2.3 Numerical Method and Procedure

A pore network model consists of pores connected by tubes. Hydrates are assigned to pores of the pore-network model. Then, relative gas and water permeability is calculated during gas expansion after hydrate dissociation. The method of pore network model generation, gas expansion, and permeability calculation is explained in this section.

2.3.1 Pore Network Model Generation

Using the grain size distribution and the effective stress of in-situ hydrate-bearing sediments, a three-dimensional particle packing is generated by Discrete Element Modeling DEM (*Itasca, PFC 3D*). The grain size distribution of sandy sediments from Mallik-Mackenzie Delta is selected for input to the DEM simulation [Soga et al., 2007; Jenner et al., 1999]. The information of grain size distribution of other in-situ hydrate-bearing sediments can be found in Soga et al. (2007), Jenner et al. (1999), Ginsberg et al. (2000), and Tan (2004). After particles are generated, a confining pressure σ'=9MPa equivalent to the effective stress of in-situ hydrate-bearing sediments at the depth of 900m in permafrost is applied to consolidate the particle packing (Figure 2.1a). Once the particle packing is consolidated, the pore space of the packing is extracted (Figure 2.1b). Then, the maximal ball algorithm developed by Silin and Patzek (2006), Al-Kharusi and Blunt (2007), Dong (2007), and Dong and Blunt (2009) is used to extract a three-dimensional pore network model (Figure 2.1c). The maximal ball algorithm generates several spheres

inscribed in the pore space (called maximal ball). Generally, big spheres inscribed in the pore space become pores of the pore-network model, and the radii of small spheres inscribed in the pore space are used as the radii of tubes connecting two pores. The length of tubes is proportional to the distance between the centers of two neighboring pores. Therefore, the extracted pore-network model consists of pores and tubes. Detailed algorithm for classifying generated inscribed spheres as pores or tubes is explained in Dong and Blunt (2009).

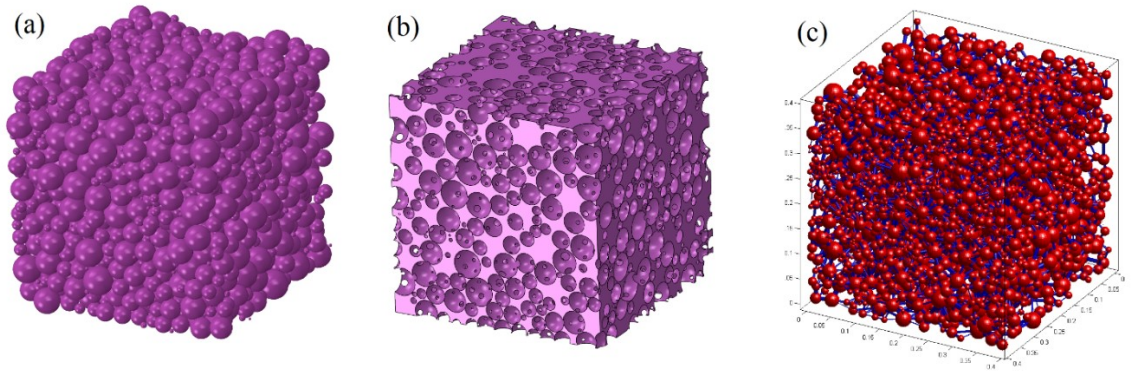

Figure 2.1 Pore-network model generation. (a) Particle packing (4mm×4mm×4mm cube) generated by discrete element model. The maximum particle diameter is Dmax=0.52mm, the minimum particle diameter is Dmin=0.04mm, the coefficient of uniformity is $cu=D_{60}/D_{10}$=0.3mm/0.09mm=3.3, and the coefficient of curvature is $cc=D_{60}^2/(D_{10}D_{30})$=(0.3mm)2/(0.09mmx0.21mm)=4.8 (Here, DX is the particle diameter representing that X% of total particles is smaller than DX). (b) Pore space of the particle packing. (c) Extracted pore network. The extracted pore network model consists of 4,526 pores and 15,282 tubes with the tube connectivity per pore (coordination number) of cn=6.5. Mean pore radius is μ[Rpore]=82μm and standard deviation in pore radius in logarithmic scale is σ[ln(Rpore)]=0.36, which is within the range of standard deviation in pore size of natural sediments obtained by mercury intrusion porosimetry, σ[ln(Rpore)]=0.4±0.2 [Phadnis and Santamarina, 2011]. Mean tube radius is μ[Rtube]=19μm.

2.3.2 Initial Hydrate Distribution

Hydrates are assigned in pores to satisfy a target initial hydrate saturation. To emulate Oswald ripening effect, pores are fully filled with either hydrate or water [Dai et al., 2012; Dai and Santamarina, 2013]. It is assumed that hydrates fill the largest pore first [Clennell et al., 1999; Dai et al., 2012]. Large pores of the pore-network model are not spatially correlated, which means hydrate pores are distributed instead of forming patchy. Therefore, fitting parameters that are suggested from gas expansion simulation are valid for distributed hydrate system where hydrates preferentially occupy large pores.

2.3.3 Hydrate Dissociation by Depressurization

Hydrates dissociate into methane gas and water. To simulate the hydrate dissociation and gas expansion, the water pressure at pore-network boundaries decreases from 13MPa to 0.1MPa at a given temperature 280K. The applied boundary pressure P=0.1MPa at 280K results in ~170 times of fluid volume expansion [Jang and Santamarina, 2011]. The depressurization rate is assumed to be very slow so that the heat needed for hydrate dissociation is transported from the pore-network model boundaries to maintain constant temperature.

2.3.4 Gas Expansion

While the volume of water dissociated from hydrate is ~79% of the initial volume of hydrate, the volume of dissociated methane gas is dependent on pressure and temperature conditions. The solubility of methane in water is assumed zero due to low solubility of methane (e.g., 0.12 mole of methane is dissolved in 1kg of water at P=6.6MPa and T=274K [Jung et al., 2010]). The modified Peng-Robinson equation of state (PRSV)

is used to compute the volume of methane gas during depressurization [Stryjek and Vera, 1986]:

$$P_g = \frac{RT_g}{V_g - b} - \frac{a}{V_g(V_g + b) + b(V_g - b)} \tag{2.3}$$

Where P_g is the gas pressure, T_g is the gas temperature, V_g is the gas volume per 1 mole of gas, R is the universal gas constant, and the values of a and b are parameters for methane gas which are tabulated in Jang and Santamarina (2011).

Differential pressure between gas and water in a tube of the pore network model is given by the capillary pressure, which is a function of surface tension T_s, contact angle θ, and tube radius R_{tube}, $P_c = P_g - P_w = 2T_s\cos\theta / R_{tube}$. The water-methane interfacial tension is $T_s = 0.072$mN/m and the contact angle is assumed $\theta = 0°$ for a perfectly wetting system. Hydrate dissociation and gas expansion starts by gradually decreasing the water pressure at two opposite boundaries of the pore network model. When the pressure drops below that required for hydrate stability, the hydrate breaks down and releases methane gas. Gas expands to the neighboring water pores once the gas pressure P_g exceeds the summation of water pressure P_w and the capillary pressure P_c, $P_g > P_w + P_c$. Gas stops expanding to neighboring water clusters if (1) water pores are isolated by surrounding gas pores (The isolated water cluster doesn't have an access to a water drainage path to boundaries) or (2) the gas cluster does not satisfy the gas expansion condition, $P_g > P_w + P_c$. An extended Hoshen-Kopelman algorithm is used to cluster both water and gas pores at every expansion step and check a water drainage path [Hoshen and Kopelman, 1976; Al-Futaisi and Patzek, 2003].

During gas expansion, the radius of tubes is used to calculate the capillary pressure, and the pore volume is used to calculate the gas pressure during gas expansion.

2.3.5 Permeability Calculation

If both pores connected by one tube are occupied by water (or gas), the tube is considered to have water (or gas) permeability. If one pore is occupied by water and the other pore is occupied by gas, neither gas nor water permeability is considered for the tube connecting two pores. For permeability calculation, the distance between centers of two neighboring pores is used for the tube length. The flow rate q [m^3/s] through a tube is a function of fluid viscosity η [$N \cdot s/m^2$], tube radius R_{tube} [m], tube length ΔL [m] and pressure difference ΔP [N/m^2] between end nodes:

$$q=\frac{\pi R_{tube}^4}{8\eta\Delta L}\Delta P=\alpha\Delta P \tag{2.4}$$

Where $\alpha=\pi R_{tube}^4/(8\eta\Delta L)$, called tube conductivity. By the mass conservation law, the total flow rate into a node equals the total flow rate out of the node, $\Sigma q_i=0$. The mass balance equation applies to all internal nodes, resulting in a system of linear equations which is captured in matrix form, $\underline{\underline{A}}\,\underline{P} = \underline{B}$ where the matrix $\underline{\underline{A}}$ consists of tubes' conductivities α, $\underline{P}$ is the vector of unknown pressures at internal nodes, and the vector $\underline{B}$ captures known boundary pressures. Once the pressures $\underline{P}$ is calculated as $\underline{P}=\underline{\underline{A}}^{-1}\underline{B}$, the global flow rate Q [m^3/s] through the pore networks is obtained by adding the flow rate q in all tubes that are connected to one boundary (see Jang et al. 2011 for detailed procedure of permeability calculation). In this manuscript, the term "permeability" means the global flow rate Q of the pore network model. This procedure is repeated at every expansion step.

2.4 Numerical Results

Several initial hydrate saturations are used: S_h=0.1, 0.2, 0.4, and 0.6. One simulation is performed for each initial hydrate saturation condition. For each simulation run, the configuration of the pore network model such as pore size, pore location, and connectivity is maintained constant.

Initial hydrate distribution and gas expansion for S_h=0.1 case is shown in Figure 2.2. Depressurization below the hydrate stability boundary allows hydrates to dissociate into gas and water (Figure 2.2a). Gas percolation occurs at the gas saturation S_g=0.21 (Figure 2.2b). Gas expands with more depressurization (Figure 2.2c). Gas continues to expand until the water clusters lose a water drainage path. In the pore-network model simulation using several initial hydrate saturations, gas expansion stops before the boundary pressure reaches down to P=0.1MPa due to the loss of water drainage path. For example, in case of the simulation using the initial hydrate saturation S_h=60%, gas expansion stopped when the boundary pressure applied to the pore-network model is P=9.4MPa. The applied boundary pressures are P=6.6MPa for S_h=40%, P=3.5MPa for S_h=20%, and P=1.72MPa for S_h=10% when gas expansion stopped. Even though the boundary pressure is programmed in the algorithm to decrease from 13MPa to 0.1MPa, gas expansion stops due to the loss of a water drainage path. At every gas expansion step, water and gas permeability is calculated and later divided by the reference permeability of each phase.

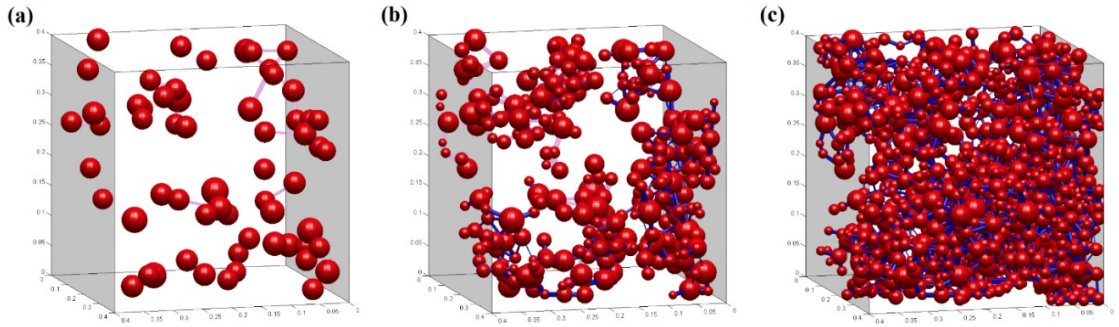

Figure 2.2 Gas expansion by depressurization: (a) Gas expansion right after hydrate dissociation (Initial hydrate saturation S_h=0.10). (b) Gas starts percolating from left gray boundary to right gray boundary. Gas percolation occurred at the gas saturation S_g=0.21. (c) Gas expansion at S_g=0.50. Note that only gas pores are shown as red color. Tubes in isolated gas clusters are colored as light red, and tubes in percolated gas clusters are colored as blue.

Relative water and gas permeability results are shown in Figure 2.3. As water is drained by expanding gas, relative water permeability decreases (Figure 2.3a). Relative water permeability obtained by using different initial hydrate saturations are almost identical for a given water saturation. However, the relative gas permeability is dependent on the initial hydrate saturation (Figure 2.3b). The simulation results of the cases using lower initial hydrate saturation show higher relative gas permeability at a given gas saturation, and gas percolation at lower gas saturation. Gas percolation occurs at $S_g \approx 0.21$ for S_h=0.1 and $S_g \approx 0.29$ for S_h=0.2. For the case of higher initial hydrate saturation such as S_h=0.4 or 0.6, gas permeability is already developed as soon as hydrates dissociate. The residual water saturation ranges from S_{rw}=0.12 for S_h=0.1 to S_{rw}=0.16 for S_h=0.6, which is the saturation of isolated water that does not have a drainage path.

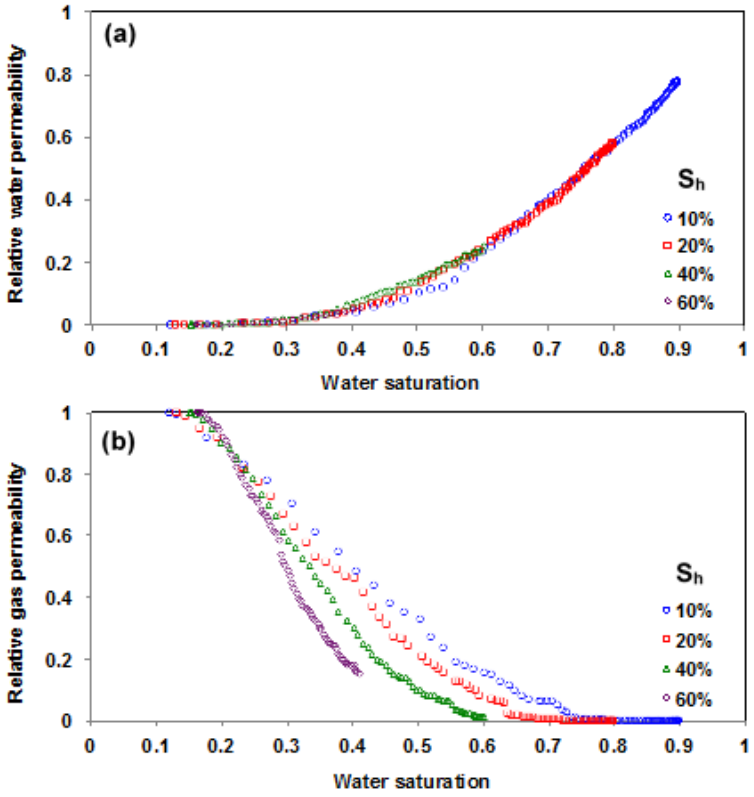

Figure 2.3 Relative water and gas permeability from pore network model simulation using initial hydrate saturation S_h=0.1, 0.2, 0.4, and 0.6. (a) Relative water permeability. (b) Relative gas permeability.

2.5 Analyses and Discussion

The method of least squares is used to fit modified Stone equations (Equation 2.1&2.2) to the relative water and gas permeability data of the pore-network model simulation. The suggested fitting parameter n_w of relative water permeability for each initial hydrate saturation case is shown in Figure 2.4 (The information of residual water saturation S_{rw} used for curve fitting is described in the figure caption). The n_w-values range from n_w=2.2 to 2.6. The values do not show any typical correlation with initial hydrate saturation. The averaged value is n_w=2.4, which is slightly smaller than the n_w-values (e.g., n_w=3.0~4.5) used in other hydrate simulation studies. Higher n_w-value means lower relative water permeability at a given water saturation.

The fitting parameter n_g for relative gas permeability increases as the initial hydrate saturation increases: n_g=1.8 for S_h=0.1, n_g=2.2 for S_h=0.2, n_g=3.0 for S_h=0.4, n_g=3.5 for S_h=0.6 (Figure 2.5 – The information of residual water saturation S_{rw} and residual gas saturation S_{rg} used for curve fitting is described in the figure caption). The hydrate saturation-dependent n_g-value follows a power equation:

$$n_g = \frac{1}{1.35} S_h^{0.38} \quad \text{for} \quad 0.1 < S_h < 0.6 \tag{2.5}$$

The obtained n_g-values for high initial hydrate saturations (e.g., n_g=3.0 and 3.5 for S_h=0.4 and 0.6, respectively) are within the range of the n_g-values (e.g., n_g=3.0~4.0) used in the literature [Reagan and Moridis, 2008; Moridis and Kowalsky, 2005; Moridis et al., 2007, 2009; Moridis and Regan, 2007a, 2007b; Moridis and Sloan, 2007; Rutqvist and Moridis, 2007, 2009; Anderson et al., 2011; Kurihara et al., 2011]. The initial hydrate saturation used for gas production study in the literature is S_h>0.5 [Moridis and Kowalsky, 2005; Moridis et al., 2007, 2009; Moridis and Regan, 2007a, 2007b; Rutqvist and Moridis, 2007, 2009; Anderson et al., 2011; Kurihara et al., 2011].

The reason of low n_g-value and early gas permeability development for low initial hydrate saturation condition can be explained by the different spatial distribution of gas pores for each initial hydrate saturation cases. For the case of initial hydrate saturation S_h=0.1, gas expansion into neighboring water pores inherently makes interconnected gas pores, called a gas cluster. With further depressurization, several gas clusters become interconnected to each other, and finally form a gas percolation path. Further gas expansion beyond gas percolation threshold results in increasing gas permeability. However, for the case of initial hydrate saturation S_h=0.2, initially hydrate pores are individually distributed,

which means gas pores are also individually distributed. Therefore, the gas pore distribution when gas saturation is S_g=0.2 for the case of S_h=0.1 has more interconnected gas pores compared to the gas pore distribution at S_g=0.2 for S_h=0.2 case, which later results in higher gas permeability at a given gas saturation beyond gas percolation threshold. This can also explain the delayed gas percolation for higher hydrate saturation cases.

For higher initial hydrate saturation cases S_h=0.4 or 0.6, the initially distributed hydrate pores (that will become gas pores later) are already interconnected, which means initially developed gas permeability. But, the gas permeability for higher initial hydrate saturation cases is lower than the gas permeability for lower initial hydrate saturation cases at the same gas saturation.

Pore network model simulation shows that gas permeability starts to evolve at $S_g \approx 0.21$ for S_h=0.1 and $S_g \approx 0.29$ for S_h=0.2 (Figure 2.5) while the modified Stone equation (Equation 2.2) predicts gas permeability develops at residual gas saturation S_{rg} (Typical residual gas saturation used in hydrate simulation studies in the literature is S_{rg}=0.02 which is also used in this study for curve fitting). Therefore, if the relative gas permeability obtained by modified Stone equation is compared to the results of pore network model simulation, the modified Stone equation overestimates the relative gas permeability k_{rg} when $k_{rg}<0.4$ while it underestimates k_{rg} when $k_{rg}>0.4$ (Figure 2.5).

Finally, this study assumes spatially distributed hydrate preferentially filling large pores. The hydrate morphology (distributed-vs.-patchy formation) affect physical properties of hydrate-bearing sediments such as electrical, hydraulic, and thermal

conductivity and bulk modulus [Dai et al., 2012]. Therefore, the effects of hydrate morphology on relative permeability should be explored further.

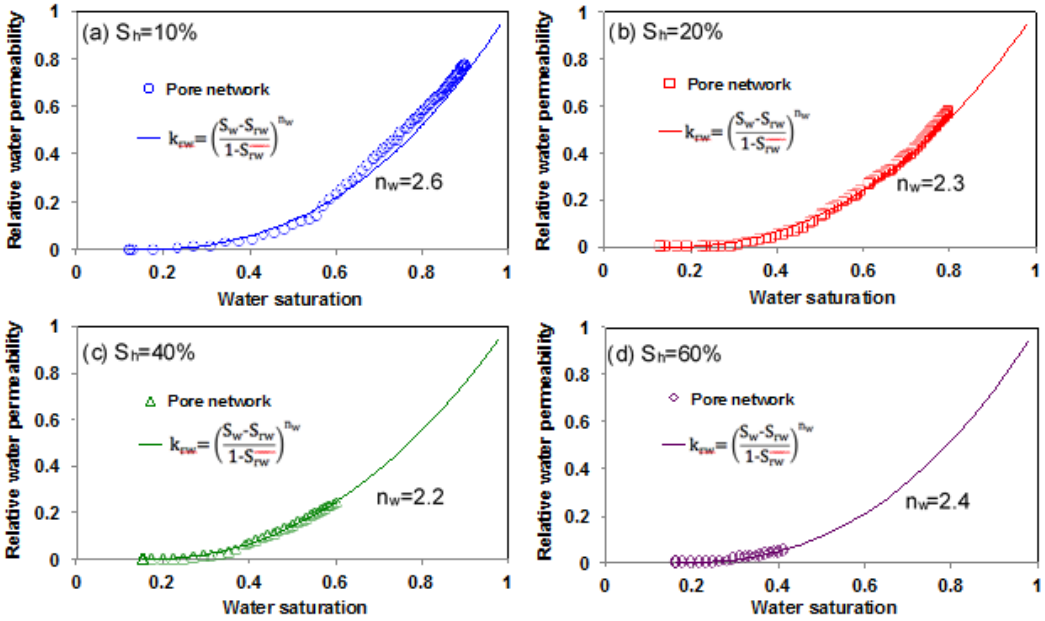

Figure 2.4 Relative water permeability simulation results and fitted curves using Equation 2.1. (a) Initial hydrate saturation S_h=0.1, residual water saturation S_{rw}=0.12, and fitting parameter n_w=2.6. (b) Initial hydrate saturation S_h=0.2, residual water saturation S_{rw}=0.13, and fitting parameter n_w=2.3. (c) Initial hydrate saturation S_h=0.4, residual water saturation S_{rw}=0.15, and fitting parameter n_w=2.2. (d) Initial hydrate saturation S_h=0.6, residual water saturation S_{rw}=0.16, and fitting parameter n_w=2.4. The fitting parameters are obtained by the method of least squares.

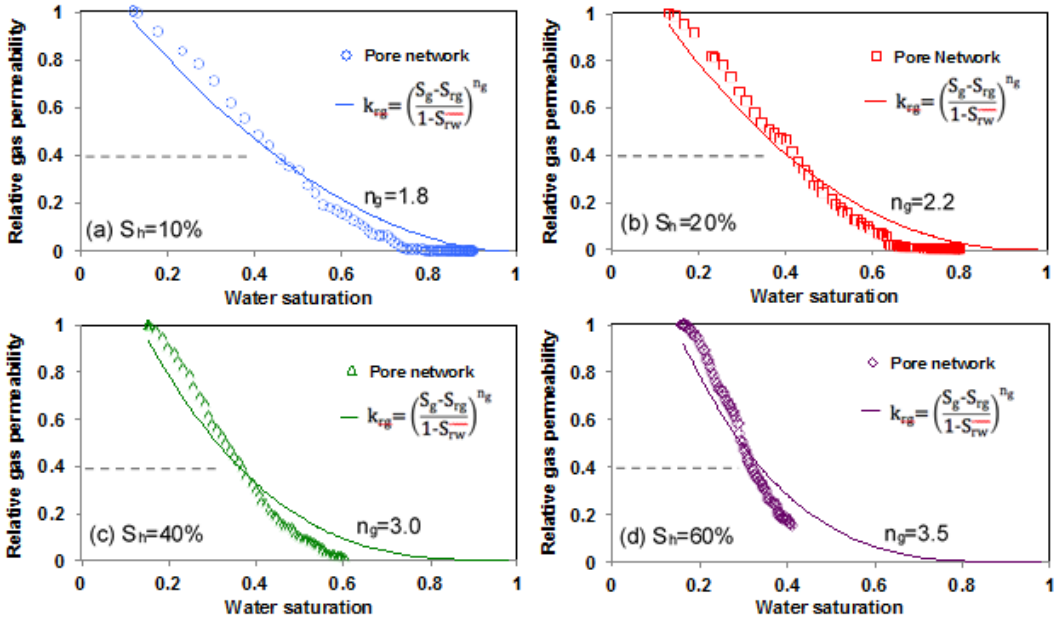

Figure 2.5 Relative gas permeability simulation results and fitted curves using Equation 2.2. (a) Initial hydrate saturation S_h=0.1, residual gas saturation S_{rg}=0.02, and fitting parameter n_w=1.8. (b) Initial hydrate saturation S_h=0.2, residual gas saturation S_{rg}=0.02, and fitting parameter n_w=2.2. (c) Initial hydrate saturation S_h=0.4, residual gas saturation S_{rg}=0.02, and fitting parameter n_w=3.0. (d) Initial hydrate saturation S_h=0.6, residual gas saturation S_{rg}=0.02, and fitting parameter n_w=3.5. The fitting parameters are obtained by the method of least squares.

2.6 Conclusions

The selection of appropriate fitting parameters for relative permeability equations is very important to predict water and gas production from hydrate-bearing sediments. In this study, a pore-network model simulation is performed to suggest proper fitting parameters for modified Stone equation. The results of a pore-network model simulation show that modified Stone equation can be used to predict relative water and gas permeability for the gas production from hydrate-bearing sediments with properly chosen fitting parameters.

The suggested fitting parameter n_w for relative water permeability is n_w=2.4 which is independent on initial hydrate saturations S_h=0.1~0.6. However, the suggested fitting parameter n_g for relative gas permeability varies from n_g=1.8 for S_h=0.1 to n_g=3.5 for S_h=0.6. These fitting parameters are valid for the condition at which hydrate pores are individually distributed, not forming patchy hydrate. The suggested fitting parameter n_g for high initial hydrate saturation condition is within the range of n_g-values used in the literature. The reason of dependency of n_g-value on initial hydrate saturation is explained by the different spatial distribution of gas pores for each initial hydrate saturation condition. The relative water permeability predicted by modified Stone equation is matched well with pore network model simulation results. However, a relative gas permeability curve of modified Stone equation shows a little discrepancy with numerical simulation results such as delayed gas percolation threshold, overestimation for k_{rg}<0.4, and underestimation for k_{rg}>0.4.

Even though the effect of hydrate morphology on relative permeability needs to be considered for more reliable study, this study is the first attempt to suggest fitting parameters of modified Stone equation for gas production from hydrate-bearing sediments. These results and observations are relevant to other natural and engineered systems' phenomena that are caused by gas nucleation from pore fluid of sediments, such as pockmark development due to sea level change, storage capacity change in confined aquifers, gas bubble accumulation at the downstream of dams and ensuing water permeability decrease, and CO_2 gas formation after geological CO_2 sequestration.

CHAPTER 3

THE WATER RETENTION CURVE AND RELATIVE PERMEABILITY FOR GAS PRODUCTION FROM HYDRATE BEARING SEDIMENTS: X-RAY CT SCANNING AND PORE-NETWORK SIMULATION

3.1 Introduction

The fundamental expressions for unsaturated soil behavior are anchored in capillarity and water saturation relation P_c-S_w, typically known as a water retention curve (WRC). The water retention curve essentially captures pore-scale characteristics of the porous media and the gas-fluid-mineral interactions. This curve can be used as an indicator to hydraulic conductivity [Assouline, 2001], soil-water storage [Brady and Weil, 2007], and soil stiffness, strength, and volume changes [Fredlund et al., 1996; Gens and Alonso, 1992; Öberg and Sällfors, 1997; Pedarla et al., 2012]. The relative fluxes of liquid and gaseous phases through porous media are usually captured by relative water and gas permeability k_{rw} and k_{rg}. Both the water retention curve and relative permeability are the most critical characteristics to characterize multiphase flow in porous media.

Widely used models of water retention curve and relative permeability [Bear, 1979; Bear and Cheng, 2010; Brooks and Corey, 1964; Corey, 1954; Parker et al., 1987; Stone, 1970; van Genuchten, 1980] contain multiple fitting parameters. The appropriate selection of these parameter values is critical to enhance the prediction accuracy of water and gas production rates for the development of methane gas hydrate deposits [B J Anderson et al., 2011; Jang and Santamarina, 2011; 2014; Johnson et al., 2011; Kleinberg et al., 2003; Li et al., 2013; Mahabadi and Jang, 2014]. However, this selection has long been a challenge

due to the lack of experimental studies that can precisely control and quantify hydrate saturation throughout the tests. Reported direct measurement of relative water permeability in natural sediments is available for Nankai Trough pressure cores after hydrate dissociation [Santamarina et al., 2015]. Recently, percolation theory has been deployed to characterize relative gas and water permeability in hydrate-bearing sediments [Daigle and Rice, 2015; Ghanbarian et al., 2015]. Yet, none of these studies has been able to capture all the equations and fitting parameters for hydro-thermo-mechanically coupled process analyses in numerical simulators for gas hydrate research [B J Anderson et al., 2011; G Moridis, J et al., 2008].

This study aims to identify proper parameter values for characterizing the water retention curve and relative permeability in hydrate-bearing sediments using the combined techniques of micro-focus X-ray computed tomography (CT) and pore-network model simulation. The sediment recovered from a hydrate deposit at the Mallik site in Canada is remolded and scanned at in situ stress conditions. A three-dimensional pore network is then extracted from the micron-sstion CT images for pore-network simulation. Hydrate is artificially generated in the pores with various saturations and morphology. The processes of gas invasion, hydrate dissociation, and gas expansion during dynamic gas production are simulated to obtain the proper fitting parameter values for water retention curve and relative permeability of water and gas in hydrate-bearing sediments.

3.2 Fundamentals: Water Retention Curve and Relative Permeability Models

The water retention curve is affected by pore throat size distribution, connectivity and spatial correlation, soil fabric, contact angle, and interfacial tension [Dai and

Santamarina, 2013]. Obtaining the water retention curve for sediments with the presence of hydrate faces many experimental challenges, such as long induction time for hydrate formation and poor control of hydrate saturation due to transient hydrate dissolution/dissociation and formation during water and gas flow.

Analytical expressions usually capture the water retention curve using P_c, S_w, and residual water saturation S_{rw} [Brooks and Corey, 1964; Corey, 1954; Fredlund and Xing, 1994; van Genuchten, 1980]. Most numerical studies on gas hydrates [B J Anderson et al., 2011; Gamwo and Liu, 2010; Hong and Pooladi-Darvish, 2003; 2005; G Moridis, J and Reagan, 2007; George Moridis, J and Sloan, 2007; M. T. Reagan et al., 2010; Matthew T. Reagan and Moridis, 2008; Rutqvist and Moridis, 2007] use the van Genuchten [1980] model:

$$P_c=P_0\left[\left(\frac{S_w-S_{rw}}{1-S_{rw}}\right)^{-\frac{1}{m}}-1\right]^{1-m} \tag{3.1}$$

Where P_0 is the gas entry pressure, S_{rw} is the residual water saturation, and m is a fitting parameter. Lower m-value shows steeper P_c-S_w curve (Figure 3.1a), typically in sediments with wider pore size distribution.

Additionally, the van Genuchten [1980] model is used to predict the relative water k_{rw} and gas k_{rg} permeability [Parker et al., 1987]:

$$k_{rw}=\bar{S}^{0.5}\left[1-\left(1-\bar{S}^{1/m}\right)^{m}\right]^{2} \qquad \bar{S}=\left(\frac{S_w-S_{rw}}{1-S_{rw}}\right) \tag{3.2}$$

$$k_{rg}=(1-\bar{S})^{0.5}\left[1-\bar{S}^{1/m}\right]^{2m} \qquad \bar{S}=\left(\frac{S_w-S_{rw}}{S_{wmax}-S_{rw}}\right) \tag{3.3}$$

Where S_{wmax} is the water saturation at which gas permeability starts to occur. A lower m-value depicts lower water permeability but higher gas permeability at a given saturation

(Figure 3.1b).

An earlier relative permeability model (Brooks and Corey [1964]) also frequently used in hydrate simulation studies is:

$$k_{rw} = \left(\frac{S_w - S_{rw}}{1 - S_{rw}}\right)^{n_w} \tag{3.4}$$

$$k_{rg} = \left(\frac{S_g - S_{rg}}{1 - S_{rw}}\right)^{n_g} \tag{3.5}$$

Where S_{rg} is the residual gas saturation, n_w and n_g are fitting parameters for water and gas permeability. Lower n_w and n_g values reflect higher relative water and gas permeability (Figure 3.1c). Note that two individual fitting parameters, n_w and n_g, are used to predict relative water and gas permeability separately in Brooks-Corey model, while one common m-value is used for both water and gas permeability equations in van Genuchten model.

3.3 Methodology

3.3.1 X-ray CT Scanning and Pore-Network Extraction

The sediment used for X-ray scanning was recovered from Mallik 5L-38 site at 1,091meter depth. A sieve analysis was conducted to obtain the grain size distribution (Figure 3.2a, refer also to Jenner et al. [1999] for the grain size distribution of other specimens at this site). This sediment was oven-dried for 48 hours, and then packed in a rubber sleeve (with an inner diameter of 6.35 mm) housed within a high-pressure vessel made out of beryllium for X-ray scanning. The in-situ effective stress (~10MPa) was restored during scanning (Note that this is a remolded sample that does not preserve the original pore structure and connectivity of in-situ sediment, but may have a similar porosity due to restored confining stress). The micro-focus scanner has ~0.68μm per pixel resolution

with 0.7 mm field of view in all three dimensions.

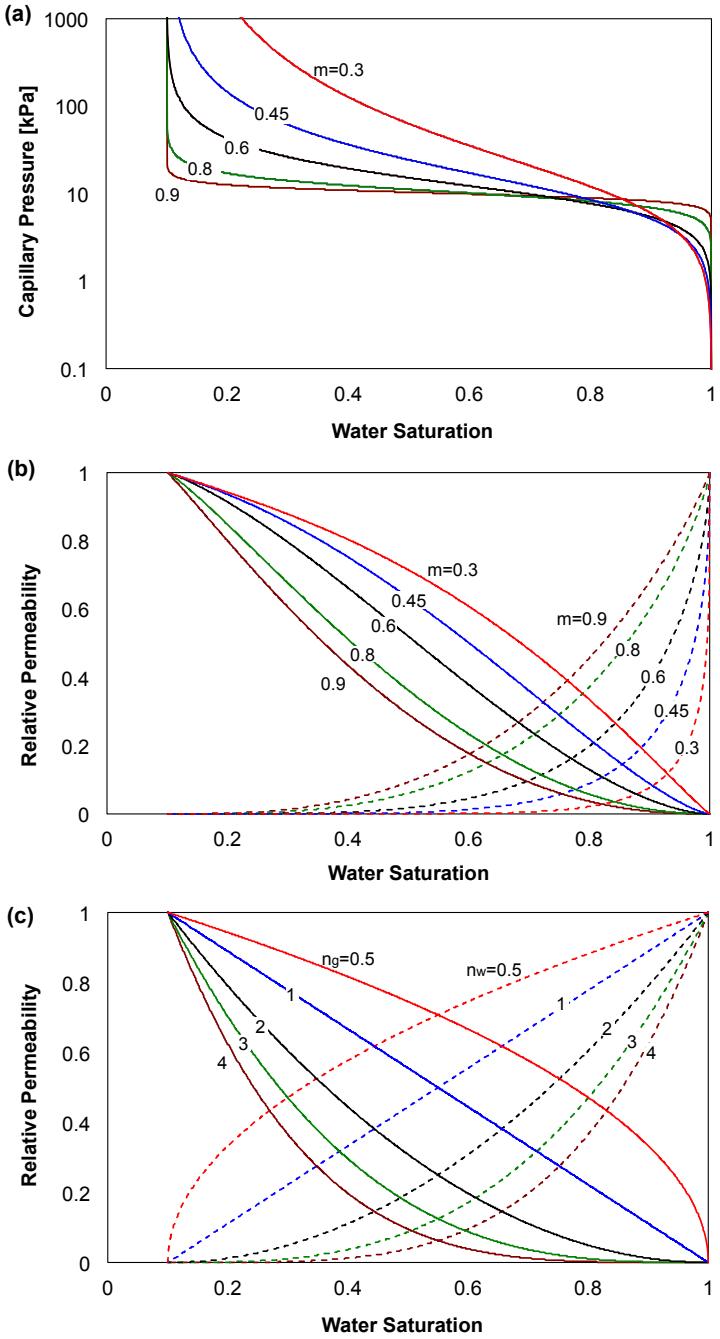

Figure 3.1 Effects of fitting parameters on the water retention curve (P_c-vs-S_w) and relative permeability. (a) Water retention curve using the van Genuchten model (Equation 3.1). (b) Relative permeability using the van Genuchten model (Equations 3.2&3.3). As an m-value increases, relative water permeability increases while relative gas permeability decreases. **(c)** Relative permeability using the Brooks-Corey model (Equations 3.4&3.5). As fitting parameters (n_g and n_w) increase, relative water and gas permeability decrease.

However, we intentionally chose a larger pixel size so the overall scanned volume is large enough to be representative. In this study, the volume of the scanned image is $27mm^3$ (3mm×3mm×3mm) with 12.5μm/pixel resolution. The obtained CT images provide the three-dimensional structure of the scanned sediment, including both the grains and the pore spaces (Figure 3.2b). Then, a three-dimensional pore network consisting of spherical pores and cylindrical tubes (Figure 3.2c) is extracted from the CT images using the maximal ball algorithm developed by Silin and Patzek [2006]. The maximal ball algorithm finds spheres inscribed in the pore wall. As a general rule, big spheres located in the center of pore spaces of the sediment image become pores of the pore-network model and the small spheres inscribed in pore throats are turned into tubes. Further information on inscribing spheres and assigning spheres for pores or tubes is found in Dong and Blunt [2009]. The generated pore-network model can be modified to accurately simulate multiphase fluid flows by changing pore and tube size distribution or considering irregular cross-sectional shape of tubes [Valvatne and Blunt, 2004], but in this study, the extracted pore-network model was used without further modification. Detailed information on the extracted pore-network model is provided in the caption of Figure 3.2.

3.3.2 Hydrate Realization: Saturation and Morphology

Three types of hydrate morphology are found in natural sediments: (1) Pore-filling, (2) lenses/veins, and (3) nodules/chunks [Waite et al., 2009]. The hydrate morphology is determined by the effective stress level of the natural sediments, pore and throat size, and hydrate-water interfacial tension [Clennell et al., 1999; Dai et al., 2012]. In our study, we consider only pore-filling model usually found in coarse-grained sediments.

To achieve target initial hydrate saturation (i.e., S_h=0, 0.2, 0.4, and 0.6 in this study), hydrates are assigned in randomly chosen pores, not in tubes. Hydrate pore selection disregards their size. And it is assumed that the selected pores are entirely filled with hydrates. The assumption of either 100% or 0% pore occupancy by hydrates reflects Ostwald ripening. In a long-term, Ostwald ripening in coarse-grained sediments promotes patchy hydrate formation, whereby hydrate-filled sediment patches (S_h=100%) are embedded in hydrate-free sediments (S_h=0%). Reported data (e.g., P-wave velocity and hydraulic conductivity at different hydrate saturation) and physical analyses suggest hydrate-bearing sands contain a heterogeneous and patchy hydrate distribution [Dai et al., 2012]. And the laboratory observation performed over two weeks for THF hydrate confirms the formation of hydrate patch [Mahabadi et al., 2016].

Based on the fact that hydrate patch size and morphology affects the physical properties of hydrate-bearing sediments in orders of magnitude [Dai and Santamarina, 2013; Dai et al., 2012; Yun et al., 2005], various hydrate morphology are considered in this study: (1) hydrates in individually distributed pores (Figure 3.2d) and (2) hydrates in patchy formations of different sizes, occupying 4, 64, or 1024 pores for a given hydrate saturation (Figure 3.2d). The size of hydrate patch is arbitrarily chosen to explore the effect of hydrate patch size on water retention curve and relative permeability.

Due to hydrate occupancy in pores, the pore connectivity of pore-network model is reduced, which affects residual water saturation as well.

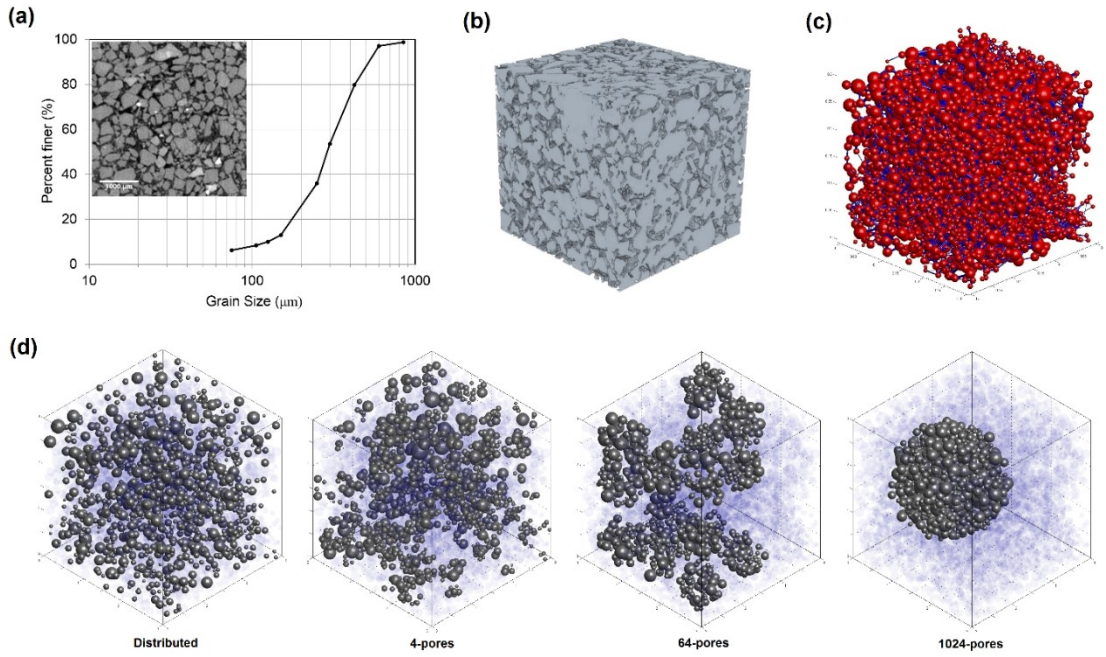

Figure 3.2 Pore-network model generation and hydrate distribution in the pore-network model. (a) Grain size distribution of the specimen recovered from the Mallik 5L-38 site. The soil is classified as poorly graded sand with fines based on the Unified Soil Classification System (ASTM D2487). The coefficient of uniformity is $C_u = D_{60}/D_{10} = 0.33\text{mm}/0.13\text{mm} = 2.6$ and the coefficient of curvature is $C_c = D^2_{30}/(D_{10}D_{60}) = (0.23\text{mm})^2/(0.13\text{mm}\times 0.33\text{mm}) = 1.2$ (D_x is the particle diameter representing that X percent of the total particles is smaller than D). The inset shows a cross-section of the CT image of the Mallik sand specimen. (b) Three-dimensional representative pore space (3mm×3mm×3mm) obtained by μCT scan. (c) Pore network model extracted from the pore space CT images. The pore network model consists of 5376 pores and 18770 tubes with a mean tube connectivity per pore (coordination number) of cn=6.8. Mean pore radius is $\mu[R_{pore}]=60\mu\text{m}$, mean tube size is $\mu[R_{tube}]=11\mu\text{m}$, and mean tube length is $\mu[L_{tube}]=41\mu\text{m}$ ($\max[R_{pore}]=185\mu\text{m}$, $\min[R_{pore}]=21\mu\text{m}$, $\max[R_{tube}]=50\mu\text{m}$, $\min[R_{tube}]=1\mu\text{m}$, $\max[L_{tube}]=190\mu\text{m}$, $\min[L_{tube}]=0.04\mu\text{m}$) (d) Various types of hydrate morphology (distributed vs. patchy) for a given hydrate saturation $S_h=0.2$. Hydrate forms in randomly distributed individual pores, or in patches of different size consisting of 4 pores, 64 pores, and 1024 pores. Note that hydrate pores are shown in gray and water pores in transparent blue.

3.3.3 Water Retention Curves in Hydrate-Bearing Sediments

The water retention curve is obtained by simulating the gas invasion process into water-saturated, hydrate-bearing sediments. Gas invasion is enforced at tubes located on

the inlet boundary. Quasi-static gas invasion controlled by capillarity is assumed so the viscosity effect can be disregarded. If the gas pressure is higher than the summation of the capillary and water pressure of the water-filled tube ($P_g > P_w + P_c$,), the gas can invade the tube. The capillary pressure at gas-water interface in a tube with radius R_{tube} is captured by the Laplace equation $P_c = 2T_s\cos\theta / R_{tube}$, where in this study the water-gas interfacial tension is T_s=0.072 N/m; the contact angle is assumed θ=0° to represent a completely water-wet surface (note: refer to Al-Futaisi and Patzek [2003] for the effects of contact angle on computed relative permeability). With pressure increases, gas starts invading through the largest tube on the inlet boundary. And as capillary pressure increases, gas invades more water-filled tubes, leading to a decrease in water saturation; thus, the water retention curve is computed until water drainage stops.

3.3.4 Relative Permeability after Hydrate Dissociation

Solid hydrate turns into gas and water during hydrate dissociation. Hydrate dissociation and the volume expansion of the dissociated gas is controlled by gradually lowering the pressure at pore-network inlet and outlet boundaries from P=15MPa to 0.1MPa at constant T=287K. The gas volume expansion upon dissociation and during depressurization is computed by the modified Peng-Robinson equation of state [Jang and Santamarina, 2011; Stryjek and Vera, 1986]. The depressurization is kept slow enough so that the endothermic effect during hydrate dissociation is negligible. As soon as the P-T condition comes out of the hydrate phase boundary (P=13.9MPa and T=287K), hydrates start to dissociate. The water from dissociated hydrate is drained out of the pore-network (for all cases, water pores are forming percolating path), but the gas from dissociated

hydrates remains in the pore space that was initially occupied by hydrates. At the P-T condition of P=13.9MPa and T=287K, the volume of the gas dissociated from hydrates is the same as the volume of initial hydrates. Therefore, pores occupied by initially hydrates turn into gas pores (for S_h=0.2 case, the saturations for hydrate, gas, and water prior to dissociation are S_h=0.2, S_g=0, S_w=0.8, respectively, and become S_h=0, S_g=0.2, S_w=0.8, right after dissociation at P=13.9MPa and T=287K). Then, further depressurization allows gas to expand into neighboring water pores. Gas expansion continues as long as gas pressure is higher than the summation of capillary pressure and water pressure, and as long as water drainage path is available. At around water saturation S_w=0.15~0.2, gas expansion stops mainly due to the loss of water drainage path.

The methane solubility in water without hydrate is assumed zero due to relatively small methane solubility in water compared to large methane amount contained in methane hydrates. The gas expansion algorithm and water and gas permeability calculation during each gas expansion step are explained in detail in the authors' previous publication [Jang et al., 2011; Jang and Santamarina, 2011; Mahabadi and Jang, 2014].

3.4 Simulation Results

3.4.1 Computed Water Retention Curves

Figure 3.3a shows the computed retention curves in sediments with various initial hydrate saturations, i.e., S_h=0, 0.2, 0.4 and 0.6. Hydrates (black spheres Figure 3.3a-inset) are randomly distributed in individual pores. One simulation run is performed for S_h=0 case and five simulation runs for each of other S_h>0 cases. All cases use the identical pore-network. The process of gas invasion into the hydrate-bearing pore network model is

illustrated as red spheres in the Figure 3.3a-inset. As the initial hydrate saturation increases, the gas-entry pressure increases, and the capillary pressure at a given water saturation also increases. The higher initial hydrate saturation condition results in the higher residual water saturation.

Figure 3.3b shows the computed water retention curves in sediments with the same initial hydrate saturation (S_h=0.2) but different hydrate patch size (i.e., the hydrate patch is composed of 4, 64, and 1024 pores). Three simulation runs are performed for each patch size and the spatial distribution of hydrate patch varied at each simulation. Sediments with larger hydrate patches tend to result in lower gas-entry pressure and also slightly lower residual water saturation (Figure 3.3b).

3.4.2 Relative Permeability during Gas Expansion

Figure 3.4 illustrates the gas expansion and water drainage processes during gas expansion in sediments with initial hydrate saturation S_h=0.2 (S_h=0 and S_w=0.8). All the hydrates dissociate into gas (S_g=0 and S_w=0.8, first column in Figure 3.4). And gas expands with further depressurization (second, third, and fourth columns in Figure 3.4). With further gas expansion, water continues draining, but gas conductivity does not occur until the gas phase forms a percolation path at gas saturation S_g=0.3 (second column in Figure 3.4). Later, the water phase gradually loses percolation paths, and the gas phase builds more gas flow paths (third column in Figure 3.4a). Eventually, gas keeps expanding into neighboring water-filled pores until water drainage stops at S_g=0.86 and S_w=0.14=S_{rw} (fourth column in Figure 3.4a).

The relative permeability of water (or gas) is the conductivity at a given water

saturation normalized by the water (or gas) conductivity at 100% water (gas) saturation. The gas conductivity at the residual water saturations can be also used for normalization.

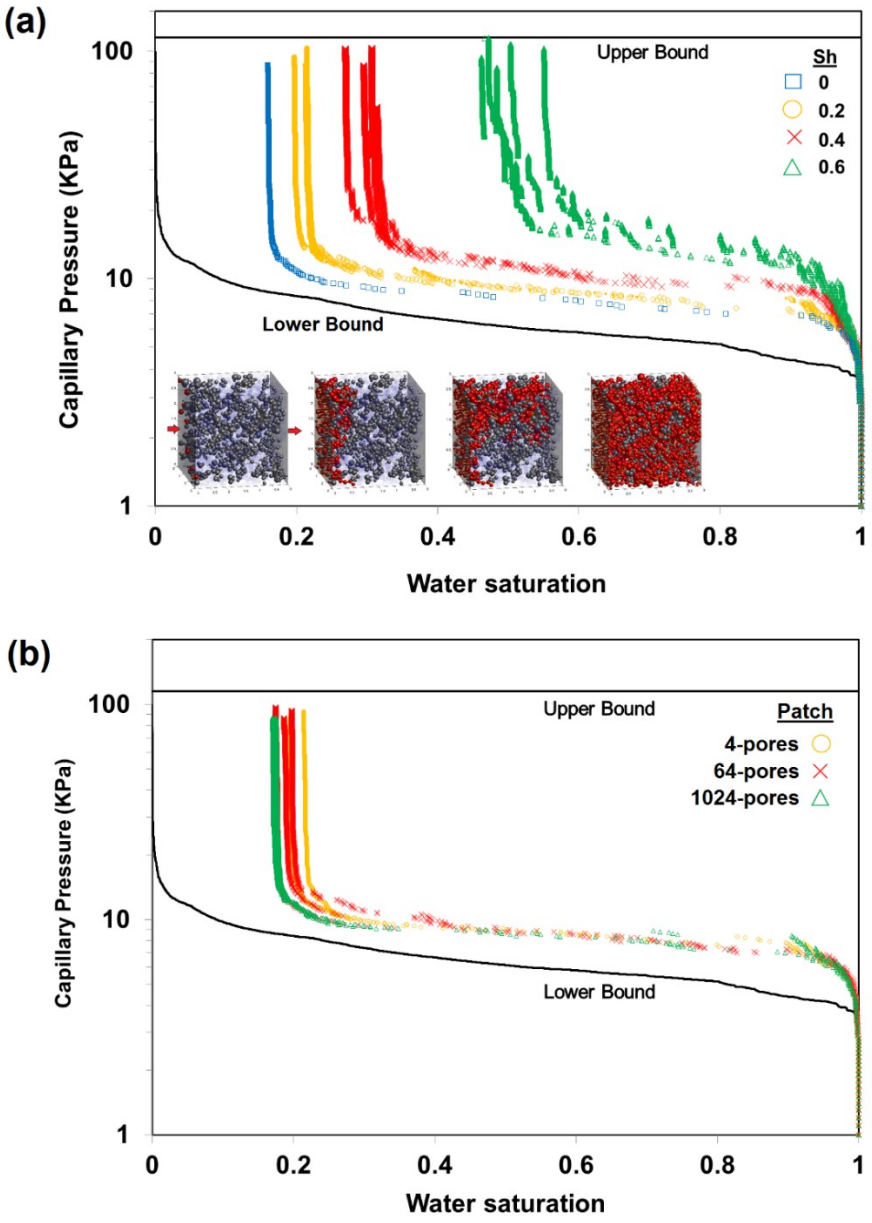

Figure 3.3 Water retention curves in hydrate-bearing sediments. (a) Effects of hydrate saturation (S_h=0, 0.2, 0.4, and 0.6) on computed water retention curves. Upper and lower bounds are obtained by injecting gas into tubes arranged in a series forming a single line from smallest to largest (upper bound) or in parallel (lower bound). Inset figures show gas invasion into the hydrate-bearing pore-network from left to right boundary. Note that gas pores are colored red, hydrate pores gray, and water pores transparent blue. (b) Effects of hydrate morphology (all at constant hydrate saturation S_h=0.2) on water retention curves.

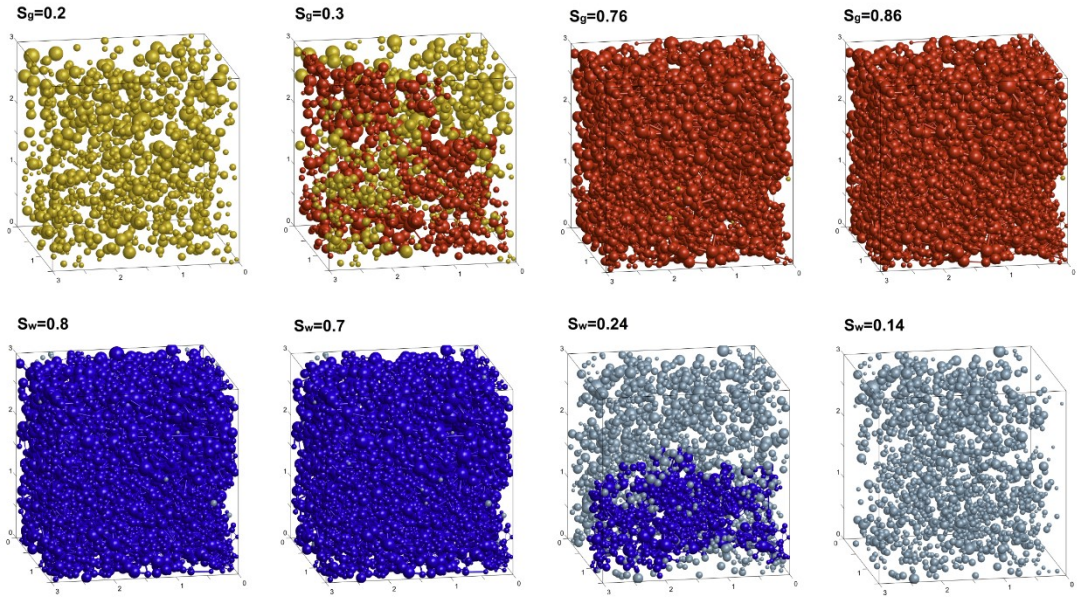

Figure 3.4 Illustrations of gas and water flow processes during gas expansion in sediment undergoing hydrate dissociation (S_h=0.2). Note that gas pores forming conductivity paths are colored red, and isolated gas pores are colored yellow in upper figures. Water pores forming conductivity paths are colored blue, and isolated water pores are colored light blue in lower figures.

In order to explore the effect of hydrate saturation and patch formation on relative water and gas permeability, the water (or gas) conductivity at a given water saturation is normalized by the water (or gas) conductivity at 100% water (or gas) saturation (left figures in Figure 3.5a&b). However, in order to fit van Genuchten and Brooks-Corey equations, the gas conductivity at the residual water saturation is used for normalization (right figures in Figure 3.5&b).

Results show that relative gas permeability increases, and relative water permeability decreases as gas expands into water-filled pores (Figure 3.5). As shown in left figure in Figure 3.5a, sediments with lower initial hydrate saturation result in (1) higher relative gas permeability and (2) lower residual water saturation. This trend of relative gas and water permeability as a function of initial hydrate saturation is consistent with

published results [Mahabadi and Jang, 2014]. Higher gas connectivity developed for lower hydrate saturation conditions can explain this trend.

Additionally, with the increase in hydrate patch's size, both water and gas permeability increases dramatically particularly for S_w>0.4 (left figure in Figure 3.5b). When the water saturation is lower than S_w=0.4, the effect of hydrate patch size on relative gas and water permeability becomes insignificant. Moreover, larger patch size results in lower residual water saturation.

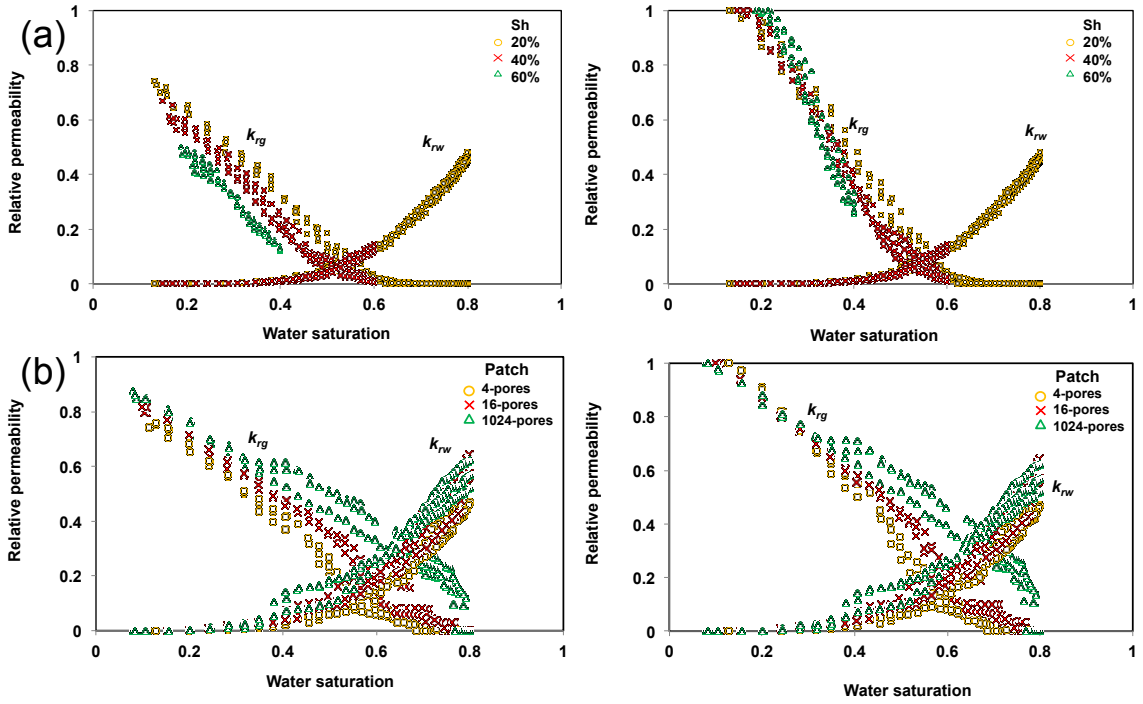

Figure 3.5 Relative permeability in hydrate-bearing sediments. (a) Effect of hydrate saturation on relative gas and water permeability for initial hydrate saturations S_h=0.2 (yellow), 0.4 (red) and 0.6 (green). Five simulation runs are performed for each hydrate saturation condition. (b) Effect of hydrate patch size on relative gas and water permeability. Three simulation runs are performed for each size of hydrate patch: 4 pores (yellow), 64 pores (red) and 1024 pores (green). The hydrate saturation is S_h=0.2. Note that in left figures, the water (or gas) conductivity is normalized by the water (or gas) conductivity at 100% water (or gas) saturation, however, the gas conductivity at the residual water saturation is used to normalize gas conductivity in right figures.

Gas conductivity values are normalized by the gas conductivity at the residual water saturation for each simulation run in order to fit the van Genuchten equation and Brooks-Corey equation (right figures in Figure 3.5a&b).

3.5 Analyses and Discussions

3.5.1 Pore-Network Model Simulation—Relevance to Experimental Tests

The shape of pore geometry in real sediments is irregular, while the pore-network model composed of cylindrical tubes and spherical pores simplifies the real pore geometry of sediments, which can result in differences between numerical simulation and experimental study. For example, the maximum ball algorithm used for pore-network model extraction finds spheres inscribed onto the pore surface [Dong and Blunt, 2009]. Therefore, the cross-sectional area of tubes tends to be smaller than the actual cross-sectional area of real pore throats. The simulation results obtained by using the Lattice Boltzman Method show that the capillary pressure of the cylindrical tube inscribed in other tubes with polygonal cross-sectional shape is smaller than the capillary pressure of polygonal shape tubes [Mahabadi et al., 2015]. In addition, the process of finding inscribed spheres for various pore throat shapes may result in homogenization of pore throat size distribution of real sediments. Therefore, water retention curves obtained from the pore-network model may show more uniform pore throat size distribution, which increases m-value in the P_c-vs-saturation curve, as shown in Figure 3.1a.

3.5.2 Flow in Hydrate-Bearing Sediments—Recommended Parameter Values

The method of least squares is used to fit the Equations 3.1~3.5 to the water retention curves and relative permeability simulation results. When the least square method

is applied to the unevenly distributed data points, biased fitting parameters can be obtained. Therefore, a median curve is found for distributed data. Then, evenly distributed data points on the median curve are used for the least squares method to find fitting parameters with a minimum L2-norm. Fitting parameters are calculated at each individual simulation run for each initial hydrate saturation condition and each hydrate morphology case. Then, the averaged fitting parameters of 5 or 3 simulation runs are obtained.

Table 3.1a summarizes the best fitting values for the van Genuchten model and the Brooks-Corey model based on the simulations. The results of water retention curve simulation suggest that the three parameters in the van Genuchten WRC model (i.e., P_0, S_{rw}, and m) depend on hydrate saturation: increased hydrate saturation in sediments leads to (1) higher gas entry pressure P_0, (2) higher residual water saturation S_{rw}, and (3) steeper P_c-S_w curve (meaning lower m value). For patchy hydrate formation, as the size of hydrate patch increases for a given hydrate saturation, the m-value increases slightly (from m=0.91 to 0.92), and the gas-entry pressure decreases (Table 3.1a). The gas-entry pressure for the largest hydrate patch case (a patch consisting of 1024 pores) is P_0=8.0kPa which is as low as the gas-entry pressure of the hydrate-free sediment. It is obvious that sediments with heterogeneous hydrate distribution tend to have lower gas entry pressure than those with uniformly distributed hydrate.

The relative water and gas permeability during gas expansion also depend on both hydrate saturation and hydrate morphology. During hydrate dissociation, gas expands into the neighboring water-filled pores and forms interconnected clusters, which further interconnect to each other to become larger gas clusters and eventually percolate through the porous media. In sediments with distributed hydrate, the gas permeability of the

sediment with higher S_h is lower than that of the sediment with lower S_h (Figure 3.5a), due to less interconnected gas clusters in a higher S_h case than that in a lower S_h case. Hydrate morphology has even more significant effect on the gas permeability (Figure 3.5b). At a given saturation, the relative gas permeability increases dramatically as the size of hydrate patch increases, e.g., k_{rg} = ~0.5 in the case of a larger hydrate patch (1024-pore size), but k_{rg} = ~0.1 in the case of a smaller hydrate patch (4-pore size) at around S_w=0.55. However, the variance in gas permeability due to hydrate morphology diminishes toward residual water saturation, i.e., at gas saturation S_g > ~0.7 or water saturation S_w < ~0.3.

With regard to water permeability, initial hydrate saturation in sediments with uniformly distributed hydrate has marginal effect. But in sediments with a patch hydrate, larger hydrate patch results in higher relative water permeability because gas expansion from larger hydrate patches has less effect on plugging water paths than does a smaller hydrate patch or distributed hydrates.

More importantly, the simulation results also suggest that using one common fitting parameter m-value in the van Genuchten model for both gas and water permeability is not appropriate to characterize the water/gas flows during gas production from hydrate deposits. In sediments with uniformly distributed hydrate, the m-value for both gas and water permeability decreases with increasing hydrate saturation. Under identical hydrate saturation (S_h = 0.2 in this case, Table 3.1b) but various hydrate morphology, however, the m-values for gas and water permeability show evident discrepancies; and sediments with larger hydrate patches tend to result in lower residual water saturation S_{rw}, and higher gas and water permeability (Table 3.1b). In this sense, the Brooks-Corey model that has two different fitting parameters specifically for gas n_g and water n_w permeability appropriately

predict the flows in sediments with patchy hydrate. The fitting parameter values for the Brooks-Corey model for sediments with various hydrate saturation and morphology are listed in Table 3.1a.

3.6 Conclusions—Recommendations

Based on the results and analyses in this study, we propose the following recommendations for selecting proper parameters and their values (summarized also in Table 3.1b) when characterizing gas and water flows in sediments during hydrate dissociation:

- For water retention curves in hydrate-bearing sediments, the air-entry pressure P_0, residual water saturation S_{rw}, and m-value of the van Genuchten model depend on hydrate saturation S_h. The effect of hydrate patch size on the WRC steepness m is negligible, particularly at S_h=0.2.
- In relative permeability characterization using the van Genuchten model, the residual water saturation S_{rw} and maximum water saturation S_{wmax} should be corrected by considering hydrate saturation S_h. Also, the same m-value can be used for both gas and water permeability, but only in sediments with uniformly distributed hydrate; hydrate morphology greatly impacts the m-value for gas permeability.

The Brooks-Corey model characterizes the gas and water permeability using two separate parameters. Hydrate saturation slightly affects the fitting parameter for water permeability; but the gas permeability must be corrected at different hydrate saturation S_h. Again, hydrate morphology dramatically affects the gas permeability. In particular, a more heterogeneous specimen (with a larger hydrate patch) tends to result in both higher gas and water permeability.

Table 3-1 Fitting parameters for water retention curves and relative permeability: (a) numerical results and (b) recommendations. Note: HBS = hydrate-bearing sediments; HFS = hydrate-free sediments.

(a)	van Genuchten model							Brooks-Corey model		
	Water Retention Curve			Relative Permeability						
S_h	P_0 [kPa]	S_{rw}	m	S_{rw}	S_{wma}	m_g	m_w	S_{rw}	n_g	n_w
0	8.0	0.16	0.91							
0.2	8.7±0.2	0.21±0.01	0.90±0.01	0.14±0.02	0.80	0.87±0.00	0.88±0.01	0.14±0.02	2.6±0.1	3.1±0.1
0.4	10.2±0.4	0.29±0.02	0.87±0.01	0.17±0.01	0.75	0.85±0.01	0.85±0.01	0.17±0.01	3.1±0.1	3.3±0.1
0.6	13.8±0.5	0.49±0.04	0.81±0.01	0.20±0.01	0.60	0.80±0.01	0.80±0.02	0.20±0.01	3.5±0.1	3.3±0.2
Patch size (at S_h = 0.2)										
4-pore	8.6±0.2	0.20±0.01	0.91±0.01	0.12±0.01	0.80	0.70±0.01	0.89±0.01	0.12±0.01	2.1±0.1	3.1±0.2
64-pore	8.4±0.2	0.19±0.01	0.91±0.01	0.10±0.00	0.80	0.55±0.02	0.97±0.02	0.10±0.00	1.6±0.1	2.6±0.2
1024-pore	8.0±0.2	0.17±0.00	0.92±0.01	0.08±0.00	0.80	0.25±0.03	1.07±0.02	0.08±0.00	1.1±0.2	2.3±0.2

(b)			Uniformly distributed hydrate	Note: impacts of heterogeneously distributed/patchy hydrate
van Genuchten model	WRC	P_0	$P_0^{HBS} = P_0^{HFS}\left(1+S_h\right)$	Lower P_0
		S_{rw}	$S_{rw}^{HBS} = S_{rw}^{HFS}\left(1+5S_h\right)$	Lower S_{rw} with increasing patch size
		m	$m^{HBS} = m^{HFS}\left(1-0.15S_h\right)$	Negligible impact when S_h=0.2
	Relative Permeability	S_{rw}	$S_{rw}^{HBS} = 0.1+0.17S_h$	Lower S_{rw}
		S_{wmax}	$S_{w\max}^{HBS} = 1-0.7S_h$	No impact
		m_g	$m^{HBS} = m^{HFS}\left(1-0.19S_h\right)$	Significantly lower m_g, decreasing with increasing patch size
		m_w		Higher m_w, increasing with increasing patch size
B-C model	Relative Permeability	S_{rw}	$S_{rw}^{HBS} = 0.1+0.17S_h$	Lower S_{rw} =~ 0.1
		n_g	$n_g^{HBS} = 2+2.6S_h$	Significantly lower n_g, $n_g^{HBS} = 1+2.6S_h$
		n_w	$n_w^{HBS} =\sim 3-3.5$	Lower n_w, $n_w^{HBS} =\sim 2-3$

CHAPTER 4

THE EFFECT OF HYDRATE SATURATION ON WATER RETENTION CURVES IN THF HYDRATE-BEARING SEDIMENTS: EXPERIMENTAL STUDY

4.1 Introduction

The water retention curve (WRC) describes the amount of water retained in sediments at a given capillary pressure. Expression for capillary pressure as a function of water saturation requires multiple fitting parameters. Several analytical models have been proposed to describe the water retention curve [Brooks and Corey, 1964; Corey, 1954; Fredlund and Xing, 1994; van Genuchten, 1980]. Among them, van Genuchten [1980] model is widely used for various sediment types in many other gas hydrate simulation studies [B J Anderson et al., 2011; Gamwo and Liu, 2010; G Moridis, J and Reagan, 2007; George Moridis, J and Sloan, 2007; M. T. Reagan et al., 2010; Matthew T. Reagan and Moridis, 2008; Rutqvist and Moridis, 2007; Wilder et al., 2008]:

$$P_c = P_0 \left[\left(\frac{S_w - S_{rw}}{1 - S_{rw}} \right)^{-\frac{1}{m}} - 1 \right]^{1-m} \tag{4.1}$$

Where P_c is the capillary pressure, S_w is the water saturation, S_{rw} is the residual water saturation, P_0 is the gas entry pressure and m is the fitting parameter. A lower m-value results in steeper P_c-S_w curve, typically in sediments with wide pore size distribution. In addition, the fitting parameter m-value is also used to predict relative water k_{rw} and gas k_{rg} permeability as shown below [Parker et al., 1987; van Genuchten, 1980]:

$$k_{rw} = \bar{S}^{0.5} \left[1 - \left(1 - \bar{S}^{1/m} \right)^m \right]^2 \qquad \bar{S} = \left(\frac{S_w - S_{rw}}{1 - S_{rw}} \right) \tag{4.2}$$

$$k_{rg}=(1-\bar{S})^{0.5}\left[1-\bar{S}^{1/m}\right]^{2m} \qquad \bar{S}=\left(\frac{S_w-S_{rw}}{S_{wmax}-S_{rw}}\right) \tag{4.3}$$

Where S_{wmax} is the water saturation at which gas permeability starts to occur. A lower m-value depicts lower water permeability but higher gas permeability. It should be noted that only one m-value is used for water retention curve, relative water and gas permeability equations.

The water retention curve is a crucial function to characterize the behavior of unsaturated sediments. The appropriate selection of fitting parameter m-value for the water retention curve in hydrate numerical simulators is important to understand coupled processes during hydrate dissociation and gas production from hydrate-bearing sediments [Dai and Santamarina, 2013; Jang and Santamarina, 2014]. However, there are not many experimental studies to help the selection of the fitting parameters in the literature (see the work done by Ghezzehei and Kneafsey [2010]). In this study, the formation of tetrahydrofuran (THF) hydrates is observed at pore-scale. And, a series of fitting parameter m-value of van Genuchten equation is obtained from the water retention curve measurements for THF hydrate-bearing sediments.

4.2 Experimental Details

In this study, THF hydrates are formed in a transparent micromodel for pore-scale observation and in a pressure chamber for water retention curve measurement. The properties of THF hydrates and volume change during formation are described in the following section.

4.2.1 THF Hydrates

There are many challenges in forming methane hydrate in a laboratory such as long induction time, low methane solubility in water, the loss of water percolation to achieve high hydrate saturation condition (e.g., S_h>80%), and dynamic/transient hydrate formation and dissolution under water-saturated condition. In order to avoid these challenges, tetrahydrofuran (C_4H_8O) is chosen as a surrogate of hydrate-forming gas. THF hydrates are stable under atmospheric pressure. And the equilibrium temperature for THF hydrates depends on the weight fraction of water in water-THF solution (Figure 4.1). Moreover, water and THF are miscible. Therefore, it is easy to control THF hydrate saturation by changing the mixture ratio between water and THF.

Water and THF form structure II hydrate ($8C_4H_8O \bullet 136H_2O$) that consists of 8 large cages (L-cage) and 16 small cages (S-cage). THF molecules can occupy only large cage, and small cage is empty; 8 THF molecules and 137 water molecules are required for the unit of structure II hydrate for 100% large cage occupancy. For example, by weight ratio, the solution of 80.9 weight% water and 19.1 weight% THF forms 100% THF hydrates. The molecular mass of water is M_{H2O}=18.02g/mol and the molecular mass of THF is M_{THF}=72.107g/mol [Mellan, 1977].

Assuming that all 8 large cages are occupied by THF molecules, the density of THF hydrate is estimated to be $\rho_{THF\text{-}H}=(8\times M_{THF}+136\times M_{H2O})/(N_A\times V_{sII})=0.981 g/cm^3$ where N_A is the Avogadro's number $N_A=6.022\times10^{23}$ [mol^{-1}] and V_{sII} is the volume of structure II hydrate $V_{sII}=(17.24Å)^3$ at 4°C [Gough and Davidson, 1971]. And the density of pure liquid THF is $\rho_{THF\text{-}L}=0.888 g/cm^3$ at 20°C [Mellan, 1977]. The measured density of the THF and

water solution consisting of 1 mole of THF and 17 moles of water is $\rho_{THF+WATER}$=0.997g/cm^3 at the temperature ~4°C [Gough and Davidson, 1971]. Based on the density of THF hydrate calculated above, the volume expansion upon THF hydrate formation from the THF-water solution (1:17 mole ratio) is estimated to be $V_{THF-H}/V_{THF+WATER}=\rho_{THF+WATER}/\rho_{THF-H}$=0.997/0.981=1.016 (1.6% volume expansion) where V_{THF-H} is the volume of THF hydrate and $V_{THF+WATER}$ is the volume of THF-water solution prior to hydrate formation. This phenomenon is captured by the volume expansion of THF hydrate-bearing sediments under zero-lateral strain condition [Lee et al., 2010].

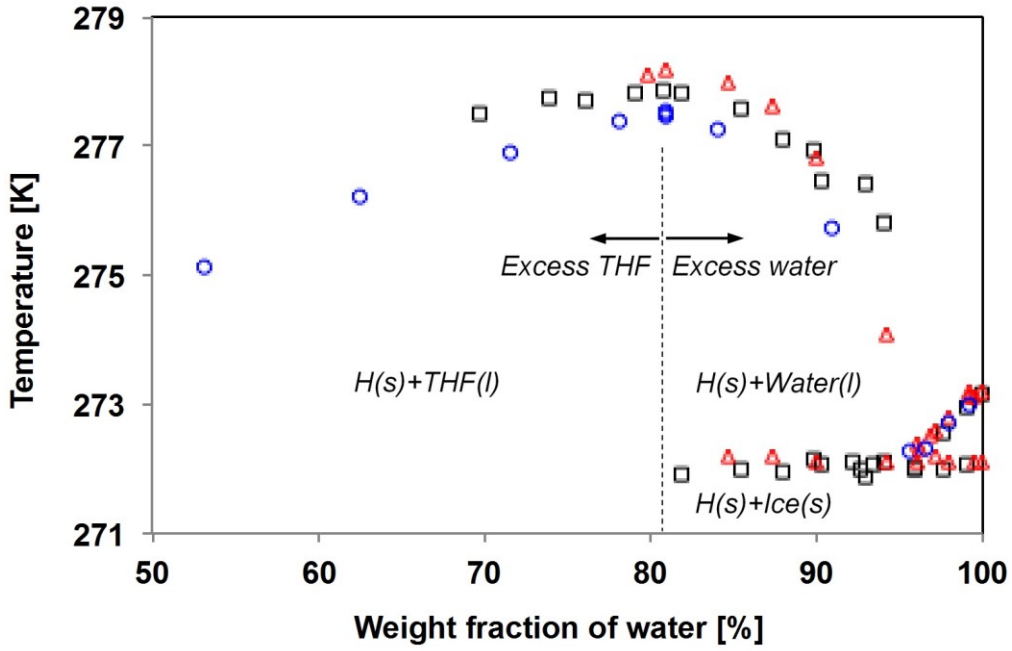

Figure 4.1 Equilibrium temperature of THF hydrate as a function of water fraction in THF-water solution. Experimentally measured equilibrium temperature points are shown as symbols: red triangle [R Anderson et al., 2007], black square [Delahaye et al., 2006], blue circle [Makino et al., 2005].

4.2.2 Micromodel Experiment

A transparent pressure-resistant quartz micromodel (Micronit microfluidics, Netherland) is fabricated to observe THF hydrate formation (Figure 4.2a). The micromodel

is placed inside the environmental chamber (Sigma Systems, C5 model). The solution of water and THF (Fisher Scientific, purity 99.9%) is dyed as blue by methyl blue (Sigma-Aldrich, the used concentration of methyl blue in water is 0.15weight%) to increase image contrast; the color of water and THF solution is initially blue, and after hydrate formation, the portion of THF hydrates becomes transparent due to ion exclusion and the color of pore water becomes dark blue. A solution consisting of 90.5weight% water and 9.5weight% THF resulting in hydrate saturation S_h=0.5 is injected into the micromodel using a stainless steel syringe (Analytical West Inc, 2.5mL). After the solution is injected, two valves connected to inlet and outlet ports of the micromodel are closed to prevent THF evaporation and fluid flow. Then, the temperature of the environmental chamber decreases down to -8°C to facilitate hydrate nucleation. A camera (Nikon, D5100) is placed inside the environmental chamber for time-lapsed photography. Once hydrate formation is observed, the temperature increases up to 1°C to prevent ice formation and maintain THF hydrates within stability zone.

4.2.3 Water Retention Curve Measurement

A pressure chamber (GCTS Testing Systems, Fredlund's Soil Water Characteristic Curve Device) developed for the water retention curve measurement of unsaturated soils is used for this study (Figure 4.2b). The placement of the pressure chamber inside the environmental chamber prevents visual reading of the height of water column for drainage measurement. Therefore, a pressure transducer for low-pressure range (Omega, PX329-002G5V, 2psi) is connected to the bottom of the water column so that the volume of water drained from soil sediment during pressurization is calculated by reading hydrostatic

pressure of the water column. Another pressure transducer (Omega, PX309-030G5V, 30psi) connected to the pressure chamber measures air pressure applied to hydrate-bearing sediments. Therefore, the water retention curve (pressure-vs.-saturation) is obtained by reading values from the two pressure transducers. The pressure of air (Praxair, UN 1002 Breathing grade) inside the chamber is controlled by a precise regulator (Fairchild, 10272N, 20-1400kPa). The capillary pressure of the ceramic porous plate (Soilmoisture Equipment Corp.) placed on the bottom of the pressure chamber is 300kPa that is high enough to perform water retention curves of fine sands. Two k-type thermocouples (Omega, precision of 0.1°C) are used to measure temperatures inside the pressure chamber and inside the soil sediment.

A sediment recovered from the Mallik 5L-38 site in Canada is used for this test. The diameter of median size sand particle is D_{50}=0.29mm. Fine particles smaller than 75μm are removed by wet sieving on #200 sieve, and only sand particles larger than 75μm are used for this test. It is remolded sample and no vertical confining stress is applied. Therefore, the pore structure of this remolded sample is different from the pore structure of original sediment in Mallik site.

In order to run WRC test, first the ceramic porous plate is saturated with the mixture of 90weight% water and 10weight% ethyleneglycol to prevent THF hydrate or ice formation in the pore space of the ceramic plate during the entire test (The temperature of the high pressure chamber decreases below 0°C to facilitate hydrate nucleation). The oven-dried sediment is compacted into a stainless steel cylinder (dimension: 7cm in diameter and 2.5cm in height) by three layers on the saturated ceramic porous plate. The density of the compacted dry sediment is 1.637g/cm^3, and the porosity of the sediment is n=0.38.

During compaction, a tip of the thermocouple is placed in the middle of the sediment to detect temperature spike occurring at the moment of hydrate nucleation and during formation. Once the sediment is compacted, the sediment is saturated with water-THF solution. The used weight fractions of water in the water-THF solution are 1, 0.92, 0.89, 0.87 and 0.85 which results in THF hydrate saturation S_h=0, 0.4, 0.6, 0.7 and 0.8, respectively. After the saturation process is completed, the pressure chamber is assembled and placed inside the environmental chamber. Then, the temperature of the environmental chamber decreases down to -5°C to facilitate hydrate nucleation. After a temperature spike is observed (meaning hydrate nucleation), a temperature of the sediment is increased to 1°C and maintained for 14 days for complete conversion of THF to THF hydrates. After 14 days, the air pressure of the pressure chamber is gradually increased and remained constant at each pressure-level until there is no volume change of drained water. The maximum air pressure applied to the pressure chamber is 200kPa that is 100kPa lower than the capillary pressure of the ceramic porous plate. And, in addition to four different hydrate saturation cases (S_h=0.4, 0.6, 0.7, and 0.8), a water retention curve for hydrate-free sediment (S_h=0) is also obtained. The case of hydrate saturation lower than S_h=0.4 is not tried because low equilibrium temperature for excess water condition (Figure 4.1) gives the possibility of forming ice. The pore fluid remaining after THF hydrate formation is water. Therefore the surface tension of water (~0.072N/m) instead of THF surface tension (0.264N/m [Mellan, 1977]) is used later to obtain pore size distribution from water retention curves.

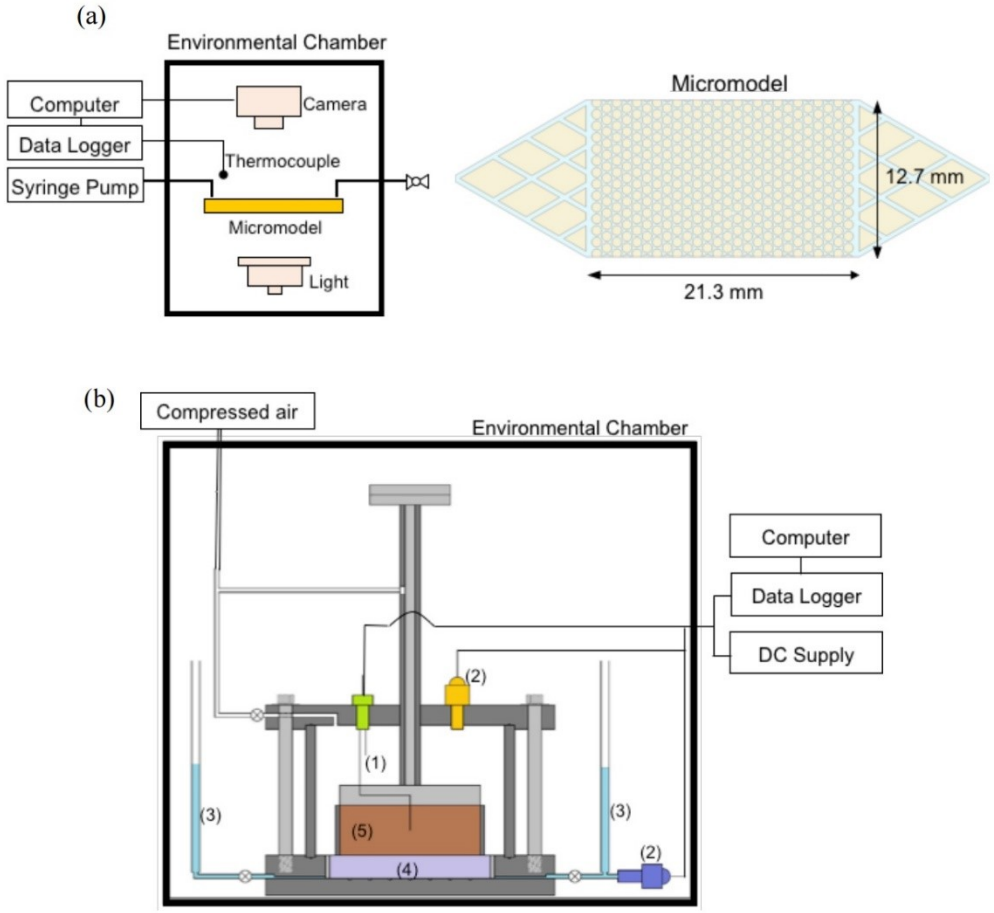

Figure 4.2 Experimental configuration. (a) Micromodel for the observation of THF hydrate pore habit. The dimension of pore space area is 12.7mm×21.3mm, and the pore depth (internal thickness) of the micromodel is 50μm. The diameter of mono-sized grain is 800μm, and the distance between grains is 105μm. (b) Pressure chamber for water retention curve measurement. The chamber consists of (1) thermocouples, (2) pressure transducer, (3) water column, (4) ceramic porous plate, and (5) sediment sample.

4.3 Results and Analyses

Images of THF hydrates in the micromodel are shown in Figure 4.3. Initially, the pore space in the micromodel is saturated with water-THF solution prior to hydrate formation (Figure 4.3a). The nucleation starts 68 hours after the temperature decreases to -8°C. At this moment, it is not sure whether the nucleated crystal is hydrate or ice. After 6 hours, the temperature of the micromodel increases to 1°C to dissolve any possible ice that

might be formed while maintaining hydrate crystals (Figure 4.3b). At this stage, many small hydrate crystals are disseminated all over the pore space. The picture taken another 6 hours later shows that hydrate crystals are merged to each other (Figure 4.3c). As times goes by, hydrate particles in the pore space of the micromodel keep merging to each other and forming bigger hydrate particles until 72hours from the nucleation (Figure 4.3d~4.3h). This Ostwald ripening phenomenon was also observed in previous study [Tohidi et al., 2001]. THF hydrates in the micromodel are monitored for additional 6 days, but the change in hydrate pore habit is not observed since 72 hours from the nucleation.

As shown in the series of pictures in Figure 4.3, THF hydrates are not wetting phase in water-THF hydrate-quartz surface system. Even, a thin layer of water is observed between THF hydrate and the quartz surface of the micromodel. The non-wetting hydrate formation in pore space is also observed in other laboratory experiments for Xenon hydrate [Chaouachi et al., 2015], methane hydrate [P B Kerkar et al., 2014], and THF hydrate [P Kerkar et al., 2009; Tohidi et al., 2001; Xue et al., 2012]. The measured contact angle is 105~140° for methane hydrate in glass bead packing [P B Kerkar et al., 2014] and 140° for THF hydrate in glass bead packing [P Kerkar et al., 2009]. In addition, the formation of a thin water layer between hydrates and pore surface is also reported in other studies [Chaouachi et al., 2015; P B Kerkar et al., 2014; Tohidi et al., 2001].

Compressional and shear wave velocity measurement of THF hydrate-bearing sediments under water-saturated condition confirms that hydrate nucleation starts at pore space, and hydrates grow following pore-filling model as long as hydrate saturation S_h is lower than ~40% [Waite et al., 2009; Yun et al., 2005]. This non-cementing behavior is

also found in methane hydrate-bearing sediments under water-saturated condition [Choi et al., 2014; Yokoyama et al., 2011].

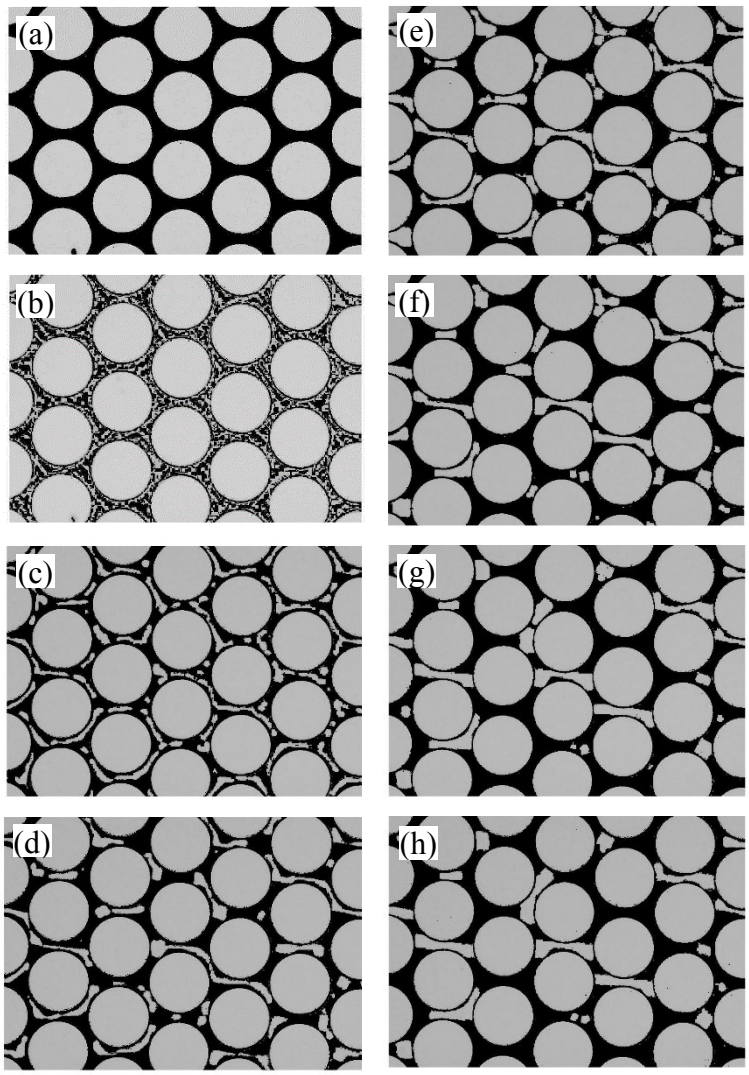

Figure 4.3 THF hydrates formation in the micromodel. (a) Micromodel saturated with water and THF solution prior to hydrate formation. (b) Nucleated THF hydrates right after temperature increased from -8°C to 1°C (time=0h). (c) Hydrates merges to each other at the time=6h. Hydrate particles keep merging to each other forming bigger particles as time goes by. Pictures are taken at the time 12h (d), 18h (e), 24h (f), 48h (g), and 72h (h) after the nucleation (time=0h).

As shown in Figure 4.3, THF hydrates tend to occupy an entire space of one pore. Sometimes hydrate particles occupy one pore as well as part of a neighboring pore. In addition, there are small hydrate particles occupying only part of pore space in the micromodel, which reduces the size of pores. Even though this is the observation from two-dimensional micromodel experiment, it is expected that hydrate formation in pore space affects pore size distribution of in-situ sediment by not only plugging pores but also producing pores with smaller size. This effect will be discussed later with water retention curve measurement data.

The water retention curves measured for several THF hydrate saturation conditions S_h=0, 0.4, 0.6, 0.7 are shown as symbols in Figure 4.4a. The measurement of water retention curve for the hydrate saturation S_h=0.8 case was tried. But, there was no water drainage even at the capillary pressure P_c=60kPa, which means there is no available water percolation path due to hydrate clogging in pore space. Water saturation S_w is the fraction of void volume V_v occupied by water volume V_w, $S_w=V_w/V_v$ where void volume V_v includes volumes of water, gas, and hydrate $V_v=V_w+V_g+V_h$ ($1=S_w+S_g+S_h$ after each term is divided by V_v). The water retention curve of S_h=0 case starts at S_w=1. And water retention curves for S_h=0.4, 0.6, and 0.7 cases start at S_w=0.6, 0.4, and 0.3, respectively. In the inset figure of Figure 4.4a, the definition of effective water saturation $S_w^*=V_w/(V_v-V_h)=S_w/(1-S_h)$ is used to plot the same data used in Figure 4.4a. Therefore, all water retention curves start at S_w=1.

The water retention curve results show that the gas-entry pressure and the capillary pressure at given effective water saturation S_w^* increase as the THF hydrate saturation increases. Higher initial hydrate saturation condition results in higher effective residual

water saturation S_{rw}*. This trend is also observed in the numerical simulation using a pore-network model [Dai and Santamarina, 2013]. But residual water saturation S_{rw} remains almost constant at S_{rw}=0.07 for hydrate-bearing sediments.

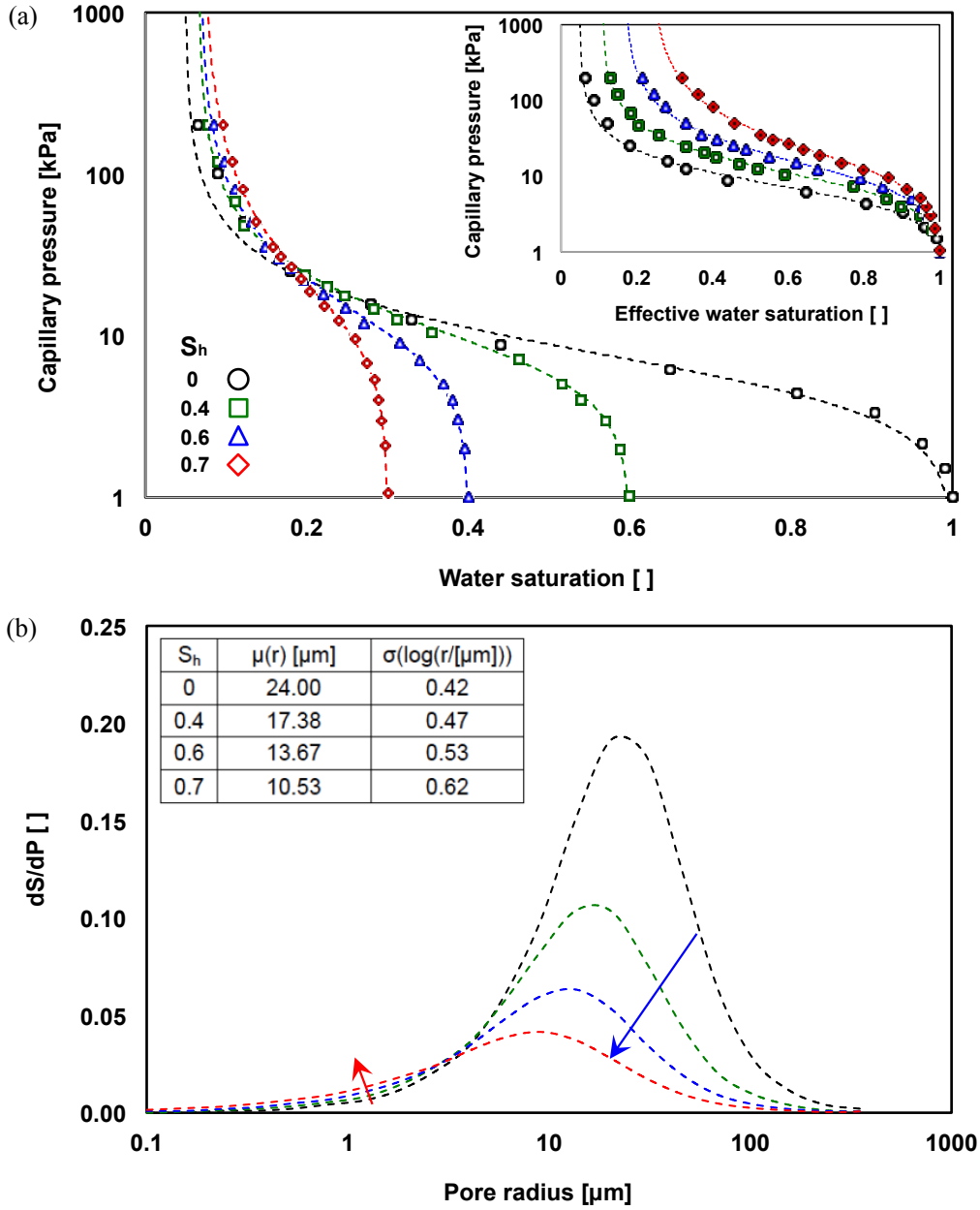

Figure 4.4 Water retention curves and pore size distribution for hydrate saturation S_h=0, 0.4, 0.6 and 0.7 cases. (a) Water retention curves. Experimental results are shown as symbols, and van Genuchten Equation 1 fitted to the experimental results are shown as broken lines. Fitting parameters are shown in the inset table. (b) Pore size distribution obtained from water retention curves.

The logarithmic-least square method is employed to fit the Equation 1 to the measured water retention curve data. Obtained fitting curves (lines) are superimposed on the experimental results (symbols) in Figure 4.4a. Pore size distribution PSD curves are obtained from the water retention curves (Figure 4.4b). The average pore size μ(r) and standard deviation of pore size distribution in log-scale σ(log(r/[μm])) for each PSD curve is also shown in the inset table of Figure 4b. As more hydrates form in pore spaces, large pores are occupied by hydrates (pointed by blue arrow in Figure 4.4b) and the peak of PSD curves move to the left, which means the reduction in the average pore size. And pores with smaller size are produced in case hydrates partially occupy pore space (pointed by red arrow). Therefore, as hydrate saturation increases, the average pore size decreases but the distribution of pore size becomes wider, which means the increase of capillary pressure and the decrease in fitting parameter m-value of Equation 1.

The fitting parameter m-value and gas-entry pressure P_0 obtained for each THF hydrate saturation condition are shown in Figure 4.5a. The m-value decreases with increasing hydrate saturation: the obtained m-values are m=0.58, 0.55, 0.51 and 0.46 for hydrate saturation S_h=0, 0.4, 0.6 and 0.7, respectively. As the THF hydrate saturation increases, the gas entry pressure increases from P_0=5.9kPa for S_h=0 to P_0=13.0kPa for S_h=0.7.

The m-values used for gas hydrate numerical simulation studies in the literature range from m=0.45 to m=0.77 for hydrate saturation S_h=0.1~0.7 and the gas entry pressure ranges from 2kPa to 100kPa [Gamwo and Liu, 2010; G Moridis, J and Reagan, 2007; George Moridis, J and Sloan, 2007; M. T. Reagan et al., 2010; Matthew T. Reagan and Moridis, 2008; Rutqvist and Moridis, 2007]. The detailed summary about various fitting

parameters is available in Jang and Santamarina [2014]. The fitting parameter m-values used for the simulation studies in the literature are in good agreement with the values measured in this study. And the gas entry pressure P_0 should be dependent of sediment type (e.g., sand, silt) and effective stress level of in-situ sediment. Moreover, from the results, it is noted that the fitting parameter m-value and gas-entry pressure P_0 should be updated while hydrates dissociate in the sediment.

(a)

S_h	P_0 [kPa]	S_{rw} (S_{rw}*)	m
0	5.9	0.05	0.58
0.4	8.1	0.07 (0.11)	0.55
0.6	10.2	0.07 (0.17)	0.51
0.7	13.0	0.07 (0.24)	0.46

(b)

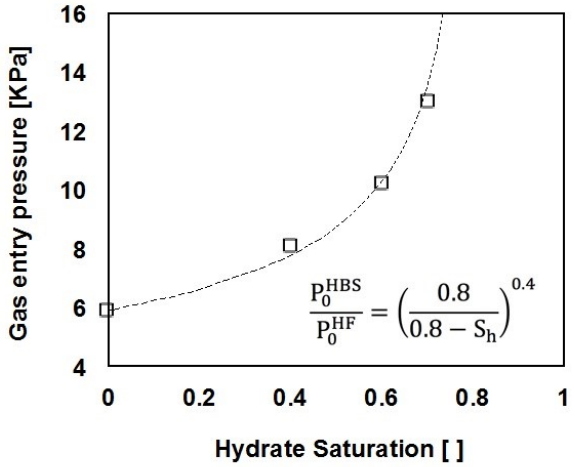

(c)

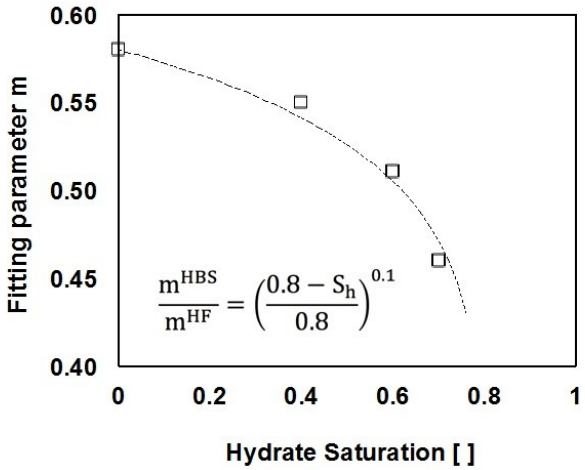

Figure 4.5 Fitting parameters of van Genuchten equation. (a) Fitting parameters obtained from experimental results. (b) General form of gas entry pressure P_0. (c) General form of fitting parameter m-value.

Based on the obtained fitting parameters m-value and the gas-entry pressure, the following power equations are suggested as shown in Figure 4.5b&c.

$$\frac{P_0^{HBS}}{P_0^{HF}} = \left(\frac{0.8}{0.8\text{-}S_h}\right)^{0.4} \qquad for\ \ S_h < 0.8 \tag{4.4}$$

$$\frac{m^{HBS}}{m^{HF}} = \left(\frac{0.8\text{-}S_h}{0.8}\right)^{0.1} \qquad for\ \ S_h < 0.8 \qquad (4.5)$$

Where P_0^{HBS} and P_0^{HF} are the gas-entry pressure for hydrate-bearing sediment and hydrate-free sediment, respectively. Likewise, m^{HBS} and m^{HF} are fitting parameter for hydrate-bearing sediment and hydrate-free sediment, respectively. These power equations are limited for the hydrate saturation less than S_h=0.8 because gas invasion is not available for S_h=0.8 case (No water drainage path available due to hydrate clogging in pore space).

4.4 Conclusions

The characteristic behavior of unsaturated sediment is well captured by the water retention curve. A study to experimentally obtain fitting parameters of the water retention curves is performed. First, the formation of THF hydrates in the micromodel confirms that THF hydrates are not wetting phase on quartz surface and shows that hydrate occupy either an entire pore or part of pore space forming smaller pore. And, the experimental measurements for water retention curves in THF hydrate-bearing sediments are presented: the gas entry pressure and capillary pressure at a given effective water saturation in THF hydrate-bearing sediments increases with increasing hydrate saturation. Based on the experimental results, fitting parameters of van Genuchten equation are suggested: the m-value related to the shape of water retention curve decreases with increasing hydrate saturation, which means wider pore size distribution. The fitting parameter m-values suggested in this study are in good agreement with the values used for other hydrate numerical simulation studies. In addition, it is noted that the fitting parameters dependent

on hydrate saturation should be updated during hydrate dissociation in numerical simulation.

CHAPTER 5

IMMISCIBLE MULTIPHASE FLUID FLOW THROUGH POROUS MEDIA: DIMENSSIONLESS NUMBERS AND PHASE DIAGRAM

5.1 Introduction

Multiphase fluid flow in porous media is found in various applications such as oil and gas recovery, hydrology, geological CO_2 sequestration, and soil remediation. The formation of preferential flow channels by invading fluid is a critical constraint in above processes. The two-phase displacement where a non-wetting fluid displaces a wetting fluid depends on several factors such as viscosity, interfacial tension, injection rate, wettability and characteristics of the porous media. A clear perspective of the structure and formation of the preferential pathways and its dependency on different parameters remains a challenge.

Lenormand et al. [1988] conducted a comprehensive study through pore network model simulations and micromodel experiments. They show three fluid displacement patterns: viscous fingering, capillary fingering and stable displacement regimes plotted on a *log M – log C* phase diagram. Here, *M* defines the viscosity ratio (ratio of the invading fluid viscosity μ_2 to the defending fluid viscosity μ_1) and *C* is the capillary number (the ratio of the viscos force to the capillary force).

$$M = \frac{\mu_2}{\mu_1} \tag{5.1}$$

$$C = \frac{q\mu}{\sum \gamma \cos\theta} \tag{5.2}$$

Where q is the displacing fluid flow (m^3/s), μ is the maximum viscosity of the two fluids, Σ (m^2) is the cross sectional area of the inlet and γ (N/m) is the interfacial tension between two fluids.

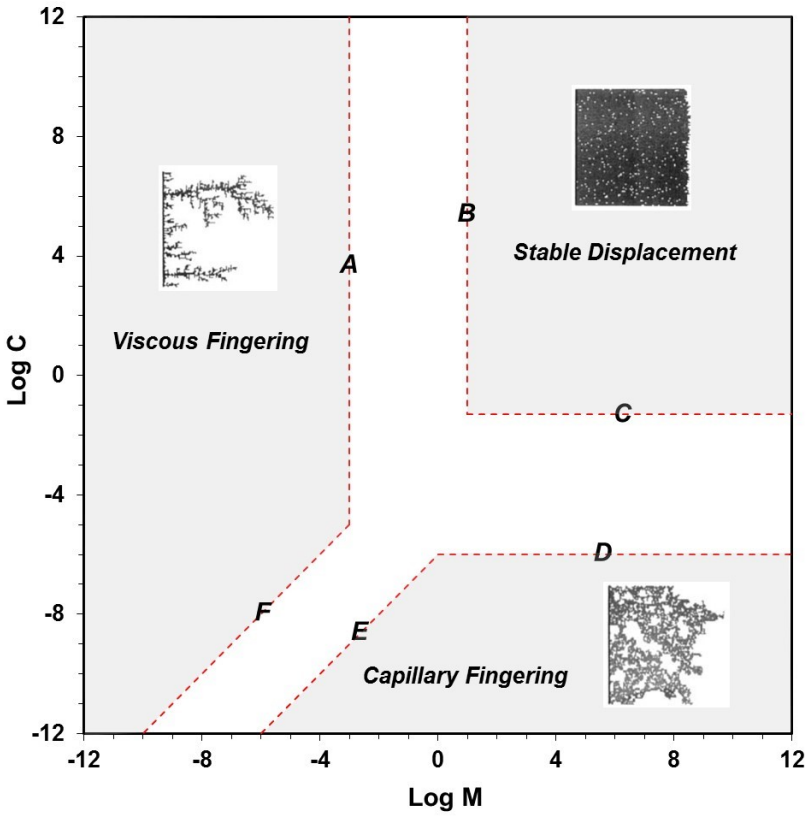

Figure 5.1 Displacement patterns proposed by [Lenormand et al., 1988]. The experimental and numerical results represent typical regimes of viscous fingering, capillary fingering and stable displacement.

Figure 5.1 shows the phase diagram and the typical patterns of the three domains proposed by Lenormand et al. [1988]. The physical interpretation of the three different regimes was explained as follow:

(1) Viscous fingering: the principal force is due to the viscosity of the displaced fluid and capillary effect in the displacing fluid is negligible. The pattern includes spread tree-like fingers with no loops. In this case, the final saturation is low.

(2) Capillary fingering: this occurs at low capillary numbers where viscous forces are negligible in both fluids and the principal force is due to capillarity. The pattern includes fingers growing in all directions with some loops which trap clusters of displaced fluid. The final saturation in this case is higher than the viscous fingering and lower than the stable displacement condition.

(3) Stable displacement: this takes place at high capillary numbers and viscosity ratios where the principal force is due to the viscosity of the invaded fluid. The pattern has a flat front shape with a small number of irregularities and only a few trapped clusters of the displaced fluid. The final saturation is higher than viscous and capillary fingering and close to a fully saturated condition.

The boundary of each of these three domains was derived based on the force balance relationship between the capillary and viscos forces (Figure 5.1, lines A-F) [Lenormand et al., 1988]:

- *Lines A and B:* These boundaries are derived based on the value of viscosity ratio M at high capillary numbers and the viscous pressure drop δP:

$$\delta P = \frac{\mu\, qL}{k k_r \Sigma} \tag{5.3}$$

where k is the monophasic permeability and k_r is the relative permeability of the fluid. At very large M, the dominant force is the viscous force of the invading fluid and the viscos pressure drop within the displaced fluid is negligible (Line B). At low M, the viscous pressure drop in the invading fluid is negligible (Line A).

- *Lines D and C:* At low capillary numbers *C*, viscous force is very small in comparison with capillary forces:

$$\frac{\mu\, qL}{kk_r\Sigma} << \frac{\gamma\cos\theta}{r} \tag{5.4}$$

At high *M* values, viscous forces are dominant in the injected fluid $\mu=\mu_2$. This leads to the boundary of line D where $C=constant\times k.k_r/rL$. Different capillary numbers leads to a different *constant* value which defines line C.

- Lines E and F: At high *M* values, viscous forces are dominant in the displaced fluid. Therefore, inserting $\mu=\mu_1$ leads to the boundary of Line E with a form of $C=constant\times M\times k.k_r/r$ which has a 45 degree slope (Slope=1) in the *log C-log M* scale map. A different *constant* value leads to Line F which is parallel to line E. The continuity is assumed for the intersected lines B-C, D-E and A-F.

A recent experimental study [Zhang et al., 2011] confirmed the three displacement domains and their boundaries. They conducted a series of displacement experiments using a homogenous water-wet micromodel for different pairs of wetting- non-wetting fluids with viscosity ratio M ranging from *log* =-1.95 to 1.88 and capillary number *C* ranging from *logC*=-5.88 to -1.02. Although their results confirmed the numerical results obtained by [Lenormand et al., 1988], they modified the boundaries of displacement patterns. A more recent study [Liu et al., 2013] used Lattice Boltzmann method to simulate immiscible fluid flow in a homogenous pore network model. Figure 5.2 illustrates the obtained displacement regimes and their boundaries proposed by Lenormand et al. [1988], Zhang et al. [2011] and Liu et al. [2013]. It was discussed that the discrepancy between the

boundaries is due to the variation in the size and configuration (pore size distribution and manufacturing) of the pore networks.

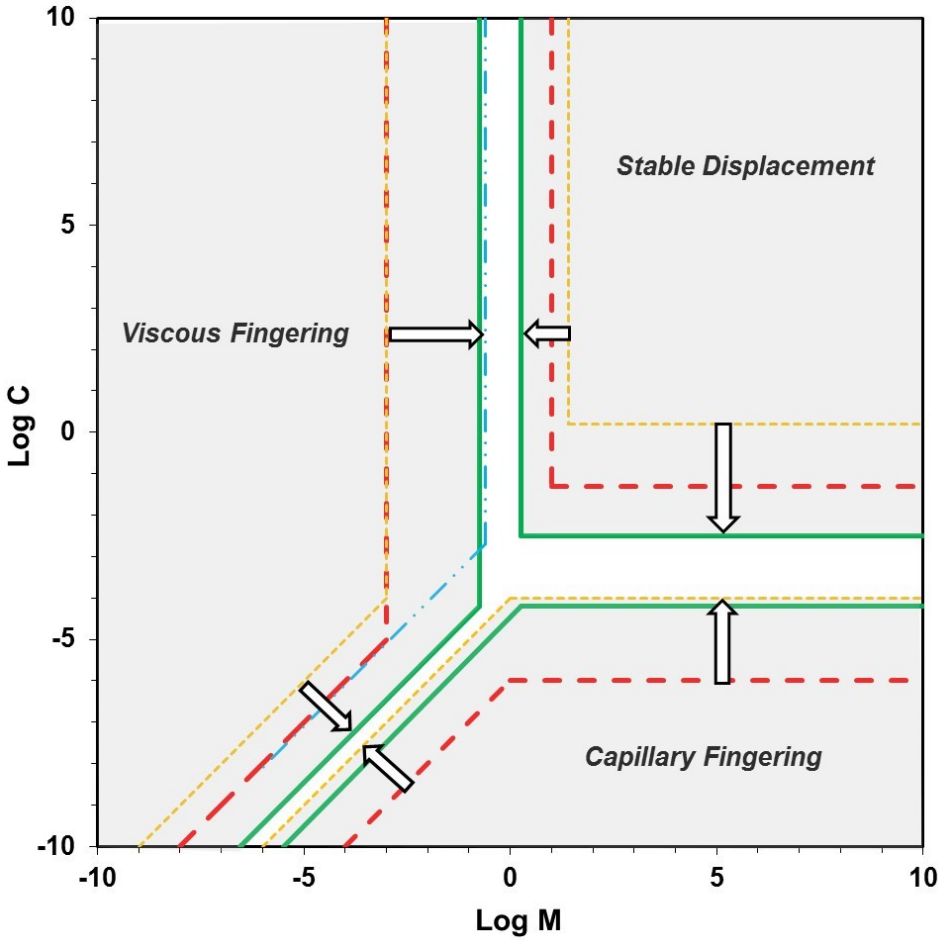

Figure 5.2 Phase diagram boundaries suggested by Lenormand et al. [1988](experimental study by red dashed and 2D pore network simulation by yellow small dashed), Zhang et al. [2011] (experimental study by green solid line) and Liu et al. [2013] (2D Lattice Boltzmann simulation by blue dash dot-dotted lines).

Figure 5.3 shows the range of capillary numbers and viscosity ratios used in different studies as well as this study. As shown in Figure 5.3 the range of the data is limited compare to the proposed zones of the phase diagram because of difficulties in experiments (e.g., limited range of viscosity ratios for different fluid types) and numerical simulations (e.g., convergence problem in LBM especially for high and low viscosity ratio region).

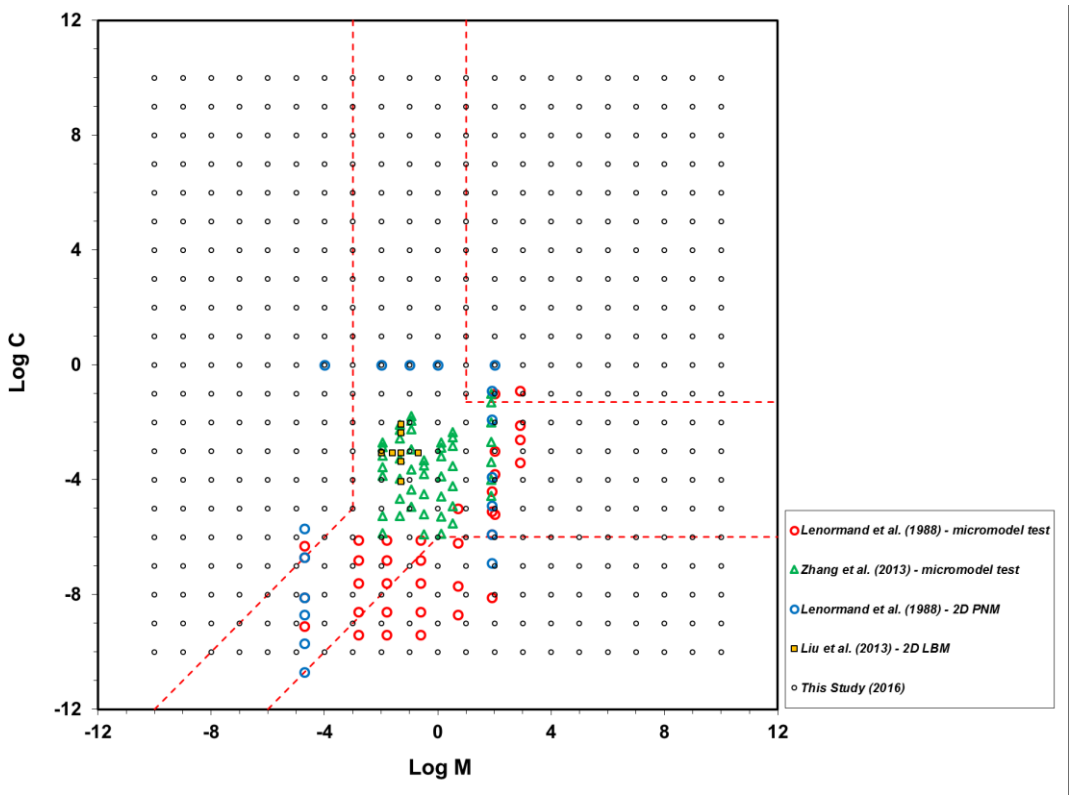

Figure 5.3 Range of the selected pairs of Log C and Log M used in Lenormand et al. [1988], Zhang et al. [2011], Liu et al. [2013] and the present study [2016]. The red dotted-lines shows the phase diagram proposed by Lenormand et al. [1988].

This study employs a time-dependent two-phase flow simulation using a three-dimensional pore network model for the first time to explore the displacement patterns for a wide range of capillary numbers and viscosity ratios. The mechanisms of the three regimes are investigated particularly for the dimensionless numbers that was not covered in the previous studies (Figure 5.3). Moreover, all the recent numerical simulations use artificial two-dimensional pore network models that would not represent the heterogeneity of the pore space. In order to deal with this problem, we use a 3D pore network model extracted from micro-CT images of a sandy sediment to simulate the immiscible fluid flow through the porous medium. Moreover, the effect of pore size distribution and connectivity on the preferential channel and fluid displacement patterns is explored. The questions such

as dependency of phase diagram on pore size distribution, the evolution of the patterns, formation of trapped clusters and final saturation of the medium is answered in this study.

5.2 Numerical Method and Procedure

A 3D pore network model is used to simulate the immiscible multiphase fluid flow in the porous medium for a wide range of capillary numbers *Log*C and viscosity ratios *LogM*. The numerical results are compared to the phase diagram proposed by previous studies.

5.2.1 Pore-Network Model

The same sample shown in Chapter 3 is used to extract the pore network model. However the confining pressure subjected to the sample used in Chapter 3 is 9MPa while we used 0MPa in this study. The volume of the CT images used in this study is $8mm^3$ (2mm×2mm×2mm) with 12.5μm pixel resolution. The obtained pore network model consists 1425 pores and 5775 tubes with a mean tube connectivity per pore (coordination number) of cn=7.8. Mean pore radius is $\mu[R_{pore}]$=67μm, and mean tube size is $\mu[R_{tube}]$=12μm. The effect of pore size on the boundary of phase diagram is analyzed using three different tube size distribution cases which are the original pore network model extracted from the CT images and the two other cases that numerically generated by changing only the tube size distribution of the network (size of balls, coordination number, location of pores and length of tubes maintained without any change). Figure 5.4 shows the three tube size distribution cases used in this study. The average value of tube size distribution is maintained constant while the standard deviation of tubes size distribution is changed.

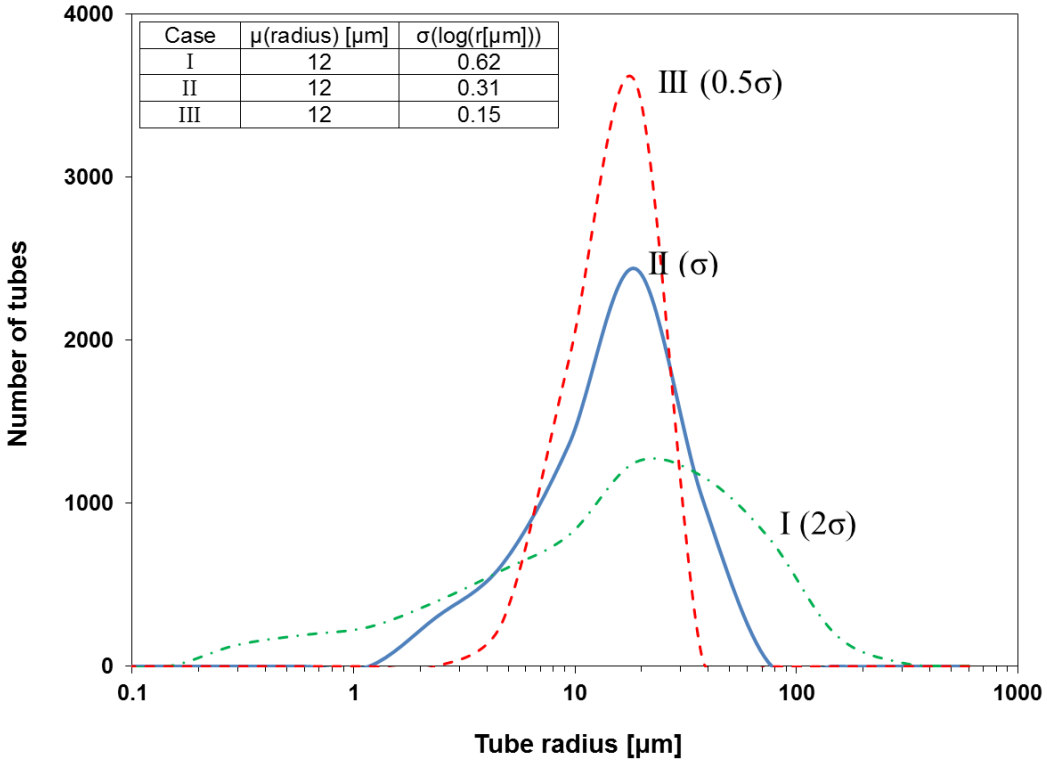

Figure 5.4 Different tube size distribution used in this study.

5.2.2 Two-Phase Fluid Flow Simulation

We follow the algorithm explained in Aker et al. [1988] to simulate two-phase immiscible fluid flow in the pore network model. Using this algorithm we are able to model the dynamics of the temporal evolution of the fluid flow and the time dependency of the interface between the wetting and non-wetting fluids.

To follow this algorithm, initially the pore network model is fully saturated by the defending fluid with viscosity μ_1, and the invading fluid with viscosity μ_2 is injected from the left boundary (inlet boundary) with a constant injection rate. All the boundaries are closed except the left (inlet) and right boundary (outlet).

It is assumed that the fluids are immiscible so that there is an explicit interface between the defending and invading fluids. Consider a cylindrical tube containing both fluids between node *i* and *j* in the pore network model. The capillary pressure P_c at the interface between the two phases is given by Young-Laplace equation:

$$P_c = \frac{2\gamma}{r}\cos\theta \tag{5.5}$$

Aker et al. [1988] modified the Young-Laplace equation in order to take the position of the meniscus into account for the calculation of the capillary pressure inside the tubes. They assumed that the tubes are hourglass-shaped with an effective radii following a smooth function. As a result the capillary pressure is a function of meniscus position inside the tube:

$$P_c = \frac{2\gamma}{r}\left[1-\cos(2\pi x)\right] \tag{5.6}$$

Where x is the relative position of the meniscus which is a continuous function ranging from 0 to 1 (0 for the beginning of the tube, and 1 for the end of the tube). It is assumed that the contact angle θ=0 (perfect wetting condition).

The volume flux *q* through a cylindrical tube is calculated from the Washburn equation:

$$q = \frac{-\pi r^4}{8\mu' d}\left(\Delta P - P_c\right) \tag{5.7}$$

$$\mu' = \mu_2 x + \mu_1 (1-x) \tag{5.8}$$

Where μ' is the effective viscosity due to the viscosity of the fluids. ΔP is the pressure difference in a capillary tube.

Solving the Flow Field for a Constant Flow rate

By the conservation of volume flux for incompressible fluids at each node we have:

$$\sum q_{ij} = 0 \tag{5.9}$$

By inserting Equation 5.7 in 5.9 and solve it using the conjugate gradient method, we can obtain the pressure at all nodes of the network. As a result, the pressure difference across the network can be measured. In this study, the main purpose is to explore the dynamics (pressure gradients) at a constant flow rate. Therefore, we need to find the nodal pressures at a constant injection rates. For a given flow rate Q in the pore network:

$$Q = A.\Delta P + B \tag{5.10}$$

Where A and B are parameters depending on the properties of the fluid and the geometry of the porous medium. These parameters can be calculated by solving the nodal pressures for two differential pressures ΔP_1 and ΔP_2. After finding A and B, ΔP is calculated for the desired constant flow rate.

Time Step and updating the Meniscus Position

The time step Δt is selected such that only one meniscus can cross a node at each time step. This leads to the Equation (5.11):

$$\Delta t = \min_{ij}\left[\frac{\Delta x_{\max}}{V_{ij}}\right] \tag{5.11}$$

Where V_{ij} is the flow velocity between two nodes and can be calculated using the flow rate and the radius of the tube ($V=Q/\pi r^2$). In each time step it is checked whether a meniscus crosses a node or not and if this happens, a new time step is defined using Equation (5.11). As a result, the new position of the meniscus is calculated and updated using the second order of Runge-Kutta scheme.

5.3 Results and Discussion

A large series of simulations consists 441 runs (21 viscosity ratios × 21 capillary numbers) for each of the three tube size distribution cases (totally 21×21×3=1323 simulations) are performed to simulate two-phase displacement in the pore network model for a wide range of capillary numbers from *Log C* = -10 to 10 and viscosity ratios from *logM*=-10 to 10. Table 5.1 compares the range of the dimensionless numbers and methods used in the previous studies and this effort.

Figure 5.5 shows several simulations for different pairs of capillary number of viscosity ratio for tube size distribution case 2 (standard deviation =1σ). The simulation results clearly show the evolution of the phases from the viscous fingering to capillary fingering and stable displacement. At low viscosity ratio (*Log M*= -5) where the principal force comes from the viscosity of the displaced fluid, the displacement pattern has a tree-like shape and the final saturation of the invading fluid is very low. In this case (*Log M*=-5) the saturation slightly increases from 0.17 to 0.2 as the capillary number decreases (*LogC* decreases from 5 to -5).

Table 5-1 Comparison between the number of simulations and range of the dimensionless numbers used in the published studies and this study.

References	Method	Number of simulations	Range of capillary number *Log C*	Range of viscosity ratio *Log M*
Lenormand et al. [1988]	Experimental, Micromodel	35	-9.4 ~ -0.9	-4.7 ~ 2.9
	Numerical, 2D Pore network model	17	-10.7 ~ 0	-4.7 ~ 2
Zhang et al. [2011]	Experimental, Micromodel	48	-5.91 ~ -1	-1.95 ~ 1.88
This Study (2016)	Numerical, 3D Pore network model	441*	-10 ~ 10	-10 ~10

* 441 simulation runs for each tube size distribution case (totally 441×3=1323 simulations)

At low capillary number (*Log C*=-5) we observe that the displacement pattern changes from the viscous fingering to capillary fingering within the range of viscosity ratio from -5 to 5. The change of displacement pattern from capillary fingering to stable displacement is also shown in Figure 5.5, when the viscosity ratio is high (*Log M*=5) and the capillary number increases from -5 to 5. The final saturation for the stable displacement condition is about 0.7 for this case.

The simulation results obtained from a large number of runs are shown in contour plot. Figure 5.6 shows the contour plot of saturation (left column) and front width ratio (right column) in terms of *LogC* and *LogM* for the three cases of tube size distributions (Figure 5.6a for case 1 [2σ], figure 5.6b for case 2 [σ] and figure 5.6c for case 3 [0.5σ]). Here, the front width ratio is defined as the average width of the interface boundary (interface between the invading and defending fluid) divided by the total width of the pore network model (2mm). The results shows that the boundaries of phases are formed at same locations for both saturation and front width ratio plots. The simulation results for different tube size distributions show that the distance between the boundaries of the stable displacement and viscous fingering decreases as the tube size distribution of the network is more uniform:

$$d_{viscous\text{-}stable\ [0.5\sigma]} < d_{viscous\text{-}stable\ [\sigma]} < d_{viscous\text{-}stable\ [2\sigma]}$$

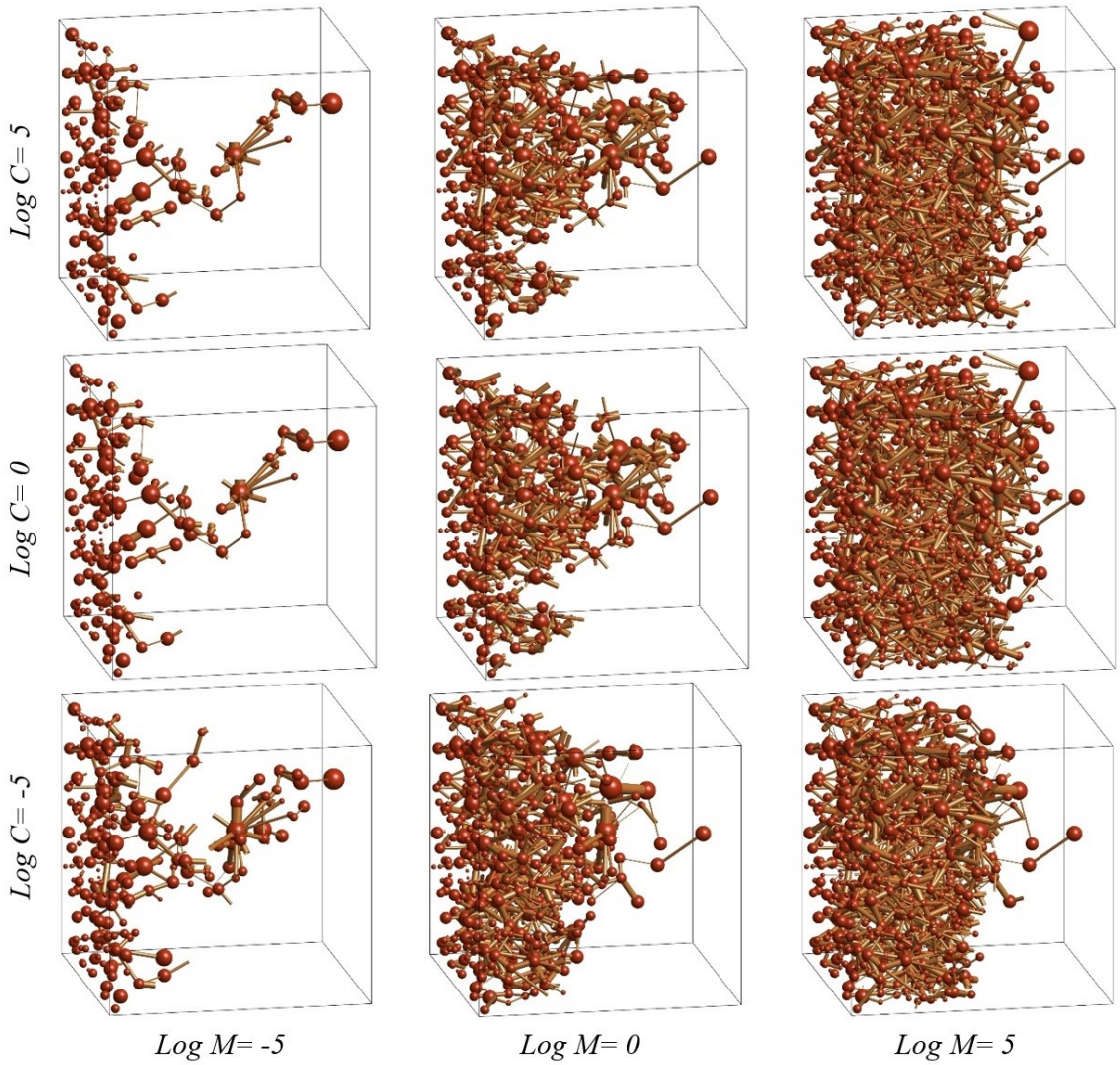

Figure 5.5 Selected simulations for different pairs of *Log M* and *Log C* numbers for tube size distribution case 1 (standard deviation = 1σ). The fluid flow direction is from the left to the right boundary.

The saturation and the front width ratio increases as the standard deviation (σ) of the tube size distribution decreases. The final saturation is 0.78 for case 3 (0.5σ) and 0.74 for case 1 (2σ). Furthermore, the lower boundary of viscous fingering (1:1 sloped line) shifts to lower capillary numbers as the tube size distribution spreads.

It is also valuable to study the displacement regimes in terms of the number and volume of the trapped clusters of the defending fluid in the porous media. The numbers and average volume of trapped clusters is calculated for the three tube size distribution cases and plotted as a contour diagram (Figure 5.7). This figure shows that the boundary of the phases can be distinguished based on the information of the trapped clusters. The maximum numbers of trapped clusters is obtained in the transition zone between the viscous fingering and stable displacement while the average volume of trapped clusters is higher in the transition zone of capillary fingering and viscous fingerings. This explains that the size of trapped clusters is smaller for viscous-stable transition zone which is in agreement with the previous observation published in the literature. The more interesting finding is that the capillary fingering zone cannot be clearly distinguished using the saturation or front width values, while the number of trapped clusters can show the boundary of the capillary fingering zone (Figure5.7a and Figure 5.7b for number of trapped clusters). The evolution of final saturation of the invading fluid through the different phases is shown in Figure 5.8~Figure 5.11. At high viscosity ratio *Log M*=5, the saturation increases from 0.55 to 0.73 as the *log C* increases for size distribution case 1 (transition from capillary fingering to stable displacement). The transition between the capillary fingering and stable displacement is clearer for the wider tube size distribution case (case 1 rather than case 2 or 3). This shows that the uniform size pore networks would not represent the real nature of the evolution of different pattern regimes.

The right side boundary of the viscous fingering shifts to a lower *Log M* value as the tube size distribution increases (Figure 5.9).

Figures 5.10 and 5.11 also explains how the boundaries of the viscous fingering, capillary fingering and stable displacement changes as the function of the tube size distribution.

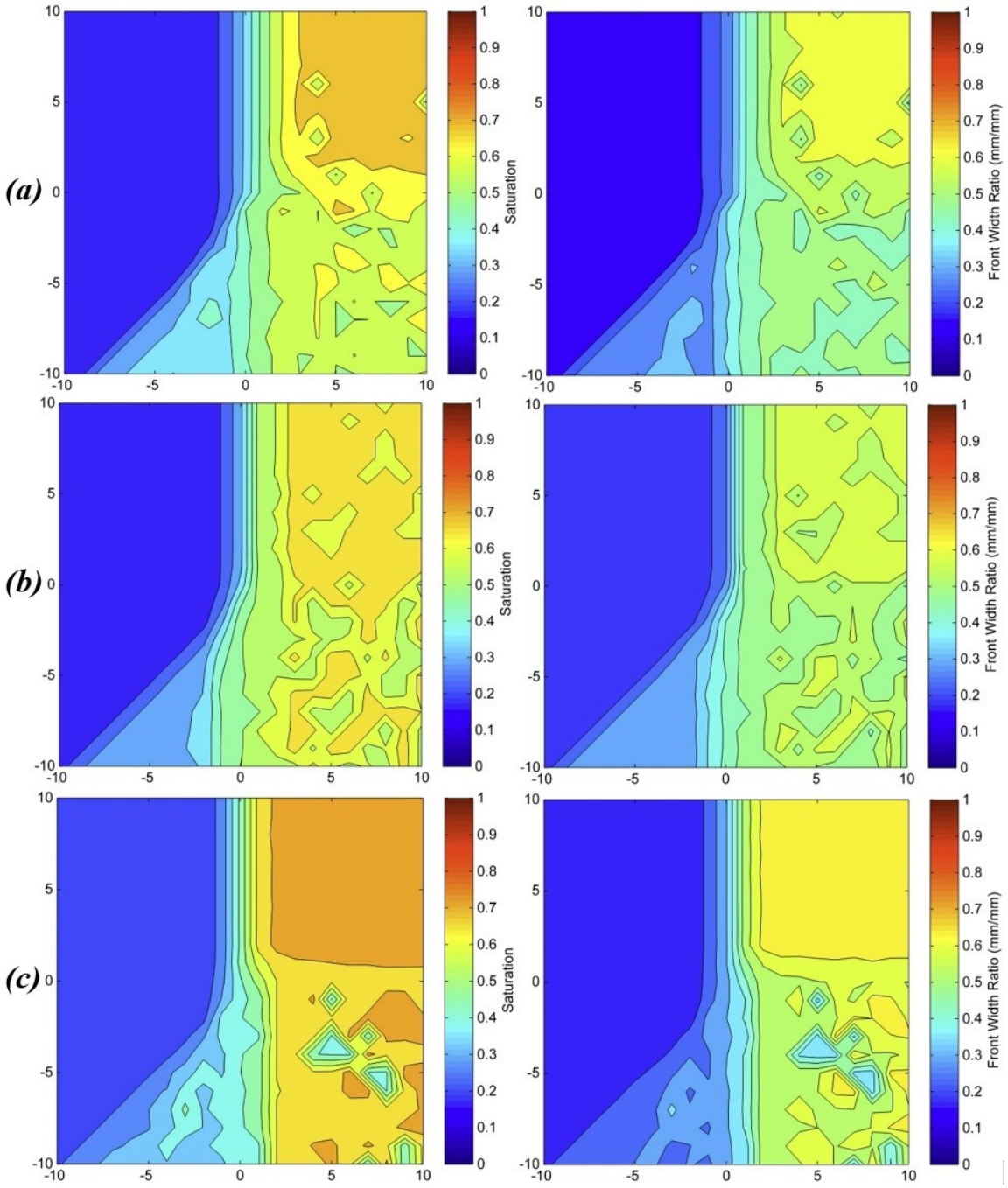

Figure 5.6 Contour of saturation (left column) and front width ratio (right column) in *LogC-LogM* map for different tube size distribution cases. (a) Case 1 [2σ]. (b) Case 2 [1σ]. (c) Case 3[0.5σ].

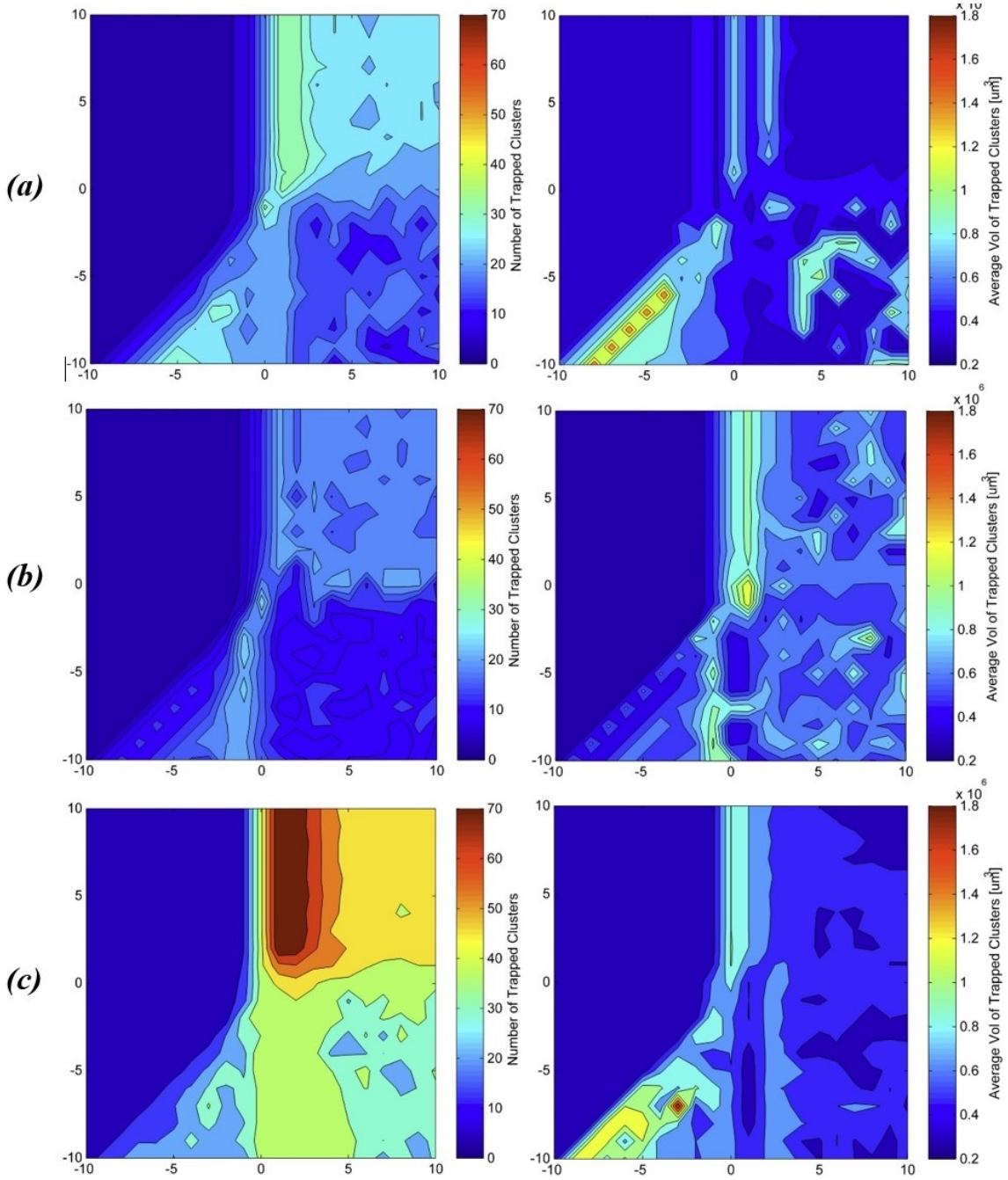

Figure 5.7 Contour of number of trapped clusters (left column) and the average volume of trapped clusters (right column) in *LogC-LogM* map for different tube size distribution cases. (a) Case 1 [2σ]. (b) Case 2 [1σ]. (c) Case 3[0.5σ].

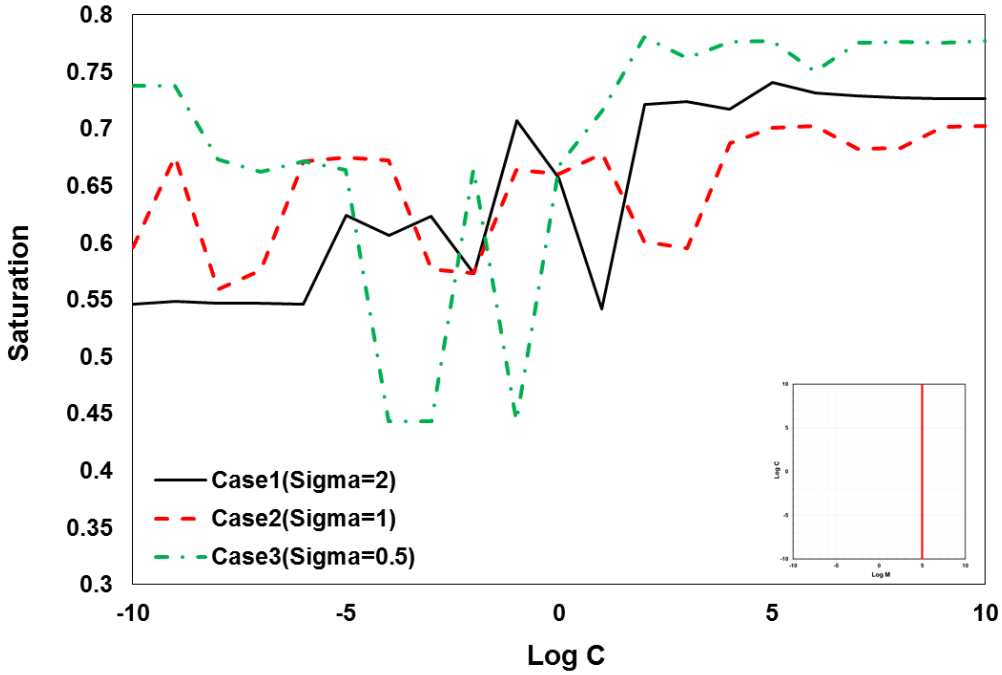

Figure 5.8 Saturation-*Log C* for different tube size distribution cases (*Log M*=5). This figures illustrates the transition from the capillary fingering to stable displacement.

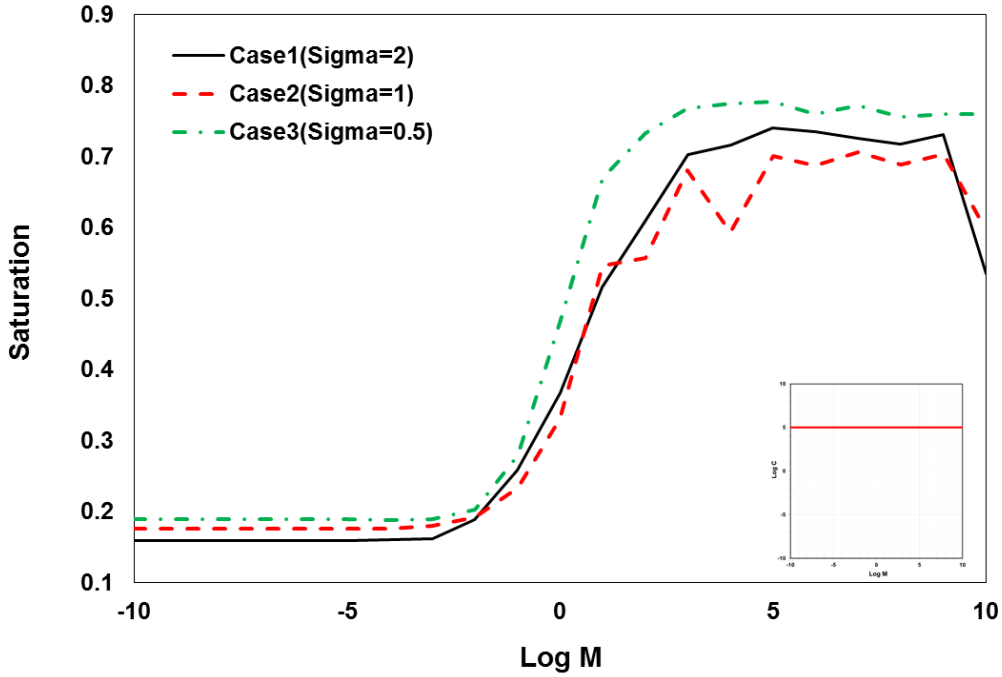

Figure 5.9 Saturation-*Log M* for different tube size distribution cases (*Log C*=5). This figure illustrates the transition from viscous fingering to stable displacement.

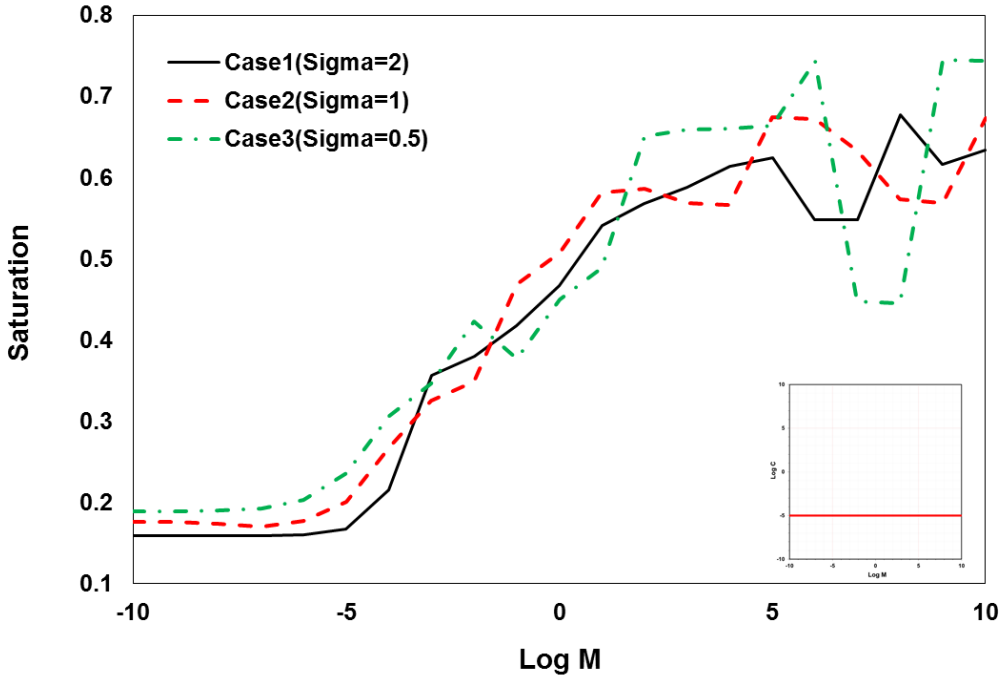

Figure 5.10 Saturation-*Log M* for different tube size distribution cases (*Log C*=-5). This figures illustrates the transition from the viscous fingering to capillary fingering.

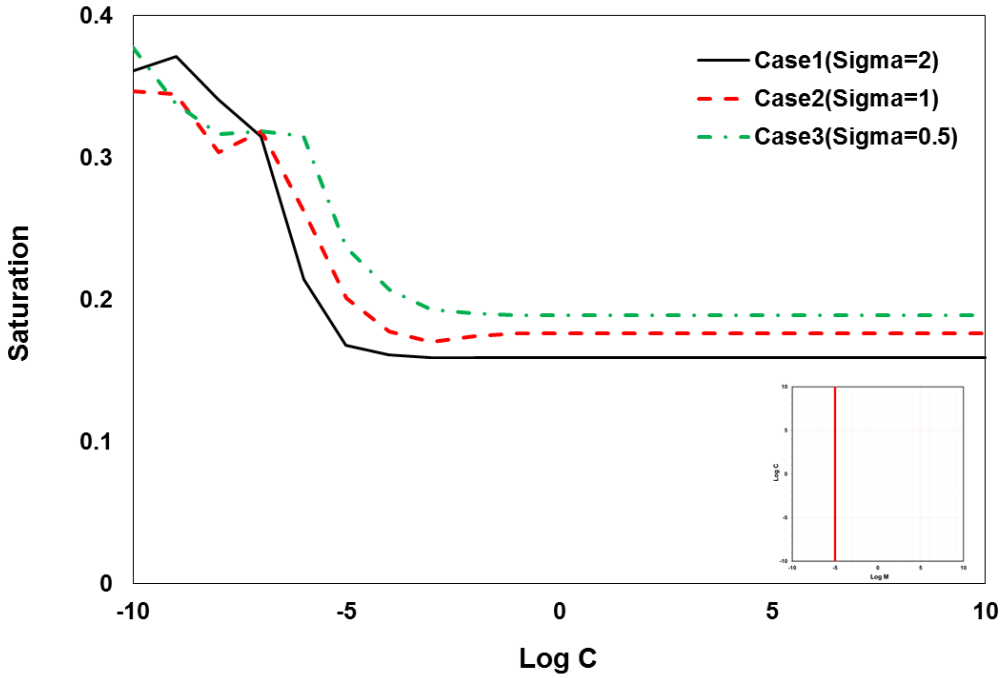

Figure 5.11 Saturation-*Log C* for different tube size distribution cases (*Log M*=-5). This figures illustrates the shift from the viscous fingering to the viscous-capillary transition zone.

Based on our results and considering different parameters simulated in this study, modified boundaries for displacement patterns is suggested (Figure 5.12). In our model, the boundaries of displacement patterns change as a function of pore size distribution: the intermediate zones between the boundaries become smaller as the pore size distribution decreases (uniform pore size distribution).

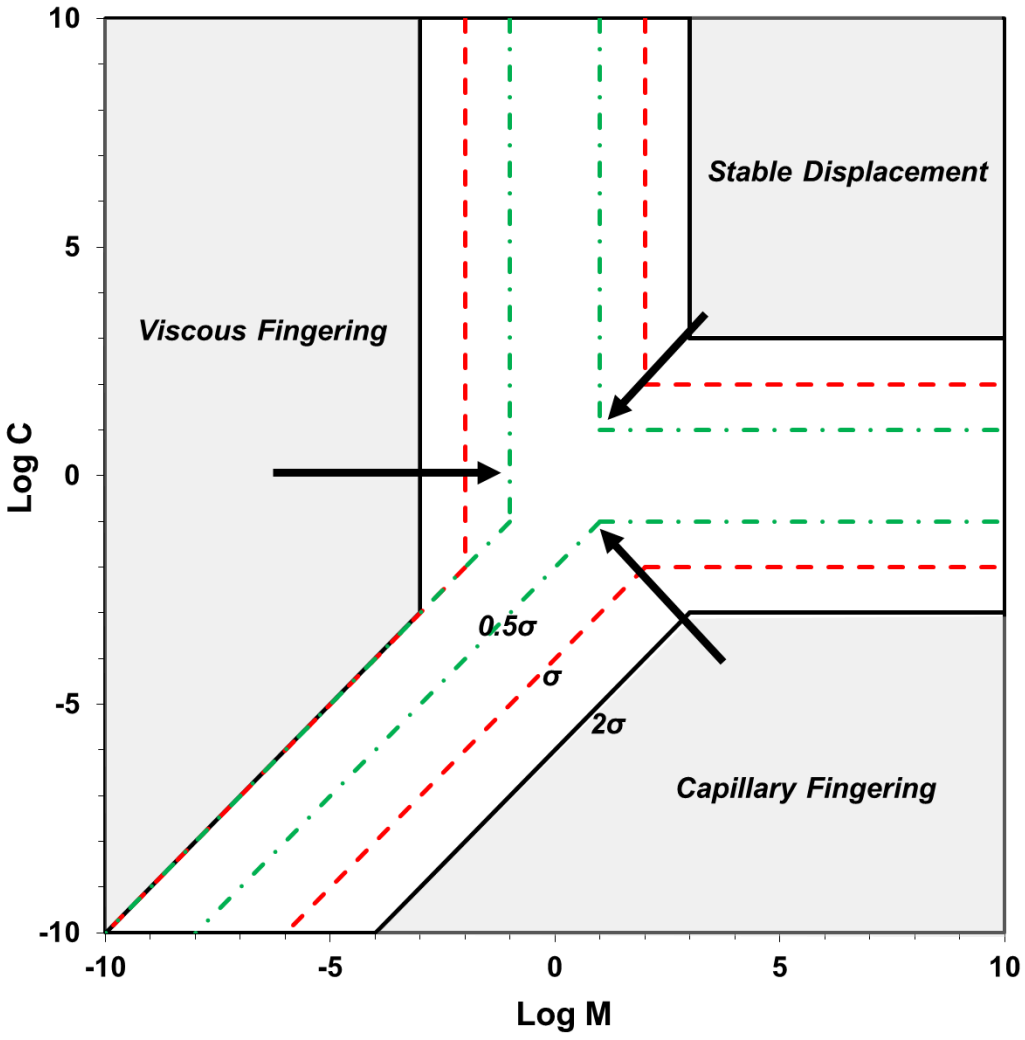

Figure 5.12 The suggested phase diagram for different pore size distributions. *σ: standard deviation of log(pore radius[μm])=0.31, 2σ=0.62, 0.5σ=0.15.*

5.4 Conclusion

The evolution of preferential patterns and phase diagram has been studied over the last decades. All the recent numerical and experimental studies confirmed the three displacement domains (viscous fingering, capillary fingering and stable conditions). However, the boundaries of the proposed phase diagrams by different researchers differ. It was discussed that the discrepancy is due to the variation in the pore size or the configuration of the model. However up to the author's knowledge there is no evidence for this. Because of the difficulties involved in the numerical and experimental simulations of fluid flow the previous studies only covers a limited range of fluids and injection rates.

In this study, a comprehensive study is performed using a 3D pore network model to simulate the immiscible multiphase fluid flow for a wide range of capillary numbers and viscosity ratios. Three different tube size distribution cases are simulated in order to explore the effect of pore size distribution on the boundaries of phase diagram. The evolution of the patterns is studies in terms of different parameters such as saturation, front width ratio, and size of the trapped clusters. Based on the results, a new model is suggested in which the boundaries of phase diagram is depend on the pore size distribution of the porous media.

CHAPTER 6

PARTICLE-FLUID INTERACTION:

PHOTOELASTIC DISK EXPERIMENT

6.1 Introduction

Fluid flow through granular media is an important process found in nature and various engineering applications. The fluid-particle interaction and the mechanical behavior of grains coupled with fluid flow are important research topics. There are still many unanswered questions regarding the geomechanics of fluid-particle interaction.

Fluid flow through granular media may induce the movement of granular particles, the change in force chains, or hydraulic fracturing under extreme flow rate conditions. Although numerical simulations such as discrete element modeling (software such as PFC and EDEM) allow to explore the effect of fluid flow on sediment particles, they need to have a subroutine for CFD code in order to simulate fluid-particle interaction. Moreover, the coupling physics between fluid dynamics and particle motion pose several challenges to researchers in terms of accuracy, computational costs and complexity of models.

The photoelasticity is an efficient technique to visualize the evolution of force chains in granular materials [Dantu, 1957; Wakabayashi, 1936]. Recently, photoelasticity has been used to visualize force networks in granular particle packs (photoelastic disk packing) under different stress conditions [Clark et al., 2012; Daniels and Hayman, 2008; Iikawa et al., 2016]. However, photoelasticiy has not been applied to explore particle-fluid interaction. The measurement of actual magnitude and orientation of forces between phtoelastic disk contacts involved many challenges such as the size of disks, difficulties in

image processing, and the large number of disks.

The main purpose of this study is to employ photoelasticity theory to analyze the effect of fluid flow in granular media. A transparent chamber is designed to contain several photoelastic disks with different size and to allow fluid through the phtoelastic disk packing. A fluid is injected to the chamber while the particle packing is under confining pressure. Several images are taken for the conditions of different confining pressures, particle packings and fluid injection rates. An algorithm of image processing technique is developed to measure the orientation and magnitude of contact forces.

6.2 Fundamentals of Photoelasticity

The distribution of contact forces between particles is optically visualized using the photoelastic theory. The method is based on birefringence phenomenon occurs mainly in the context of anisotropic crystals. When a ray of light passes through a boundary between two different homogeneous isotropic media, it will be reflected and refracted by the surface between them (Snell's law, Figure 6.1).

Birefringence or double refraction occurs when an optical anisotropic material such as calcite will refract a single beam of light and split it into two polarized refracted rays, called o-ray (ordinary ray) and e-ray (extraordinary ray), as shown in Figure 6.2. Each of these components experiences a different speed and direction which leads into a phase difference called phase retardation. The o-ray travels in the original direction of the incident light while the e-ray is refracted at an angle from the original light beam.

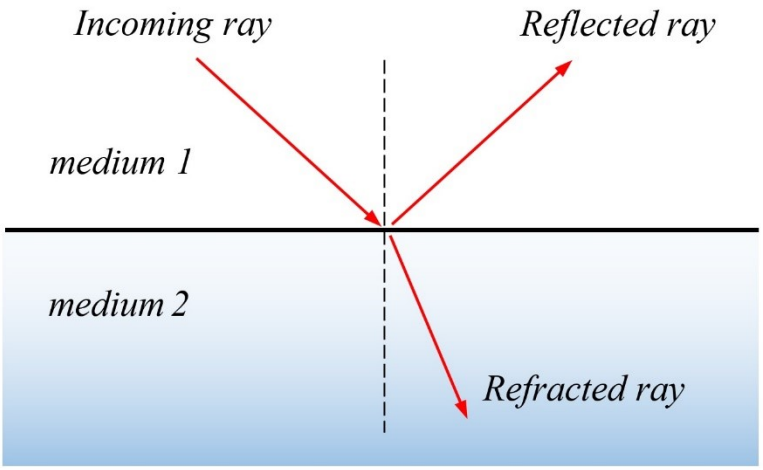

Figure 6.1 Reflection and refraction of light in a homogeneous media (Snell's law)

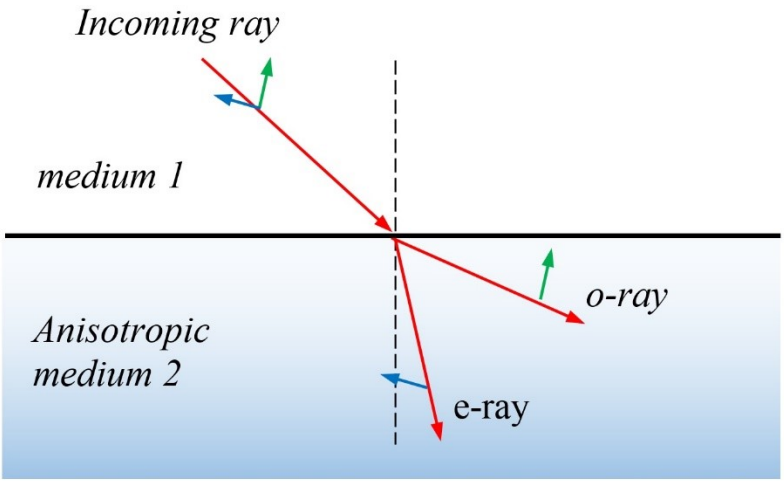

Figure 6.2 Birefringence in an anisotropic crystal media

Although birefringence exhibited in many materials (such as crystals), photoelastic materials expose the property of birefringence only on the application of stresses in which the magnitude of refractive indices in the photoelastic material is directly linked to the state of stress at that point. Birefringence in photoelastic materials occurs due to the strain difference between the vertical and horizontal direction. For example, more horizontal strain cause more concentration of atoms in the material. Therefore, there is a phase difference between the horizontal and vertical components of the light and the light ray

traveling in the horizontal direction is slower than the light in vertical direction. This phase difference changes the polarization state of the light beam and results in the formation of fringe patterns (Figure 6.3). Since, we are unable to observe the changes in polarity of light with naked eye, we need to use polariscope in order to convert birefringence into the fringe patterns. In 1853, Maxwell related the birefringence to stress through the stress-optical law which is expressed in Equation 6.1.

$$|\sigma_1\text{-}\sigma_3| = \frac{\lambda}{2\pi t C}\delta \tag{6.1}$$

Where σ_1 and σ_3 are the two principal stresses, λ is the wavelength of the light, t is the thickness of the material, δ is the phase difference between the refracted rays (phase retardation), C is the stress-optic coefficient.

The angular phase difference at the locations of the fringes can be described by:

$$\delta = 2\pi n \quad for \quad n = 0,1,2,3,\ldots \tag{6.2}$$

Where n is the fringe value and can be predicted by:

$$n = \frac{4PC}{\pi R\lambda} \tag{6.3}$$

Where, P is the force applied to the material and R is the radius of circular photoelastic disk.

Polariscope is constructed of two circular polarizers, each perpendicular to the path of light traveling through the photoelastic material. The first polarizer is called the "polarizer" (left-handed circular polarizer) and the second one is called "analyzer" (right-handed circular polarizer). When a light ray enters the polarizer, only the light of polarizer's orientation allows to travel. This light then enters trough the photoelastic material and experiences

some change in polarity. Finally, the light ray reaches the analyzer and only the light beams of its orientation can pass through. Figure 6.4 shows the components of a polariscope.

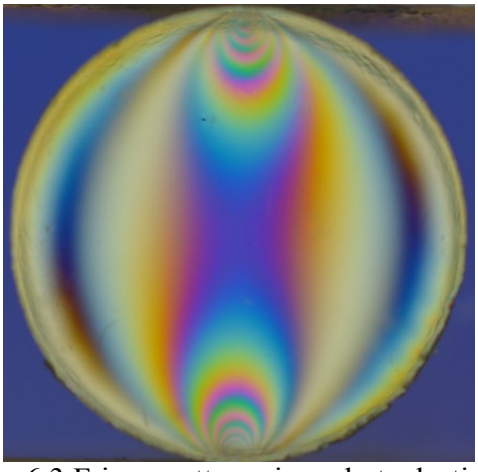

Figure 6.3 Fringe patterns in a photoelastic disk

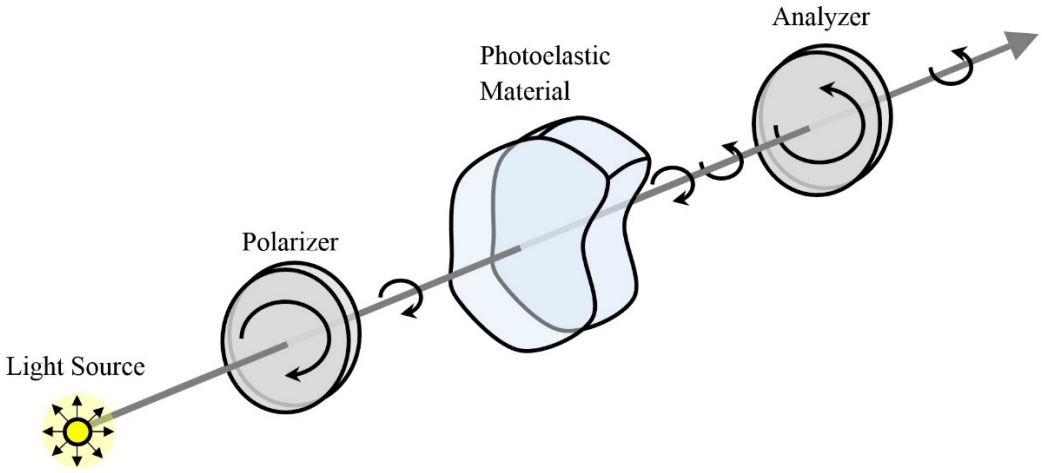

Figure 6.4 Components for a polariscope

6.3 Experimental Details

6.3.1 Equipment Set-up

An experimental setup is designed to apply a confining stress to photo-elastic discs and allow water flow through the disk packing (Figure 6.5) so that the effect of fluid flow

on the stress distribution patterns in dense granular media is explored. A square acrylic cell is designed and constructed by using two transparent acrylic plates bolted together. The dimensions of the square plates are 30.5×30.5×2.5 and 30.5×30.5×1.3 cm respectively for the top and bottom plates. The size of the pocket grooved in the bottom place is 22.9×18.8×0.95 cm and it is polished to make a perfectly transparent setting. A pressure plate with size of 2.5×18.8×0.95 cm is placed in the pocket and five springs is connected the wall of the pocket to the pressure plate. The springs used in this study are able to resist up to 64.6 N force. The stiffness of springs is 8.93 kN/m (OD=0.76, Length=2.08 and wire diameter=0.061 cm). In both sides of the pocket, two 1/8 inches holes are drilled for injection and drainage of the fluid during the test. The photoelastic material used in this study is PSM-1 sheet (30.5×30.5×0.98 cm) ordered from Vishay Precision Group. The photelastic sheets were cut at ASU Machine shop into 1.11, 0.79 and 0.61 cm diameter disks with average thickness of 0.98 inch. Table 6.1 shows the property of the photoelastic material PSM-1.

Table 6-1 Properties of the photoelastic material

Strain Optical Coefficient K	Elastic Modulus GPa (1000 psi)	Poisson's Ratio ν	Thickness (cm)
0.150	2.5 (360)	0.38	0.98

Two circular polarizer sheets (right-circular polarizing sheet APNCP37-035-RH and left-circular polarizing sheet APNCP37-035-STD, American Polarizers Inc.) are placed between the light source and the acrylic cell and another one between the acrylic set and the camera. For the light source, I used a 30.5x30.5 cm, 4500k bright White LED. A digital 5200D Nikon camera is used to record high-resolution images during the test. The water injection pressure can be controlled by adjusting the air pressure connected to a

cylindrical tank used for water supply. The injected water can be drained by the outlet tube from the acrylic cell.

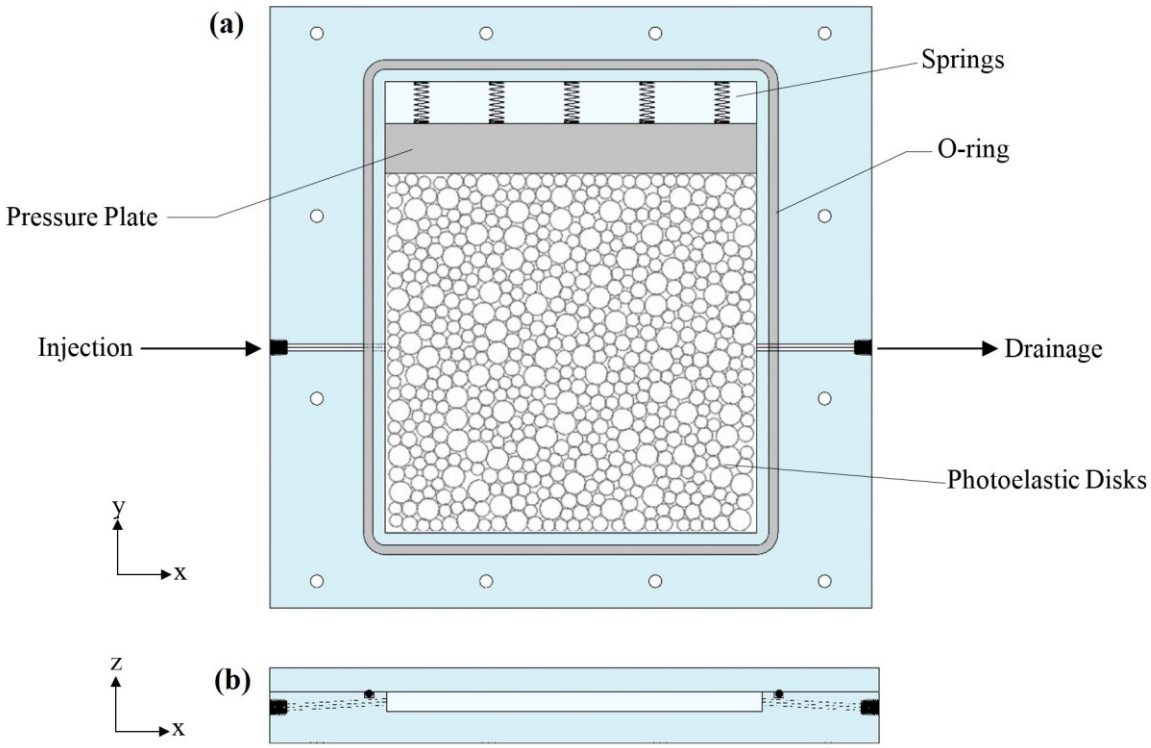

Figure 6.5 Transparent Photoelastic disc setup, (a) top view, (b) cross sectional view

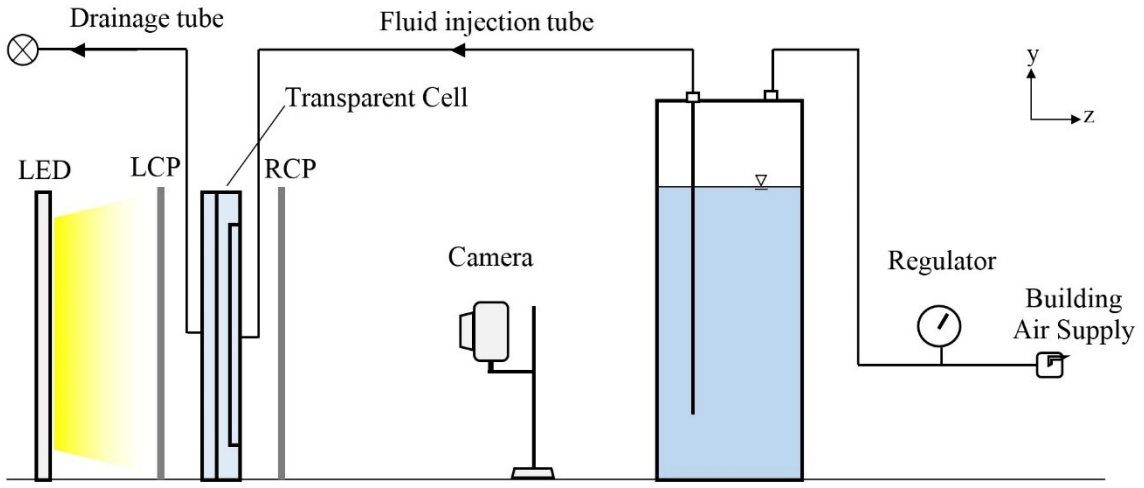

Figure 6.6 Experimental configuration for photoelastic disks: LED light source, LCP (left circular polarizer), RCP (right circular polarizer), digital camera, air tank, regulator and building air supply.

6.3.2 Experimental Procedure

The pocket inside the transparent cell is filled with photoelastic disks. The pressure plate with springs in the bottom of the pocket applies a confining stress to the particle packing. The average length of the springs measured by a caliper is used to calculate the confining pressure applied to the particle packing. Then, the transparent cell is tightened using 12 flat head screws (1/4 in-20 thread, 1-1/4 in length) and placed between the two polarizers as shown in Figure 6.6. The inlet and outlet tubes are connected to the acrylic cell and the water injection is initiated by increasing the air pressure inside the water tank.

Three types of particle packing include different numbers of the large, medium and small size disks. For each particle packing, two different confining pressure (low and high) is applied to the media using the springs. The information about the particle packing and confining pressure is shown in Table 6.2.

Table 6-2 Particle packing configurations and confining pressures used in this study

Particle Packing	Number of disks			Total number of disks	Low Confining Pressure (kPa)	High Confining Pressure (kPa)
	D=1.11 (cm)	D=0.79 (cm)	D=0.61 (cm)			
A	96	192	289	577	31.0	48.9
B	72	288	216	576	28.9	46.2
C	58	343	173	574	22.7	39.3

6.4 Image Analysis

The goal of this section is to interpret the images and extract the stress distribution changes in the particle packing due to the applied vertical stress and fluid flow. The image processing used in this study includes (1) the extraction of photoelastic disk location; (2)

the detection of particle contacts; (3) the measurement of the angle and magnitude of contact forces. The algorithms for the image analysis are written in Matlab code.

6.4.1 Particle Locations

Prior to the fluid injection, a non-polarized image (taken without polarizer filters) is used to extract the location of all the particles (Figure 6.7a). Once this image is taken, it is converted to a RGB color model in which the original image is a combination of three different matrixes R (Red color matrix), G (Green color matrix) and B (Blue color matrix). Each color matrix has 6000×4000 pixels with values range from 0 to 255. The value of each pixel shows the intensity of the corresponding color. The "R" matrix is converted to a binary matrix using a criteria in which the pixels with the value of [100 to 125] replaced by 1 and all the other pixels with 0 (Figure 6.7b). This criterion allows us to extract particle boundaries. The Hoshen-Kopelman algorithm is then used to find all the clusters (here particles) and their belonging pixels. The greatest distance between two pixels in a same cluster (particle) is used as the diameter and the location between them is calculated as the center of that particle. By using this algorithm, the size and position of all the particles are calculated and recorded (Figure 6.7c). As shown in Figure 6.7, the thickness of the particles may affect the size of particles extracted by this procedure. This happens due to the deviation of the camera from the axis perpendicular to the specimen and has more effect particularly around the sides of the particle packing. In order to deal with this problem, all

the measured sizes with a same size range are fixed to the belonging actual particle size (1.11, 0.79 and 0.61 cm diameter).

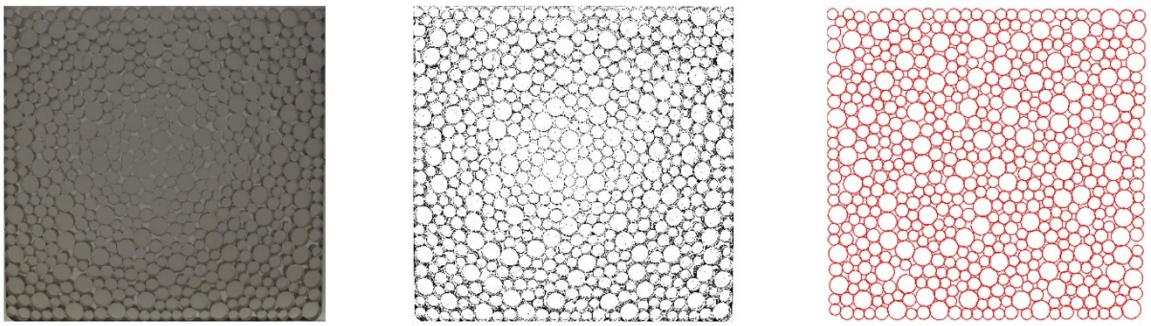

Figure 6.7 Extracting particle positions: (a) non-polarized raw image. (b) Filtered image, (c) Extracted particle size and locations using image processing.

6.4.2 Contact Detection

Once the size and position of the particles is extracted, the contacts between particles are identified by comparing their distance and location. For each particle, all the neighbors within a 2.22 cm radius distance (2 times of the biggest particle size) has detected and compared whether the summation of their radii is larger than their distance or not. Figure 6.8 shows the comparison process and Figure 6.9 shows the extracted contacts in the particle packing.

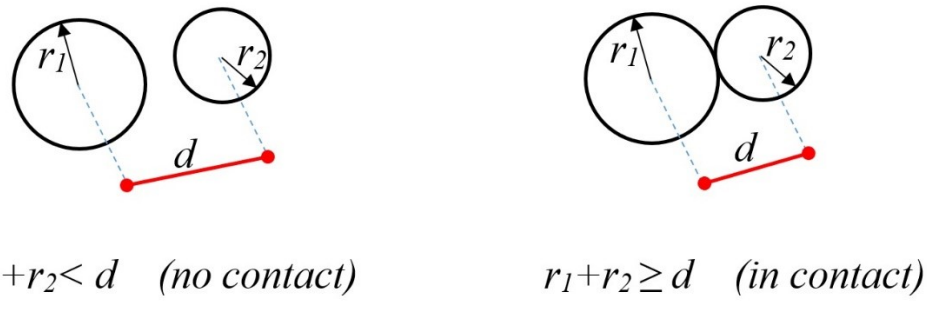

Figure 6.8 Two neighboring particles with and without contact

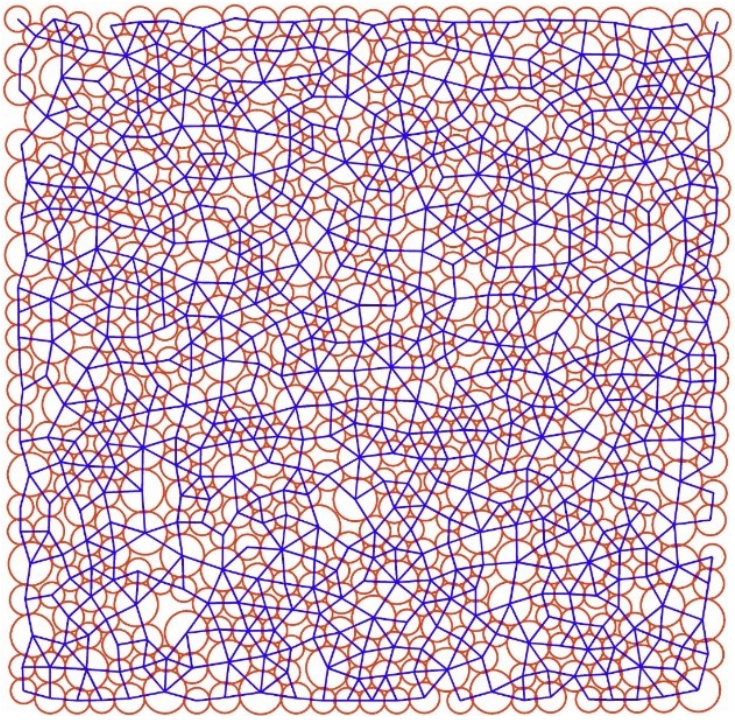

Figure 6.9 Particle interaction contact forces detected by particle positions. Contact force between each two particles is shown with blue lines cross the centers.

6.4.3 Contact Forces: Orientation and Magnitude

The direction of all the contacts are calculated using the center coordination (x,y) of each two connected neighboring disks:

$$\alpha = \tan^{-1}\left[\frac{y_j - y_i}{x_j - x_i}\right] \tag{6.4}$$

where, α is the direction of contact force, (x_1,y_1) and (x_2,y_2) are the center coordiation of particles i and j.

The magnitude of the contact forces can be estimated based on the counting of fringe values n. For example, in Figure 6.10, the fringe value for the shown disk subjected to a 38.6 kg force is n=12 which is counted by the number of fringes. Figure 6.11 shows the fringe values for a photoelastic disk subjected to different levels of force. The fringe

value can be predicted by Equation 6.3. The red dotted line in Figure 6.11 shows the predicted theoretical fringe value function using Eq. 6.3 and the paramters in Table 6.1. Through this prediction n=2.39P, where P is the force(kg). As Figure 6.11 shows, the data points measured for the photoelastic disk is in agreement with the predicted value.

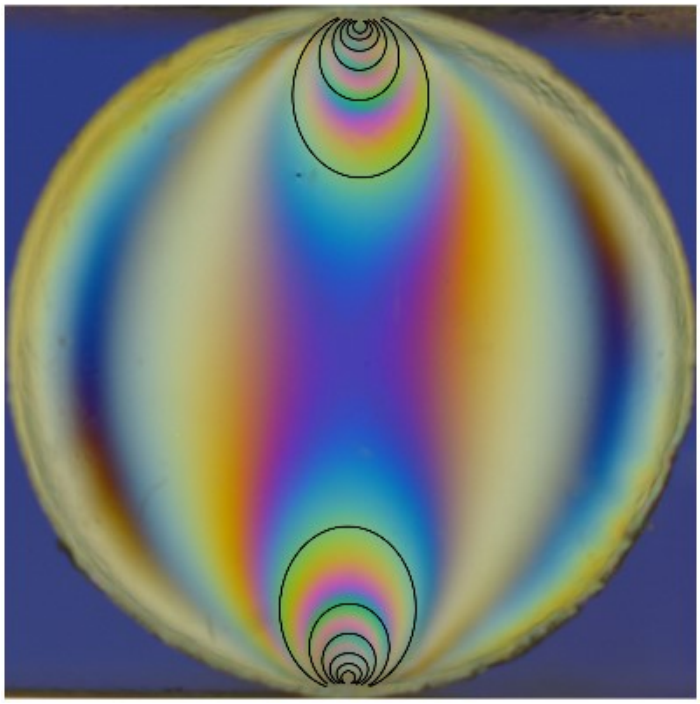

Figure 6.10 Fringe value for a photoelastic disk under pressure (n=12)

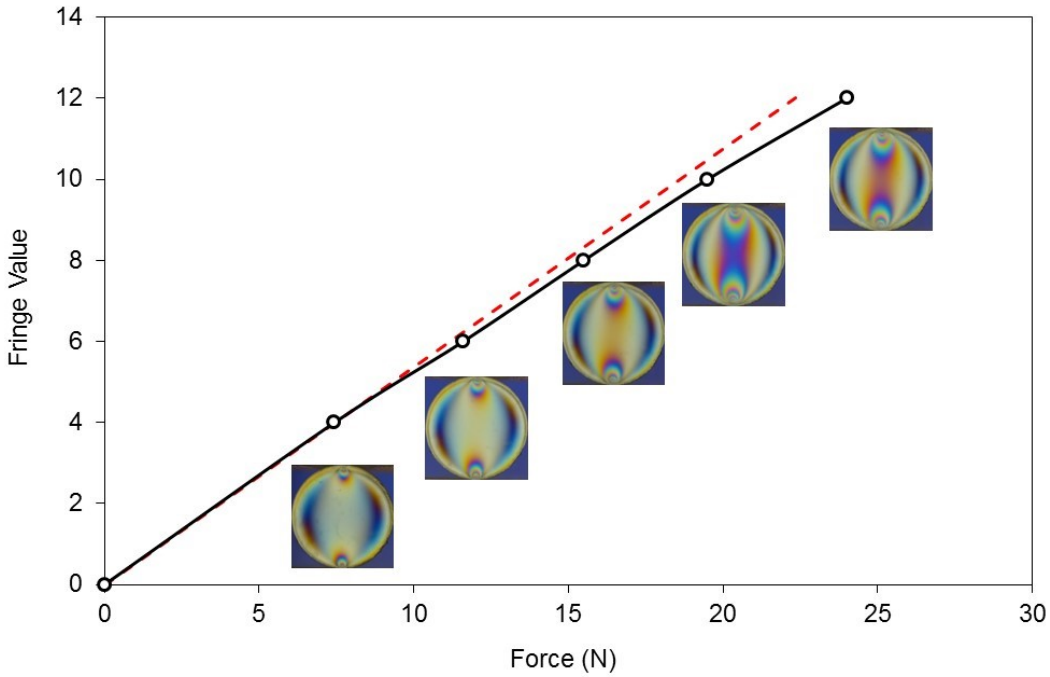

Figure 6.11 Fringe values (fringe counting) for a photoelastic disk. The red dotted line shows the predicted fringe value based on Eq. 5.1.

However, the count of integer number of fringes and its correlation with the applied contact forces may not be precise. In order to overcome this issue, a new method is proposed: the magnitude of the force is related to the distance between the fringe with the lowest red filtered color pixel value, here after called Lower Bound (LB) distance, and the boundary of the disk. Figure 6.12 shows the measured LB distance and force in a photoelastic disk. As the magnitude of a contact force increases, the LB distance increases. The red filtered color pixel value for all the contacts between each two neighboring disks are extracted and the magnitude of the contact forces is correlated with the LB distance.

Based on the proposed method the particle locations, direction and magnitude of contact forces can be detected. Figure 6.13a shows the detected particle locations, and their contact forces extracted from the image.

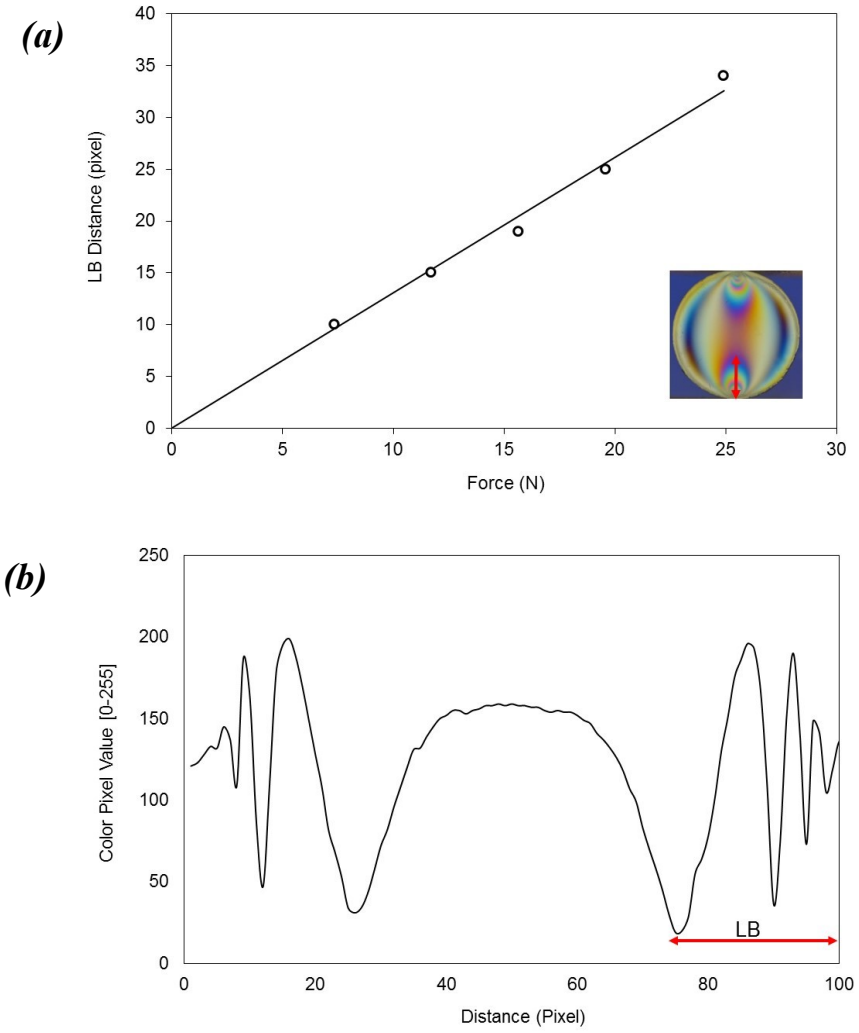

Figure 6.12 Relationship between LB distance and the magnitude of force in a photoelastic disk. (a) The measured value of LB distance and corresponding forces. (b) An example of LB distance measurement in a photoelastic disk.

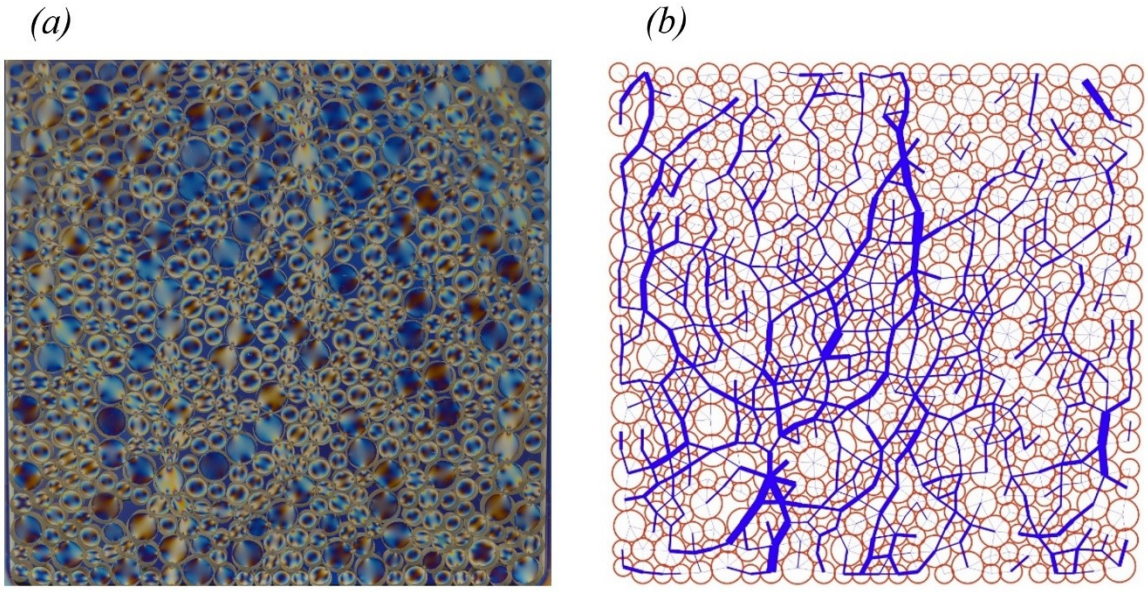

Figure 6.13 Force detection. (a) Image taken from the photoelastic particle packing A subjected to confining pressure 31 kPa. (b) Force contacts detected from the original image: The thicker the blue lines, the higher force value.

6.5 Results and Analysis

Water injection pressure increases from 0 kPa to 138.0 kPa, and images are taken for each 13.8 kPa injection pressure increments. Figure 6.14 shows the force chains for the particle packing A subjected to confining pressures 31.0 kPa and 48.9 kPa with and without fluid injection (injection pressure 0 and 96.5 kPa). As shown in this figure, force chains grow as the water pressure increases for a given confining pressure. For a given fluid injection pressure, force chains grow with the confining pressure as well. Based on the contact forces detected through the image processing, the total number of contact are 1260, 1276 and 1280 respectively for particle packing A, B and C. Figure 6.15(a) shows a polar chart which explains the number of contact in terms of force directions for different particle packings. No significant change is observed and the number of contacts are normally distributed in all directions for all the three particle packing.

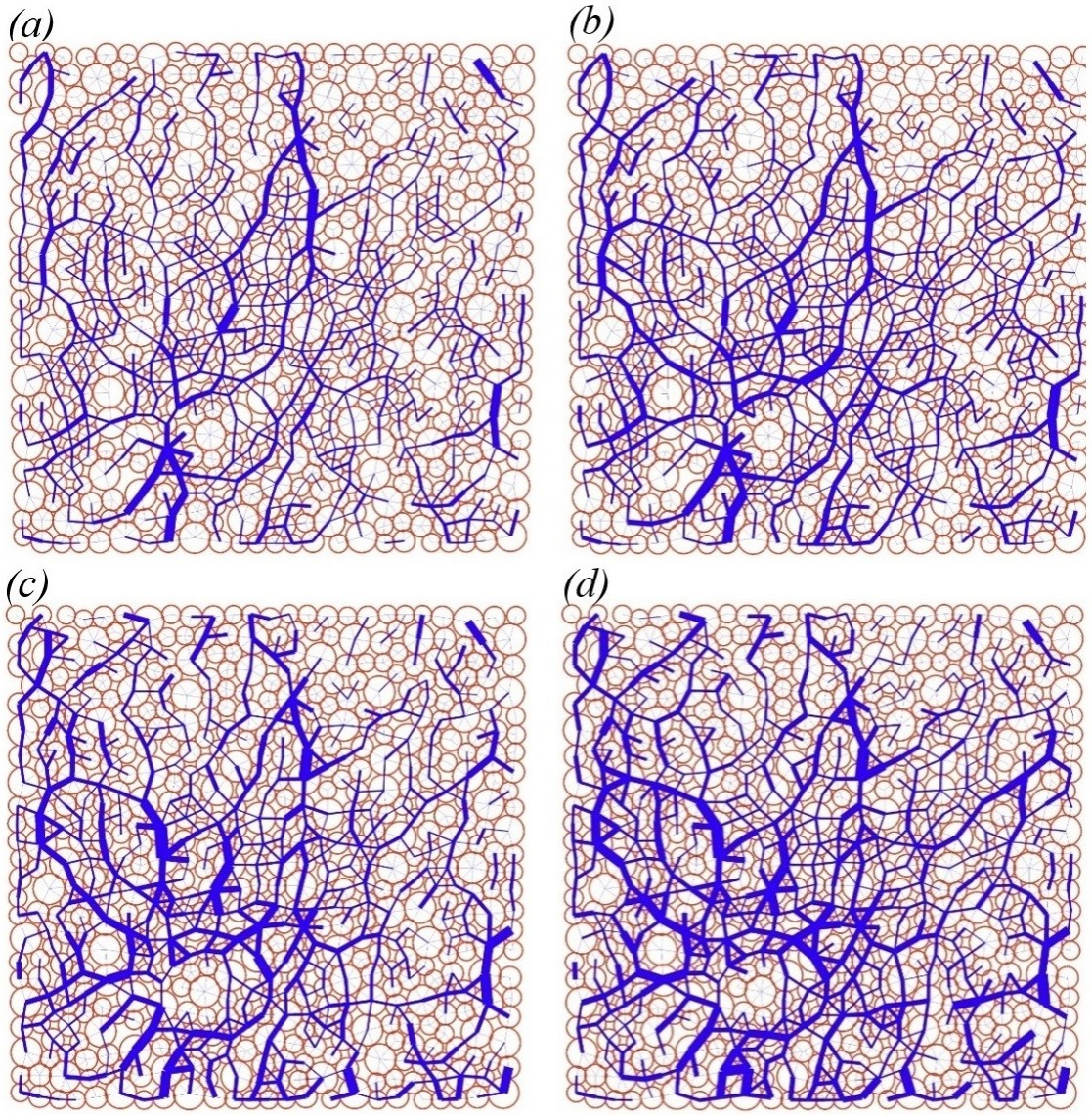

Figure 6.14 Force chains in the particle packing A. (a) Injection pressure=0 kPa, confining pressure σc=31 kPa. (b) Injection pressure= 96.5 kPa, confining pressure σc=31 kPa. (c) Injection pressure =0 kPa, confining pressure σc=48.9 kPa. (d) Injection pressure = 96.5 kPa, confining pressure σc=48.9 kPa.

The cumulative absolute of contact forces (global force) are plotted in a same way (in terms of force directions) in Figure 6.15(b) for the case without fluid injection and 6.15(c) for fluid injection pressure 96.5 kPa. In fluid free system, the overall direction of the global map (Figure 6.15b) is due to the differential length of springs that leads to a

deviation from the vertical axis. For example, the overall direction of forces for particle packing A at zero fluid injection pressure is about 60 degree. While the direction for particle packing B in this case is about 120 degree.

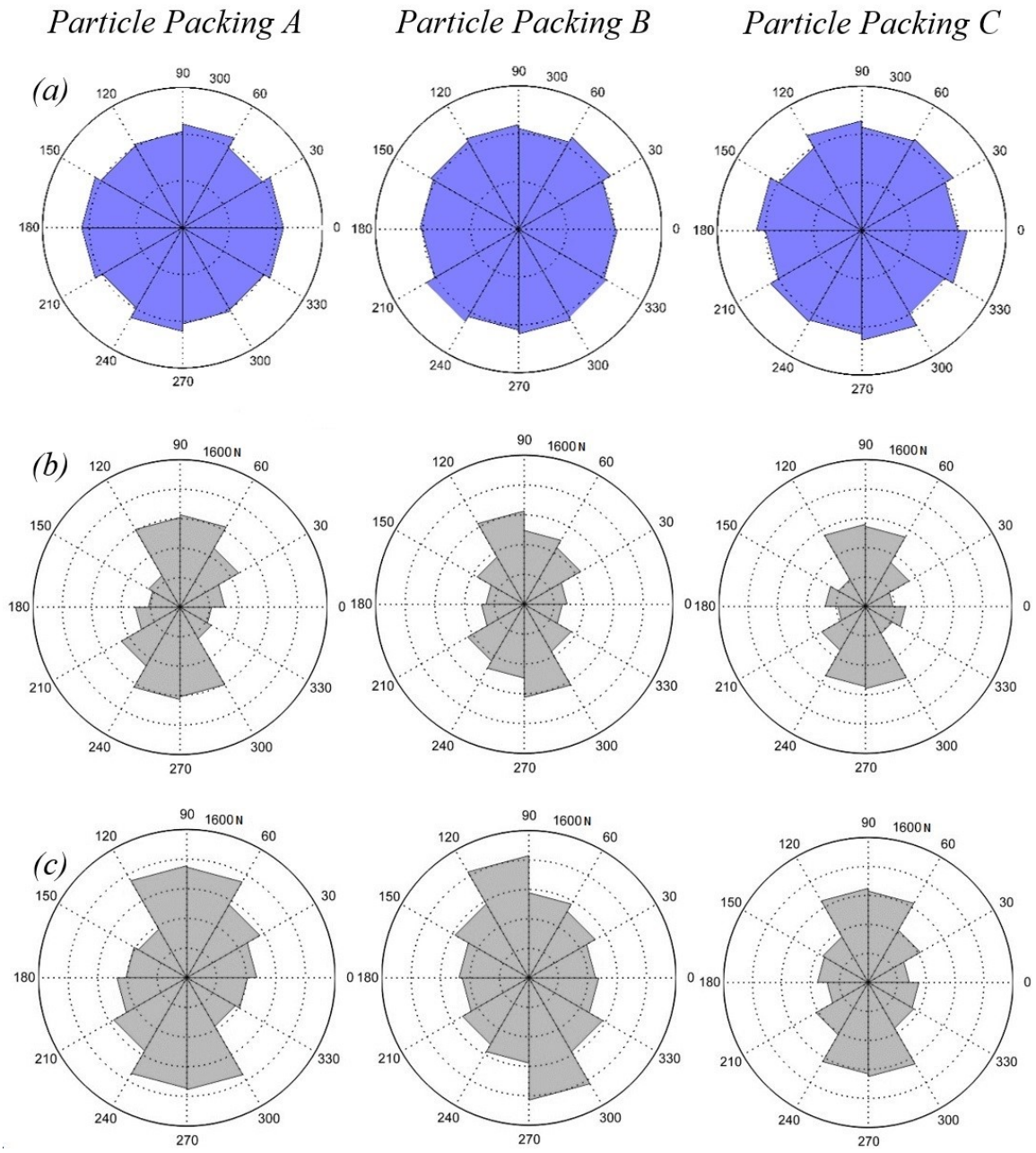

Figure 6.15 Polar plot of contacts (a) Number of contacts by different orientation angles. (b) Force magnitude (N) distribution for injection pressure = 0 kPa. (c) Force magnitude distribution for injection pressure = 96.5 kPa.

Comparison between Figure 6.15b and 6.15c shows that the fluid injection affects the horizontal forces more than the vertical forces. This also detected by calculating the ratio F_h/F_v which is the ratio of total horizontal forces to the total vertical forces (Figure 6.16). The ratio F_h/F_v increases as the fluid injection pressure increases which shows the horizontal fluid flow causes more effect in horizontal direction rather than the vertical direction. It is observed that the threshold for F_h/F_v decreases as the confining pressure increases (shown with arrows at figure 6.16). In addition, the higher the confining pressure the higher the ratio F_h/F_v.

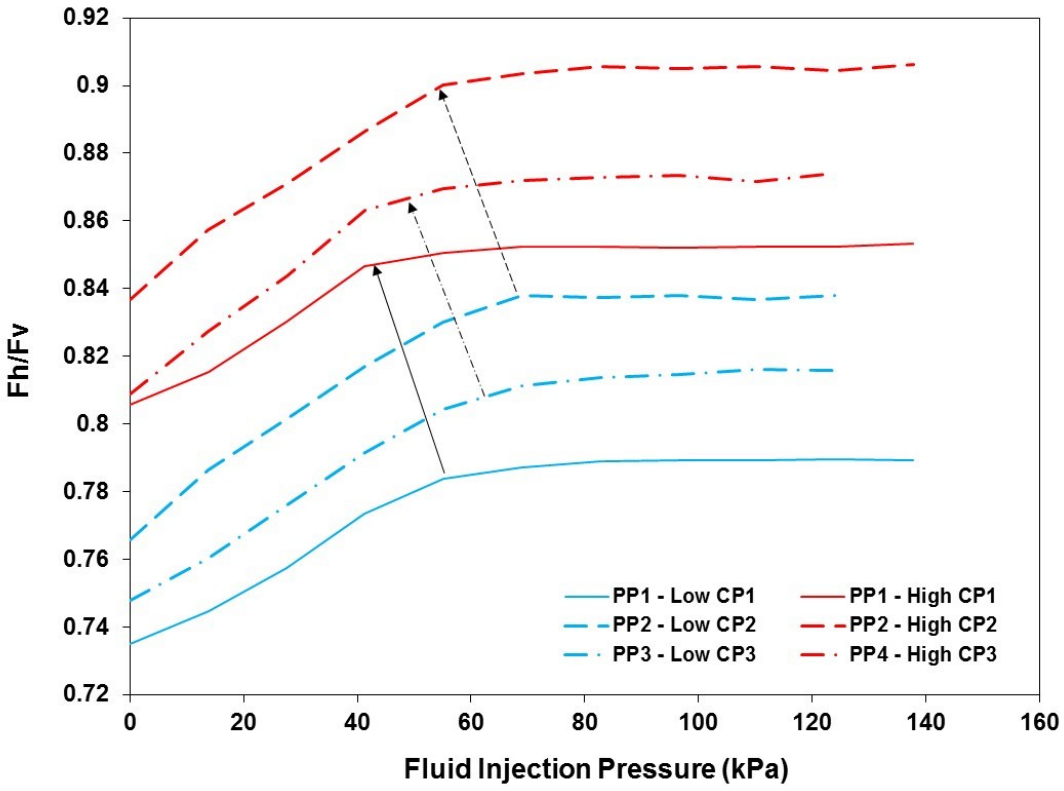

Figure 6.16 F_h/F_v for different fluid injection pressures. Arrows show the threshold of F_h/F_v changes. Blue solid line for particle packing A, Confining pressure 31.0 kPa. Blue dashed-line for particle packing B, Confining pressure 28.9 kPa. Blue dot-dashed-line for particle packing A, Confining pressure 22.7 kPa. Red solid line for particle packing A, Confining pressure 48.9 kPa. Red dashed-line for particle packing B, Confining pressure 46.2 kPa. Red dot-dashed-line for particle packing A, Confining pressure 39.3 kPA.

The cumulative absolute force (Global Force [N]) is calculated for F_h horizontal and F_v vertical component of the force chains in different confining pressure and fluid flow injection pressure conditions (high and low confining pressure). Then the normalized global force is calculated dividing the global force at the injection pressure (F_{inj}) by the initial global force without fluid flow ($F_{inj=0}$) (Figure 6.17). The normalized horizontal F_h and the vertical global force F_v is increases as the fluid injection pressure increases. The rate of changes in the horizontal component is greater than the vertical forces. In order to understand the distribution of the changes of force chains in our particle packing, the area of the media is divided into the three zones: upper zone, middle zone and lower zone (Figure 6.18a). The differential global force ΔF [N] is calculated for the horizontal ΔF_h and the vertical components of force chains ΔF_v (Figure 6.18b&c). ΔF_h has the maximum value for the middle zone where the fluid has the closest percolation path ways to the outlet (higher velocity zone) while the lowest changes in horizontal direction occurs at the upper zone where the particles are closer to the pressure plate and the force chains mostly forms in vertical directions. Figure 6.18c&f shows that the middle zone has the maximum vertical force value while the highest vertical force occurs at the lower zone. This can be clearly explained by figure 6.18d in which the conceptual orientation of force chains is presented. The force contacts starts to form at the regions close to the pressure plate and propagates through the boundaries that leads to a higher horizontal forces for the lower zones.

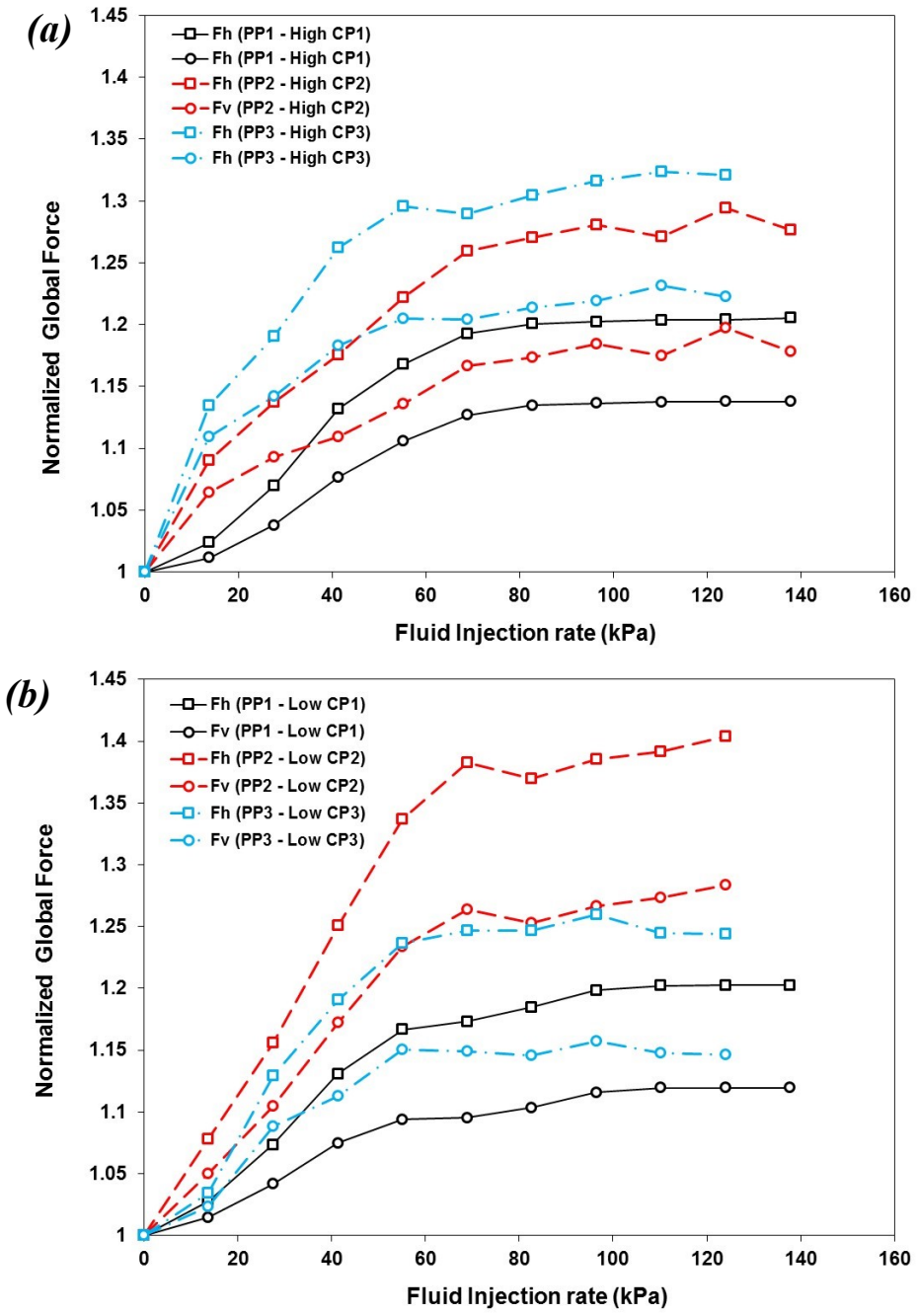

Figure 6.17 Normalized global force ($Force_{inj}/F_{inj=0}$) – Fluid injection pressure [kPa] for different particle packing cases. (a) High confining pressure. (b) Low confining pressure. Horizontal force indicated by F_h, vertical force by F_v, particle packing A, B, C by PP1, PP2 PP3 and Confining pressure by CP.

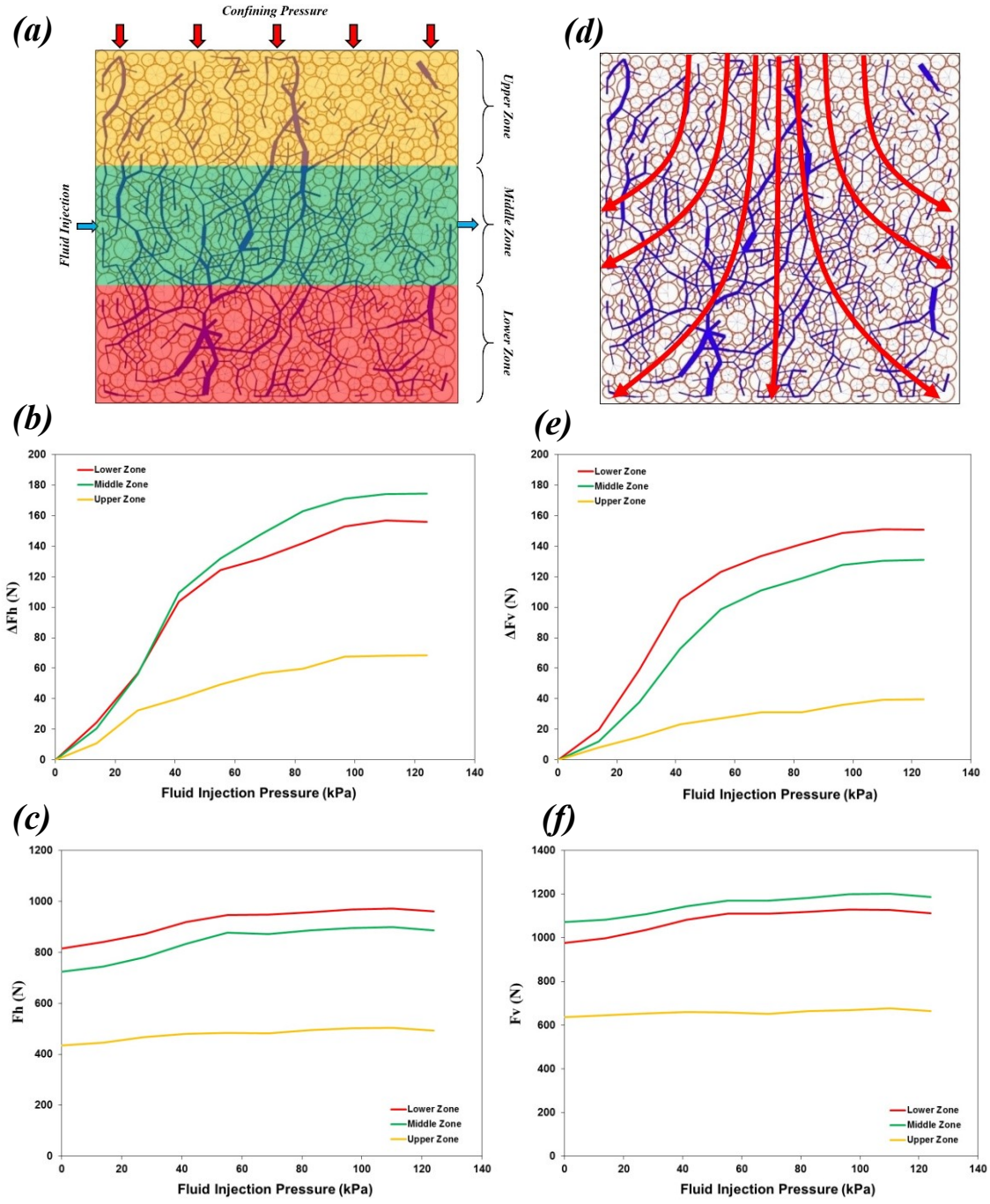

Figure 6.18 Magnitude of force chains by different horizontal zones for particle packing case A subjected to low confining pressure 28.2 kPa. (a) Order and location of different zones (upper, middle and lower) zone. (b) Differential horizontal force (N). (c) Horizontal force (N). (d) Conceptual direction of force chains. (e) Differential vertical force (N). (f) Vertical force (N).

6.6 Conclusion

In this study, photoelastic disks are used to visualize the evolution of force chains for fluid-particle interaction. A unique method is developed to correlate the external force to the pattern of fringes in a photoelastic disk. A two-dimensional transparent cell is fabricated to house a packing of photoelastic disks, to apply confining stress, and to induce fluid flow through particle packing. Water is injected with various flow pressures into the two-dimensional photoelastic disk packing under several confining stress. The direction of injected water is parallel and transverse direction to major confining stress. The location of photoelastic disks, the number of particle contacts, and the direction and magnitude of contact forces are obtained by using the image analysis algorithm developed in this study. The results shows that the fluid flow increases the contact forces among photoelastic disks in parallel direction with fluid flow. The orientation of force chains tends to the horizontal direction as the depth of the particles increases and the changes in force contacts of the particles located at the middle zone is higher than other regions.

CHAPTER 7

CONCLUSIONS

This study investigated multiphase fluid flow properties in porous media. The effects of various hydrate saturations and different hydrate pore filling habits on water retention curve and relative permeability were studied and the fitting parameters were suggested for different hydrate saturations and hydrate topologies. The preferential patterns of multiphase fluid flow were simulated for a wide range of fluid injection rates and viscosities. A new boundary of phase diagram was suggested based on the results. The fluid-flow interaction through granular media was visualized using photoleastic disk experiment. Salient Conclusions follow.

7.1 Conclusions-Suggestions

Relative water and gas permeability for gas production from hydrate-bearing sediments: DEM and pore network model simulation.

- The results of a pore-network model simulation show that modified Stone equation can be used to predict relative water and gas permeability for the gas production from hydrate-bearing sediments with properly chosen fitting parameters.
- The suggested fitting parameter n_w for relative water permeability is n_w=2.4 which is independent on initial hydrate saturations S_h=0.1~0.6. However, the suggested fitting parameter n_g for relative gas permeability varies from n_g=1.8 for S_h=0.1 to n_g=3.5 for S_h=0.6. These fitting parameters are valid for the condition at which hydrate pores are individually distributed, not forming patchy hydrate.

- The suggested fitting parameter n_g for high initial hydrate saturation condition is within the range of n_g-values used in the literature. The reason of dependency of n_g-value on initial hydrate saturation is explained by the different spatial distribution of gas pores for each initial hydrate saturation condition. The reason of dependency of n_g-value on initial hydrate saturation is explained by the different spatial distribution of gas pores for each initial hydrate saturation condition. The relative water permeability predicted by modified Stone equation is matched well with pore network model simulation results. However, a relative gas permeability curve of modified Stone equation shows a little discrepancy with numerical simulation results such as delayed gas percolation threshold, overestimation for $k_{rg}<0.4$, and underestimation for $k_{rg}>0.4$.

The water retention curve and relative permeability for gas production from hydrate bearing sediments: x-ray CT scanning and pore-network simulation.

- For water retention curves in hydrate-bearing sediments, the air-entry pressure P_0, residual water saturation S_{rw}, and m-value of the van Genuchten model depend on hydrate saturation S_h. The effect of hydrate patch size on the WRC steepness m is negligible, particularly at $S_h=0.2$.
- In relative permeability characterization using the van Genuchten model, the residual water saturation S_{rw} and maximum water saturation S_{wmax} should be corrected by considering hydrate saturation S_h. Also, the same m-value can be used for both gas and water permeability, but only in sediments with uniformly distributed hydrate; hydrate morphology greatly impacts the m-value for gas permeability.

- The Brooks-Corey model characterizes the gas and water permeability using two separate parameters. Hydrate saturation slightly affects the fitting parameter for water permeability; but the gas permeability must be corrected at different hydrate saturation S_h. Again, hydrate morphology dramatically affects the gas permeability. In particular, a more heterogeneous specimen (with a larger hydrate patch) tends to result in both higher gas and water permeability.
- Based on the results and analyses in this study, we proposed the recommendations summarized in Table 3.1.

The effect of hydrate saturation on water retention curves in THF hydrate-bearing sediments: Experimental study.

- The gas entry pressure and capillary pressure at a given effective water saturation in THF hydrate-bearing sediments increases with increasing hydrate saturation. Based on the experimental results, fitting parameters of van Genuchten equation are suggested: the m-value related to the shape of water retention curve decreases with increasing hydrate saturation, which means wider pore size distribution. The fitting parameter m-values suggested in this study are in good agreement with the values used for other hydrate numerical simulation studies. In addition, it is noted that the fitting parameters dependent on hydrate saturation should be updated during hydrate dissociation in numerical simulation.
- Based on the results and analyses in this study, we proposed the recommendations summarized in Figure 4.5.

Immiscible multiphase fluid flow through porous media: dimensionless numbers and phase diagram.

- The boundaries of phases are formed at same locations for both saturation and front width ratio plots. By comparing the results for different tube size distributions, we found that the distance between the boundary of the stable displacement and viscous fingering decreases as the tube size distribution of the network is more uniform.
- The saturation and the front width ratio increases as the standard deviation (σ) of the tube size distribution decreases. The final saturation is 0.78 for case 3 (0.5σ) and 0.74 for case 1 (2σ). Furthermore, the lower boundary of viscous fingering (1:1 sloped line) shifts to lower capillary numbers as the tube size distribution spreads
- The boundary of the phases can be distinguished based on the information of the trapped clusters. The maximum numbers of trapped clusters is occurred in the transition zone between the viscous fingering and stable displacement while the average volume of trapped clusters is higher in the transition zone of capillary fingering and viscous fingerings. This explains that the size of trapped clusters is smaller for viscous-stable transition zone which is in agreement with the previous observation published in the literature.
- Based on the results, a new model was suggested in which the boundaries of phase diagram is depend on the pore size distribution of the porous media.

Particle-fluid interaction: Photoelastic disk experiment

- A unique image processing technique was developed to extract the orientation and magnitude of force contacts induced in the photoelastic disk packing.
- The results shows that the fluid flow increases the contact forces among photoelastic disks in parallel direction with fluid flow. The orientation of force chains tends to the horizontal direction as the depth of the particles increases and the changes in force contacts of the particles located at the middle zone is higher than other regions.

7.2 Recommendations for Future Study

The direction and topics for future study are summarized based on the research topics:

The water retention curve and relative permeability for gas production from hydrate bearing sediments: x-ray CT scanning and pore-network simulation.

- The pore network model (consisting of spherical pores connected by tubes) may not represent a realistic description of real porous media. The maximal ball algorithm may produce homogenized tube size distribution. Therefore, the effect of pore shapes, pore size distribution and connectivity needs to be considered for more realistic water retention curve and relative permeability prediction. Based on the experimental water retention curve and assuming the network to be a bundle of capillary tubes it is possible to obtain an estimation of the throat size distribution. Then, the pore network model (tube size) can be tuned to match the water retention

curve to the experimental results. The capillary pressures for several polygonal shape tube can be obtained using the Lattice Boltzmann Method.

The effect of hydrate saturation on water retention curves in THF hydrate-bearing sediments: Experimental study.

- This study was performed using a sediment recovered from the Mallik 5L-38 site in Canada. The same methodology can be employed to measure water retention curves for different hydrate sediment samples.
- Although, THF hydrate formation and morphology was confirmed using micromodel test in this study, P and S-wave velocities for THF hydrate-bearing sediments need to be measured during WRC test for the future studies.
- The water retention curve was measured in this study for different hydrate saturation. Relative water and gas permeability in the presence of hydrates need to be measured. In addition, the water permeability as a function of THF hydrate saturation needs to be performed to verify the numerical simulations results.

Immiscible multiphase fluid flow through porous media: dimensionless numbers and phase diagram.

- The effect of size of the network and contact angle on the boundaries of phase diagram needs to be considered in the future studies.

Particle-fluid interaction: Photoelastic disk experiment

- The new image processing technique proposed in this study can be used in other relevant studies to measure actual force contacts among photoleastic particles.

- The effects of fluid viscosity and the fluid injection direction on the force chain need to be studied in the future works.
- Photoelastic material can be thermally loaded when heated and induced residual stresses in the material, which means that the material is no longer isotropic after it is unloaded. This would result in unrealistic results and errors that do not accurately define the forces induced in the photoelastic material. Using less thermally sensitive material is suggested for future studies.

REFERENCES

Aker, E., K. Maloy, Jorgen, A. Hansen, and G. G. Batrouni (1988), A Two-Dimensional Network Simulator for Two-Phase Flow in Porous Media, *Transport in Porous Media*, *32*, 163-186.

Al-Futaisi, A., and T. W. Patzek (2003), Impact of wettability alteration on two-phase flow characteristics of sandstones: A quasi-static description, *Water Resources Research*, *39*(2), 1042, doi:10.1029/2002wr001366.

Al-Kharusi, A. S., and M. J. Blunt (2007), Network extraction from sandstone and carbonate pore space images, J. Pet. Sci. Eng., 56, 219–231.

Anderson, B. J., et al. (2011), Regional long-term production modeling from a single well test, Mount Elbert Gas Hydrate Stratigraphic Test Well, Alaska North Slope, *Marine and Petroleum Geology*, *28*(2), 493-501, doi:10.1016/j.marpetgeo.2010.01.015.

Anderson, R., A. Chapoy, and B. Tohidi (2007), Phase relations and binary clathrate hydrate formation in the system H2-THF-H2O, *Langmuir*, *23*, 3440-3444.

Assouline, S. (2001), A model for soil relative hydraulic conductivity based on the water retention characteristic curve, *Water Resources Research*, *37*(2), 265-271, doi:10.1029/2000wr900254.

Bear, J. (1979), *Hydraulics of groundwater*, McGraw-Hill, New York.

Bear, J., and A. H.-D. Cheng (2010), *Modeling groundwater flow and contaminant transport*, Springer, Dordrecht/Heidelberg/London/New York.

Boswell, R. and Collett, T. (2011), Current perspectives on gas hydrate resources, Energy& environmental science, 4, 1206-1215.

Brady, N. C., and R. R. Weil (2007), *The Nature and Properties of Soils*, 14th ed., Pearson Prentice Hall.

Brooks, R. H., and A. T. Corey (1964), Hydraulic properties of porous media, *Hydrology paper No.3, Civil engineering department, Colorado state university, Fort Collins, Colorado*.

Chaouachi, M., A. Falenty, K. Sell, F. Enzmann, M. Kersten, D. Haberthür, and W. F. Kuhs (2015), Microstructural evolution of gas hydrates in sedimentary matrices observed with synchrotron X-ray computed tomographic microscopy, *Geochemistry, Geophysics, Geosystems*, *16*(6), 1711-1722, doi:10.1002/2015gc005811.

Choi, J.-H., S. Dai, J.-H. Cha, and Y. Seol (2014), Laboratory formation of noncementing hydrates in sandy sediments, *Geochemistry, Geophysics, Geosystems*, *15*, 1648-1656, doi:10.1002/.

Clark, A., H., L. Kondic, and R. Behringer, P. (2012), Particle Scale Dynamics in Granular Impact, *Physical Review Letters*, *109*, 238302.

Clennell, M. B., M. Hovland, J. S. Booth, P. Henry, and W. J. Winters (1999), Formation of natural gas hydrates in marine sediments 1. Conceptual model of gas hydrate growth conditioned by host sediment properties, *Journal of Geophysical Research*, *104*(B10), 22985-23003.

Corey, A. T. (1954), The interrelation between gas and oil relative permeabilities, *Producers Monthly*, *19*(1), 38-41.

Dai, S., and J. C. Santamarina (2013), Water retention curve for hydrate-bearing sediments, *Geophysical Research Letters*, *40*(21), 5637-5641, doi:10.1002/2013gl057884.

Dai, S., J. C. Santamarina, W. F. Waite, and T. J. Kneafsey (2012), Hydrate morphology: Physical properties of sands with patchy hydrate saturation, *Journal of Geophysical Research*, *117*(B11205), doi:10.1029/2012jb009667.

Daigle, H., and M. A. Rice (2015), Relative permeability of hydrate-bearing sediments from percolation theory and critical path analysis: theoretical and experimental results, in *American Geophysical Union Fall meeting Abstract,*, edited, pp. B12B-07, San Francisco, CA.

Daniels, K., E., and W. Hayman (2008), Force chains in seismogenic faults visualized with photoelastic granular shear experiments *Journal of Geophyscial Research*, *113*(B11411), doi:doi:10.1029/2008JB005781.

Dantu, P. (1957), Contribution à l'étude mécanique et géométrique des milieux pulvérulents, *Proceedings of the 4th International Conference on Soil Mechanics and Foundation Engineering, London. Oxford: Butterworks Scientific Publications*, *1*, 144:148.

Delahaye, A., L. Fournaison, S. Marinhas, I. Chatti, J.-P. Petitet, D. Dalmazzone, and W. Furst (2006), Effect of THF on equilibrium pressure and dissociation enthalpy of CO2 hydrates applied to secondary refrigeration, *Ind. Eng. Chem. Res.*, *45*, 391-397.

Dong, H. (2007), Micro-CT imaging and pore network extraction, PhD thesis, Imperial College, London, U. K.

Dong, H., and M. Blunt (2009), Pore-network extraction from micro-computerized-tomography images, *Physical Review E*, *80*(3), doi:10.1103/PhysRevE.80.036307.

Fredlund, D. G., and A. Xing (1994), Equations for the soil-water characteristic curve, *Canadian Geotechnical Journal*, *31*, 521-532.

Fredlund, D. G., A. Xing, M. D. Fredlund, and S. L. Barbour (1996), The relationship of the unsaturated soil shear to the soil-water characteristic curve, *Canadian Geotechnical Journal*, *33*(3), 440-448, doi:10.1139/t96-065.

Gamwo, I. K., and Y. Liu (2010), Mathematical modeling and numerical simulation of methane production in a hydrate reservoir, *Ind. Eng. Chem. Res.*, *49*, 5231-5245.

Gens, A., and E. Alonso (1992), A framework for the behaviour of unsaturated expansive clays, *Canadian Geotechnical Journal*, *29*(6), 1013-1032.

Ghanbarian, B., H. Daigle, A. G. Hunt, E. R. P., and M. Sahimi (2015), Gas and solute diffusion in partially saturated porous media: Percolation theory and effective medium approximation compared with Lattice Boltzmann simulations, *Journal of Geophysical Research: Solid Earth*, *120*, 182-190, doi:10.1002/.

Ghezzehei, T. A., and T. J. Kneafsey (2010), Measurements of the Capillary Pressure-Saturation Relationship of Methane Hydrate Bearing Sediments, paper presented at Offshore Technology Conferene, Houston, Texas, USA, May, 3-6, 2010.

Ginsburg, G., V. Soloviev, T. Matveeva, and I. Andreeva (2000), Sediment Grain-Size Control on Gas Hydrate Presence, Sites 994, 995, and 997, Scientific Results, Proc. Ocean Drill. Program Sci. Results, vol. 164, Ocean Drill. Program, College Station, Tex., doi:10.2973/ odp.proc.sr.164.236.2000.

Gough, S. R., and D. W. Davidson (1971), Composition of tetrahydrofuran hydrate and the effect of pressure on the decomposition, *Canadian Journal of Chemistry*, *49*, 2691-2699.

Gupta, A. (2007), Methane hydrate dissociation measurements and modeling: The role of heat transfer and reaction kinetics, PhD thesis, Colorado School of Mines, Golden, CO, U. S.

Hong, H., and M. Pooladi-Darvish (2003), A numerical study on gas production from formations containing gas hydrates, paper presented at Canadian international petroleum conference - 54th Annual technical meeting, Calgary, Canada, June 10-12, 2003.

Hong, H., and M. Pooladi-Darvish (2005), Simulaiton of depressurization for gas production from gas hydrate reservoirs, *The Journal of Canadian Petroleum Technology*, *44*(11), 39-46.

Hoshen, J., and R. Kopelman (1976), Percolation and cluster distribution. I. Cluster multiple labeling technique and critical concentration algorithm, Phys. Rev. B Solid State, 14(8), 3438–3445.

Iikawa, N., M. Bandi, M. , and H. Katsuragi (2016), Sensitivity of Granular Force Chain Orientation to Disorder-Induced Metastable Relaxation *Physical Review Letters 116*, 128001.

Jaiswal, N. J. (2004), Measurement of gas-water relative permeabilities in hydrate systems, MS thesis, Univ. of Alaska, Fairbanks, Alaska.

Jang, J., G. A. Narsilio, and J. C. Santamarina (2011), Hydraulic conductivity in spatially varying media-a pore-scale investigation, *Geophysical Journal International*, *184*(3), 1167-1179, doi:10.1111/j.1365-246X.2010.04893.x.

Jang, J., and J. C. Santamarina (2011), Recoverable gas from hydrate-bearing sediments: Pore network model simulation and macroscale analyses, *Journal of Geophysical Research*, *116*(B8), doi:10.1029/2010jb007841.

Jang, J., and J. C. Santamarina (2014), Evolution of gas saturation and relative permeability during gas production from hydrate-bearing sediments: Gas invasion vs. gas nucleation, *Journal of Geophysical Research: Solid Earth*, *119*(1), 116-126, doi:10.1002/2013jb010480.

Jang, J., G. A. Narsilio, and J. C. Santamarina (2011), Hydraulic conductivity in spatially varying media—A pore-scale investigation, Geophys. J. Int., 184, 1167–1179.

Jenner, K. A., S. R. Dallimore, I. D. Clark, D. Pare, and B. E. Medioli (1999), Sedimentology of gas hydrate host strata from the JAPEX/JNOC/GSC Mallik 2L-38 gas hydrate research well, in *Scientific results from JAPEX/JNOC/GSC Mallik 2L-38 gas hydrate research well,, Mackenzie delta, Northwest territories, Canada*, edited by S. R. Dallimore, T. Uchida and T. Collett, pp. 57-68, Geological Survery of Canada.

Johnson, A., S. Patil, and A. Dandekar (2011), Experimental investigation of gas-water relative permeability for gas-hydrate-bearing sediments from the Mount Elbert Gas Hydrate Stratigraphic Test Well, Alaska North Slope, *Marine and Petroleum Geology*, *28*(2), 419-426, doi:10.1016/j.marpetgeo.2009.10.013.

Kerkar, P., K. W. Jones, R. Kleinberg, W. B. Lindquist, S. Tomov, H. Feng, and D. Mahajan (2009), Direct observations of three dimensional growth of hydrates hosted in porous media, *Applied Physics Letters*, *95*(2), 024102, doi:10.1063/1.3120544.

Kerkar, P. B., K. Horvat, K. W. Jones, and D. Mahajan (2014), Imaging methane hydrates growth dynamics in porous media using synchrotron X-ray computed microtomography, *Geochemistry, Geophysics, Geosystems*, *15*(12), 4759-4768, doi:10.1002/2014gc005373.

Kleinberg, R. L., C. Flaum, D. D. Griffin, P. G. Brewer, G. E. Malby, E. T. Peltzer, and J. P. Yesinowski (2003), Deep sea NMR: Methane hydrate growth habit in porous media and its relationship to hydraulic permeability, deposit accumulation, and submarine slope stability, *Journal of Geophysical Research*, *108*(B10), 2508, doi:10.1029/2003jb002389.

Kurihara, M., et al. (2008), Analysis of the JOGMEC/NRCAN/Aurora Mallik gas hydrate production test through numerical simulation, paper presented at 6th International

Conference on Gas Hydrates, Chevron, Human energy, ConocoPhillips, US Department of Energy, Schlumberger, Vancouver, B. C., Canada, 6–10 Jul.

Kurihara, M., A. Sato, K. Funatsu, H. Ouchi, Y. Masuda, H. Narita, and T. S. Collett (2011), Analysis of formation pressure test results in the Mount Elbert methane hydrate reservoir through numerical simulation, Mar. Pet. Geol., 28(2), 502–516.

Lee, J. Y., J. C. Santamarina, and C. Ruppel (2010), Volume change associated with formation and dissociation of hydrate in sediment, *Geochemistry, Geophysics, Geosystems*, *11*(3), n/a-n/a, doi:10.1029/2009gc002667.

Lenormand, E. Touboul, and C. Zarcone (1988), Numerical models and experiments on immiscible displacements in porous media, *J. Fluid Mech.*, *189*, 165-187.

Li, B., X.-S. Li, G. Li, J.-L. Jia, and J.-C. Feng (2013), Measurements of Water Permeability in Unconsolidated Porous Media with Methane Hydrate Formation, *Energies*, *6*(7), 3622-3636, doi:10.3390/en6073622.

Liu, H., A. J. Valocchi, Q. Kang, and C. Werth (2013), Pore-Scale Simulations of Gas Displacing Liquid in a Homogeneous Pore Network Using the Lattice Boltzmann Method, *Transport in Porous Media*, *99*(3), 555-580.

Mahabadi, N., and J. Jang (2014), Relative water and gas permeability for gas production from hydrate-bearing sediments, *Geochemistry, Geophysics, Geosystems*, *15*, 2346-2353, doi:10.1002/2014GC005331.

Mahabadi, N., S. Dai, Y. Seol, T.S. Yup, J. Jang (2016), The Water Retention Curve and Relative Permeability for Gas Prodcution from Hydrate-Bearing Sediments: Pore-Network Model Simulation, *Geochemistry, Geophysics, Geosystems*, doi:10.1002/2016GC006372.

Mahabadi, N., X. Zheng, and J. Jang (2016), The effect of hydrate saturation on water retention curves in hydrate-bearing sediments, *Geophysical Research Letters*, *43*(9), 4279-4287, doi:10.1002/2016gl068656.

Mahabadi, N., X. Zheng, D. Kang, J. Wang, S. Dai, Y. Seol, C. E. Zapata, T.-S. Yun, and J. Jang (2015), Water retention curve of tetrahydrofuran (THF) hydarte-bearing sediments, paper presented at American Geophysical Union Fall meeting, San Francisco, CA, December, 12~16, 2015.

Makino, T., T. Sugahara, and K. Ohgaki (2005), Stability boundaries of tetrahydrofuran + water system, *J. Chem. Eng. Data*, *50*, 2058-2060.

Mellan, I. (1977), *Industrial solvents handbook*, Noyes Data Corporation, Park Ridge, New Jersey, USA.

Minagawa, H., Y. Hirakawa, M. Sato, R. Ohmura, Y. Kamata, S. Takeya, J. Nagao, T. Ebinuma, H. Narita, and Y. Masuda (2004), Measurement of water permeability under the presence of methane hydrate, paper presented at AAPG Hedberg Research Conference, Vancouver, B. C., Canada, 12–16 Sep.

Minagawa, H., Y. Nishikawa, I. Ikeda, Y. Sakamoto, T. Komai, and H. Narita (2007), Measurement of methane hydrate sediment permeability using several chemical solutions as inhibitors, paper presented at The Seventh ISOPE Ocean Mining Symposium, Lisbon, Portugal, 1–6 Jul.

Moridis, G. J., and M. B. Kowalsky (2005), Depressurization-induced gas production from class-1 hydrate deposites, paper SPE 97266 presented at Annual Technical Conference and Exhibition, ISA, Dallas, Tex., 9–12 Oct.

Moridis, G. J., and M. T. Reagan (2007a), Gas production from oceanic class 2 hydrate accumulations, paper presented at Offshore Technology Conference, Houston, Tex.

Moridis, G. J., and M. T. Reagan (2007b), Strategies for gas production from oceanic class 3 hydrate accumulations, paper presented at Offshore Technology Conference, OTC 18865, Houston, Tex.

Moridis, G. J., M. Kowalsky, and K. Pruess (2007), Depressurization-induced gas production from class1 hydrate deposits, SPE Reservoir Eval. Eng., 10(5), 458–481.

Moridis, G., J, M. Kowalsky, B, and K. Pruess (2008), Tough+Hydrate v1.0 User manual: A code for the simulation of system behaviro in hydrate-bearing geological media, *Lawrence Berkeley National Laboratory*, *LBNL-149E*.

Moridis, G., J, and M. Reagan, T (2007), Strategies for gas production from oceaenic class 3 Hydrate accumulations, in *Offshore Technology Conference*, edited, p. OTC 18865, Houston, TX, USA.

Moridis, G., J, and E. D. Sloan (2007), Gas production potential of disperse low-saturation hydrate accumulations in oceanic sediments, *Energy Conversion and Management*, *48*(6), 1834-1849, doi:10.1016/j.enconman.2007.01.023.

Moridis, G. J., M. T. Reagan, S.-J. Kim, Y. Seol, and K. Zhang (2009), Evaluation of the gas production potential of marine hydrate deposits in the Ulleung Basin of the Korea East Sea, paper SPE 110859 presented at 2007 SPE Asia Pacific Oil & Gas Conference and Exhibition, Jakarta, Indonesia, 30 Oct. to 1 Nov.

Myshakin, E. M., B. J. Anderson, K. Rose, and R. Boswell (2011), Simulations of variable bottomhole pressure regimes to improve production from the double-unit Mount Elbert, Milne Point Unit, North Slope Alaska hydrate deposit, Energy Fuels, 25, 1077–1091.

Myshakin, E. M., M. Gaddipati, K. Rose, and B. J. Anderson (2012), Numerical simulations of depressurization-induced gas production from gas hydrate reservoirs at the Walker Ridge 313 site, northern Gulf of Mexico, Mar. Pet. Geol., 34, 169–185.

National Energy Technology Laboratory, US Department of Energy (2011), Energy resource potential of methane hydrate An introduction to the science and energy potential of a unique resource (http://www.netl.doe.gov/technologies/oilgas/ publications/Hydrates/2011Reports/MH_Primer2011.pdf).

Öberg, A.-L., and G. Sällfors (1997), Determination of shear strength parameters of unsaturated silts and sands based on the water retention curve, *ASTM geotechnical testing journal*, *20*(1), 40-48.

Parker, J. C., R. J. Lenhard, and T. Kuppusamy (1987), A parametric model for constitutive properties governing multiphase flow in porous media, *Water Resources Research*, *23*(4), 618-624.

Pedarla, A., A. J. Puppala, L. R. Hoyos, S. K. Vanapalli, and C. Zapata (2012), SWRC Modelling framework for evaluating volume change behavior of expansive Soils, in *Unsaturated Soils: Research and Applications*, edited, pp. 221-228, Springer.

Reagan, M. T., M. B. Kowalsky, and G. J. Moridis (2010), The effect of reservoir heterogeneity on gas production from hydrate accumulations in the permafrost, paper presented at SPE Western Regional Meeting, Anaheim, CA, May, 27-29, 2010.

Reagan, M. T., and G. J. Moridis (2008), Dynamic response of oceanic hydrate deposits to ocean temperature change, *Journal of Geophysical Research*, *113*(C12), doi:10.1029/2008jc004938.

Phadnis, H. S., and J. C. Santamarina (2011), Bacteria in sediments: Pore size effects, G_eotech. Lett., 1, 91–93.

Rutqvist, J., and G. J. Moridis (2007), Numerical studies of geomechanical stability of hydrate-bearing sediments, in *Offshore Technology Conference*, edited, p. OTC 18860, Houston, TX, USA.

Rutqvist, J., and G. J. Moridis (2009), Numerical studies on the geomechanical stability of hydrate-bearing sediments, SPE J., 14(2), 267–282.

Santamarina, J. C., and J. Jang (2009), Gas production from hydrate bearing sediments: Geomechanical implications, Fire in the ice (This is DOE/NETL methane hydrate newsletter), 9(4), 18–22.

Santamarina, J. C., and J. Jang (2010), Energy geotechnology: Implications of mixed fluid condition, paper presented at International Conference on Unsaturated Soils, Int. Cent. for Numer. Methods in Eng., Barcelona, Spain, 6–8 Sep.

Santamarina, J. C., et al. (2015), Hydro-bio-geomechanical properties of hydrate-bearing sediments from Nankai Trough, *Marine and Petroleum Geology*, *66*, 434-450, doi:10.1016/j.marpetgeo.2015.02.033.

Silin, D., and T. Patzek (2006), Pore space morphology analysis using maximal inscribed spheres, *Physica A: Statistical Mechanics and its Applications*, *371*(2), 336-360, doi:10.1016/j.physa.2006.04.048.

Soga, K., S. L. Lee, M. Y. A. Ng, and A. Klar (2007), Characterisation and engineering properties of methane hydrate soils, in Characterisation and Engineering Properties of Natural Soils, pp. 2591–2642, Taylor and Francis, London.

Stone, H. L. (1970), Probability model for estimating thee-phase relative permeability, *Journal of Petroleum Technology*, *22*, 214-218.

Stryjek, R., and J. H. Vera (1986), PRSV: An improved Peng-Robinson equation of state for pure compounds and mixtures, *The Canadian Journal of Chemical Engineering*, *64*(323-33).

Tan, B. B. (2004), Geotechnical characteristic of sediments from Hydrate Ridge, Cascadia continental margin, MSc thesis, Mass. Inst. of Technol., Dep. of Civ. and Environ. Eng., Cambridge, MA, U. S.

Tohidi, B., R. Anderson, M. B. Clennell, R. W. Burgass, and A. B. Biderkab (2001), Visual observation of gas-hydrate formation and dissociation in synthetic porous media by means of glass micromodels, *Geology*, *29*(9), 867-870.

Valvatne, P. H., and M. J. Blunt (2004), Predictive pore-scale modeling of two-phase flow in mixed wet media, *Water Resources Research*, *40*(7), n/a-n/a, doi:10.1029/2003wr002627.

van Genuchten, M. T. (1980), A closed-form equation for prediction the hydraulic conductivity of unsaturated soils, *Soil Science Society of America Journal*, *44*, 892-898.

Waite, W. F., et al. (2009), Physical properties of hydrate-bearing sediments, *Reviews of Geophysics*, *47*(4).

Wakabayashi, T. (1936), Photo-elastic method for determination of stress in powdered mass, *Journal of the Physical Society of Japan*, *5*(5), 383-385.

Wilder, J. W., et al. (2008), An international effort to compare gas hydrate reservoir simulators, paper presented at 6th International Conference on Gas Hydrates, Vancouber, British Columbia, Canada, July 6-10, 2008.

Xue, K., J. Zhao, Y. Song, W. Liu, W. Lam, Y. Zhu, Y. Liu, C. Cheng, and D. Liu (2012), Direct Observation of THF Hydrate Formation in Porous Microstructure Using Magnetic Resonance Imaging, *Energies*, *5*(12), 898-910, doi:10.3390/en5040898.

Yokoyama, T., E. Nakayama, S. Kuwano, and H. Saito (2011), Relationships between seismic wave velocities, electric resistivities and saturation ratio of methane hydrate using core samples in laboratory experiments, paper presented at 7th International Conference on Gas Hydrates, Edinburgh, Scotland, UK, July 17-21, 2011.

Yun, T. S., F. M. Francisca, J. C. Santamarina, and C. Ruppel (2005), Compressional and shear wave velocities in uncemented sediment containing gas hydrate, *Geophysical Research Letters*, *32*(10), L10609, doi:10.1029/2005gl022607.

Zhang, C., M. Oostrom, T. Wietsma, W, J. Grate, W, and M. Warner, G (2011), Influence of Viscous and Capillary Forces on Immiscible Fluid Displacement: Pore-Scale Experimental Study in a Water-Wet Micromodel Demonstrating Viscous and Capillary Fingering, *energy&fules*, *25*(8), 3494-3505.